

Utah State University

DigitalCommons@USU

All Graduate Theses and Dissertations

Graduate Studies

5-2017

A Survey and Performance Analysis of Orbit Propagators for LEO, GEO, and Highly Elliptical Orbits

Simon P. Shuster
Utah State University

Follow this and additional works at: <https://digitalcommons.usu.edu/etd>



Part of the [Aerospace Engineering Commons](#)

Recommended Citation

Shuster, Simon P., "A Survey and Performance Analysis of Orbit Propagators for LEO, GEO, and Highly Elliptical Orbits" (2017). *All Graduate Theses and Dissertations*. 6510.

<https://digitalcommons.usu.edu/etd/6510>

This Thesis is brought to you for free and open access by the Graduate Studies at DigitalCommons@USU. It has been accepted for inclusion in All Graduate Theses and Dissertations by an authorized administrator of DigitalCommons@USU. For more information, please contact digitalcommons@usu.edu.



A SURVEY AND PERFORMANCE ANALYSIS OF ORBIT PROPAGATORS FOR
LEO, GEO, AND HIGHLY ELLIPTICAL ORBITS

by

Simon P. Shuster

A thesis submitted in partial fulfillment
of the requirements for the degree

of

MASTER OF SCIENCE

in

Aerospace Engineering

Approved:

David K. Geller, Ph.D.
Major Professor

Donald C. Thompson, Ph.D.
Committee Member

Stephen A. Whitmore, Ph.D.
Committee Member

Mark R. McLellan, Ph.D.
Vice President for Research and
Dean of the School of Graduate Studies

UTAH STATE UNIVERSITY
Logan, Utah

2017

Copyright © Simon P. Shuster 2017

All Rights Reserved

ABSTRACT

A Survey and Performance Analysis of Orbit Propagators for LEO, GEO, and Highly
Elliptical Orbits

by

Simon P. Shuster, Master of Science

Utah State University, 2017

Major Professor: David K. Geller, Ph.D.
Department: Mechanical and Aerospace Engineering

On-orbit targeting, guidance, and navigation relies on state vector propagation algorithms that must strike a balance between accuracy and computational efficiency. To better understand this balance, the relative position accuracy and computational requirements of numerical and analytical propagation methods are analyzed for a variety of orbits. For numerical propagation, several differential equation formulations (Cowell, Encke-time, Encke-beta, and Equinoctial Elements) are compared over a range of integration step sizes for a given set of perturbations and numerical integration methods. This comparison is repeated for two numerical integrators: a Runge-Kutta 4th order and a NLZD4/4. For analytical propagation, SGP4, which relies on mean orbital elements, is compared for element sets averaged with different amounts of orbit data.

(118 pages)

PUBLIC ABSTRACT

A Survey and Performance Analysis of Orbit Propagators for LEO, GEO, and Highly
Elliptical Orbits

Simon P. Shuster

On-orbit targeting, guidance, and navigation relies on state vector propagation algorithms that must strike a balance between accuracy and computational efficiency. To better understand this balance, the relative position accuracy and computational requirements of numerical and analytical propagation methods are analyzed for a variety of orbits. For numerical propagation, several differential equation formulations (Cowell, Encke-time, Encke-beta, and Equinoctial Elements) are compared over a range of integration step sizes for a given set of perturbations and numerical integration methods. This comparison is repeated for two numerical integrators: a Runge-Kutta 4th order and a NLZD4/4. For analytical propagation, SGP4, which relies on mean orbital elements, is compared for element sets averaged with different amounts of orbit data.

ACKNOWLEDGMENTS

I feel incredibly fortunate to be studying under Dr. Geller. He's been instrumental in my academic and professional growth. I'm grateful for his generous support, enthusiasm, and sense of humor.

I thank Don Thompson and Tyson Smith for providing me the opportunity to do this research. Their guidance and curiosity shaped this work. I appreciate them taking time out their busy schedules to listen to me babble.

Lastly, I thank my family and friends for their love and encouragement.

Simon Shuster

CONTENTS

	Page
ABSTRACT	iii
PUBLIC ABSTRACT	iv
ACKNOWLEDGMENTS	v
LIST OF TABLES	viii
LIST OF FIGURES	x
VARIABLES	xiv
ACRONYMSxviii
1 INTRODUCTION	1
2 ELEMENTS OF NUMERICAL PROPAGATION	3
2.1 Overview	3
2.2 Formulation of Differential Equations	3
2.2.1 Cowell's Formulation	3
2.2.2 Encke's Formulation	4
2.2.3 Equinoctial Elements	10
2.3 Perturbations	13
2.3.1 Earth's Gravity Field	13
2.3.2 Third Bodies	13
2.3.3 Solar Radiation Pressure	14
2.3.4 Drag	14
2.4 Numerical Integration Methods	15
2.4.1 Runge-Kutta	15
2.4.2 Nyström-Lear	15
3 SGP4	17
3.1 Background	17
3.2 Perturbation Effects	17
3.3 Overview	18
4 PROCEDURE	19
4.1 Overview	19
4.2 Truth Ephemeris Generation	19
4.3 Performance Metrics	22
4.3.1 Magnitude of Position Difference	22
4.3.2 Number of Integration Steps	22
4.3.3 Normalized Computation Time	22

4.4	Numerical Propagation Specifics	23
4.5	SGP4 Propagation Specifics	23
5	LEO RESULTS	25
5.1	Numerical Propagation	25
5.2	SGP4	30
5.3	Accuracy Comparison	31
5.4	Timing Comparison	34
6	GEO RESULTS	35
6.1	Numerical Propagation	35
6.2	SGP4	40
6.3	Accuracy Comparison	41
6.4	Timing Comparison	44
7	MOLNIYA RESULTS	45
7.1	Numerical Propagation	45
7.2	SGP4	50
7.3	Accuracy Comparison	51
7.4	Timing Comparison	54
8	GTO RESULTS	55
8.1	Numerical Propagation	55
8.2	SGP4	60
8.3	Accuracy Comparison	61
8.4	Timing Comparison	64
9	MMS RESULTS	65
9.1	Numerical Propagation	65
9.2	SGP4	70
9.3	Accuracy Comparison	71
9.4	Timing Comparison	74
10	PROPAGATOR COMPARISON	75
11	CONCLUSIONS AND FUTURE WORK	78
	REFERENCES	80
	APPENDICES	82
A	Coordinate Frames and Transformations	83
A.1	Coordinate Frame Descriptions	83
A.2	Coordinate Transformations	84
B	RK4 and NLZD4/4 Test Cases	87
B.1	First-Order Differential Equations	87
B.2	Second-Order Differential Equations	91
C	Elliptical Orbit Propagation Errors	95

LIST OF TABLES

Table	Page
3.1 SGP4 perturbation effects for different orbit conditions.	18
4.1 Initial classical orbital elements (0 if not specified) and initial perigee and apogee altitudes for each orbit.	19
4.2 Number of integration steps and corresponding time step (assuming a final time of 7 days) used for the truth ephemeris generation of each orbit.	21
4.3 Environment models used for each orbit.	21
4.4 Range of number of integration steps and corresponding range of time steps (assuming a final time of 7 days) for each orbit.	23
5.1 Number of integration steps and corresponding time step (if available) required by each differential equation formulation with the RK4 to match the 7 day LEO position accuracy of SGP4.	33
5.2 Number of integration steps and corresponding time step (if available) required by each differential equation formulation with the NLZD4/4 to match the 7 day LEO position accuracy of SGP4.	33
5.3 Time required for one integration step normalized to SGP4 runtime for LEO.	34
6.1 Number of integration steps and corresponding time step (if available) required by each differential equation formulation with the RK4 to match the 7 day GEO position accuracy of SGP4.	43
6.2 Number of integration steps and corresponding time step (if available) required by each differential equation formulation with the NLZD4/4 to match the 7 day GEO position accuracy of SGP4.	43
6.3 Time required for one integration step normalized to SGP4 runtime for GEO.	44
7.1 Number of integration steps and corresponding time step (if available) required by each differential equation formulation with the RK4 to match the 7 day Molniya position accuracy of SGP4.	53
7.2 Number of integration steps and corresponding time step (if available) required by each differential equation formulation with the NLZD4/4 to match the 7 day Molniya position accuracy of SGP4.	53

7.3	Time required for one integration step normalized to SGP4 runtime for Molniya.	54
8.1	Number of integration steps and corresponding time step (if available) required by each differential equation formulation with the RK4 to match the 7 day GTO position accuracy of SGP4.	63
8.2	Number of integration steps and corresponding time step (if available) required by each differential equation formulation with the NLZD4/4 to match the 7 day GTO position accuracy of SGP4.	63
8.3	Time required for one integration step normalized to SGP4 runtime for GTO.	64
9.1	Number of integration steps and corresponding time step (if available) required by each differential equation formulation with the RK4 to match the 7 day MMS position accuracy of SGP4.	73
9.2	Number of integration steps and corresponding time step (if available) required by each differential equation formulation with the NLZD4/4 to match the 7 day MMS position accuracy of SGP4.	73
9.3	Time required for one integration step normalized to SGP4 runtime for MMS.	74

LIST OF FIGURES

Figure	Page
2.1 A distribution of equal steps in time (yellow) and universal anomaly (red) around an elliptical orbit. Circles with both yellow and red indicate overlapping time and universal anomaly steps.	7
4.1 Position error after 7 days as a function of number of integration steps for GEO.	20
5.1 LEO position error as a function of time for each differential equation formulation. Line textures for Encke formulations indicate the following rectification tolerances: solid = 0% (every step), dashed = 0.01%, dotted = 0.1%. The left column shows RK4 results and the right column shows NLZD4/4 results. The upper row shows results using 10^4 integration steps and the lower row shows results using 10^3 integration steps.	26
5.2 7 day LEO position error as a function of number of integration steps for each differential equation formulation. Line textures for Encke formulations indicate the following rectification tolerances: solid = 0% (every step), dashed = 0.01%, dotted = 0.1%. The upper plot shows RK4 results and the lower plot shows NLZD4/4 results.	28
5.3 LEO position error as a function of time for different TLE fit lengths. A "0 day" fit refers to a TLE generated from a single state vector.	30
5.4 Comparison of 7 day LEO position error between numerical propagators and SGP4. Line textures for Encke formulations indicate the following rectification tolerances: solid = 0% (every step), dashed = 0.01%, dotted = 0.1%. The upper plot shows RK4 results and the lower plot shows NLZD4/4 results.	32
6.1 GEO position error as a function of time for each differential equation formulation. Line textures for Encke formulations indicate the following rectification tolerances: solid = 0% (every step), dashed = 0.01%, dotted = 0.1%. The left column shows RK4 results and the right column shows NLZD4/4 results. The upper row shows results using 10^3 integration steps and the lower row shows results using 10^2 integration steps.	36
6.2 7 day GEO position error as a function of number of integration steps for each differential equation formulation. Line textures for Encke formulations indicate the following rectification tolerances: solid = 0% (every step), dashed = 0.01%, dotted = 0.1%. The upper plot shows RK4 results and the lower plot shows NLZD4/4 results.	38

6.3	GEO position error as a function of time for different TLE fit lengths. A "0 day" fit refers to a TLE generated from a single state vector.	40
6.4	Comparison of 7 day GEO position error between numerical propagators and SGP4. Line textures for Encke formulations indicate the following rectification tolerances: solid = 0% (every step), dashed = 0.01%, dotted = 0.1%. The upper plot shows RK4 results and the lower plot shows NLZD4/4 results.	42
7.1	Molniya position error as a function of time for each differential equation formulation. Line textures for Encke formulations indicate the following rectification tolerances: solid = 0% (every step), dashed = 0.01%, dotted = 0.1%. The left column shows RK4 results and the right column shows NLZD4/4 results. The upper row shows results using 10^4 integration steps and the lower row shows results using 10^3 integration steps.	46
7.2	7 day Molniya position error as a function of number of integration steps for each differential equation formulation. Line textures for Encke formulations indicate the following rectification tolerances: solid = 0% (every step), dashed = 0.01%, dotted = 0.1%. The upper plot shows RK4 results and the lower plot shows NLZD4/4 results.	48
7.3	Molniya position error as a function of time for different TLE fit lengths. A "0 day" fit refers to a TLE generated from a single state vector.	50
7.4	Comparison of 7 day Molniya position error between numerical propagators and SGP4. Line textures for Encke formulations indicate the following rectification tolerances: solid = 0% (every step), dashed = 0.01%, dotted = 0.1%. The upper plot shows RK4 results and the lower plot shows NLZD4/4 results.	52
8.1	GTO position error as a function of time for each differential equation formulation. Line textures for Encke formulations indicate the following rectification tolerances: solid = 0% (every step), dashed = 0.01%, dotted = 0.1%. The left column shows RK4 results and the right column shows NLZD4/4 results. The upper row shows results using 10^4 integration step the lower row shows results using 10^3 integration step.	56
8.2	7 day GTO position error as a function of number of integration steps for each differential equation formulation. Line textures for Encke formulations indicate the following rectification tolerances: solid = 0% (every step), dashed = 0.01%, dotted = 0.1%. The upper plot shows RK4 results and the lower plot shows NLZD4/4 results.	58
8.3	GTO position error as a function of time for different TLE fit lengths. A "0 day" fit refers to a TLE generated from a single state vector.	60

8.4	Comparison of 7 day GTO position error between numerical propagators and SGP4. Line textures for Encke formulations indicate the following rectification tolerances: solid = 0% (every step), dashed = 0.01%, dotted = 0.1%. The upper plot shows RK4 results and the lower plot shows NLZD4/4 results.	62
9.1	MMS position error as a function of time for each differential equation formulation. Line textures for Encke formulations indicate the following rectification tolerances: solid = 0% (every step), dashed = 0.01%, dotted = 0.1%. The left column shows RK4 results and the right column shows NLZD4/4 results. The upper row shows results using 10^4 integration steps and the lower row shows results using 10^3 integration steps.	66
9.2	7 day MMS position error as a function of number of integration steps for each differential equation formulation. Line textures for Encke formulations indicate the following rectification tolerances: solid = 0% (every step), dashed = 0.01%, dotted = 0.1%. The upper plot shows RK4 results and the lower plot shows NLZD4/4 results.	68
9.3	MMS position error as a function of time for different TLE fit lengths. A "0 day" fit refers to a TLE generated from a single state vector.	70
9.4	Comparison of 7 day MMS position error between numerical propagators and SGP4. Line textures for Encke formulations indicate the following rectification tolerances: solid = 0% (every step), dashed = 0.01%, dotted = 0.1%. The upper plot shows RK4 results and the lower plot shows NLZD4/4 results.	72
10.1	Computation time relative to SGP4 required by each numerical propagator as a function of 7 day position accuracy. Solid lines indicate RK4 integration and dashed lines indicate NLZD4/4 integration. The green star located on each x-axis indicates the highest position accuracy attained by one SGP4 run.	76
A.1	Three general approaches for transformations between terrestrial (Earth-fixed) and celestial (inertial) systems [1].	85
B.1	Position error for $\dot{x} = f(x)$.	88
B.2	Position error for $\dot{x} = f(x, t)$.	89
B.3	Position error for $\dot{x} = f(x, t)$.	90
B.4	Position error for $\ddot{x} = f(\dot{x}, x, t)$.	92
B.5	Position error for $\ddot{x} = f(x, t)$.	93
B.6	Position error for $\ddot{x} = f(t)$.	94

C.1	Position error and true anomaly as a function of time for numerically propagated 2-body Molniya orbits. Initial true anomalies are indicated by color: $\theta_0 = 0^\circ$ (blue) and $\theta_0 = 180^\circ$ (red).	96
C.2	Magnitude of the perturbing acceleration for the Molniya orbit truth ephemeris (initial state given in Table 4.1 and environment model given in Table 4.3).	97
C.3	Radial, in-track, and crosstrack position error as a function of time for a Molniya orbit, propagated using Encke and Equinoctial with the RK4 and 10^4 integration steps over 7 days ($\Delta t = 60.48$). Encke formulations indicate the following rectification tolerances: solid = 0% (every step), dashed = 0.01%, dotted = 0.1%.	98
C.4	Position difference between 2-body Molniya orbits with an initial state difference (in terms of orbital elements) of $\delta\theta = 0.05^\circ$ and $\delta a = 10$ m.	99

VARIABLES

a	semi-major axis
a_0	initial semi-major axis
a_{pr}	perturbing acceleration in radial direction
a_{ph}	perturbing acceleration in angular momentum direction
$a_{p\theta}$	perturbing acceleration orthogonal to radial and angular momentum directions
\mathbf{a}_p	perturbing acceleration vector
A	area of the spacecraft
c	speed of light
C_d	coefficient of drag
$C_{n,m}$	gravitational coefficient of degree n and order m
C_r	coefficient of reflectivity
d_j	magnitude of position vector from a third body j to the spacecraft
\mathbf{d}_j	position vector from a third body j to the spacecraft
e	eccentricity
e_0	initial eccentricity
e_r	magnitude of position error
h_{ellps}	ellipsoidal height
i	inclination
i_0	initial inclination
$\hat{\mathbf{i}}_r$	unit vector in radial direction
$\hat{\mathbf{i}}_h$	unit vector in angular momentum direction
$\hat{\mathbf{i}}_\theta$	unit vector orthogonal to radial and angular momentum directions
J_n	gravitational coefficient of degree n and order 0
$J_{n,m}$	gravitational coefficient of degree n and order m
K	eccentric longitude
K_s	percentage of the sun that is not eclipsed, as seen by the spacecraft
l	mean longitude

L	true longitude
m	mass of the spacecraft
M	mean anomaly
n_{steps}	number of integration steps
\mathbf{N}	nutation matrix
$P_{n,m}$	associated Legendre polynomial of degree n and order m
\mathbf{P}	precession matrix
\mathbf{PN}	precession-nutation matrix
r	magnitude of position vector
r_{AU}	distance from the spacecraft to the Sun in AU
\mathbf{r}	position vector
\mathbf{r}_0	initial position vector
\mathbf{r}_c	position vector of osculating (conic) orbit
\mathbf{r}_f	final position vector
\mathbf{r}_{rec}	position vector upon rectification
\mathbf{r}_t	true position vector
$\hat{\mathbf{r}}_s$	unit position vector pointing from apparent position of the Sun to the spacecraft
$\dot{\mathbf{r}}$	velocity vector
$\ddot{\mathbf{r}}$	acceleration vector
R_e	radius of Earth
\mathbf{R}	sidereal-rotation matrix
\mathbf{R}_3	rotation matrix about z-axis
$S_{n,m}$	gravitational coefficient of degree n and order m
t	time
t_0	initial time
t_{rec}	time upon rectification
t_f	final time
\mathbf{T}	general rotation matrix
U	gravitational potential function
v_{rel}	magnitude of velocity vector of the spacecraft relative to the atmosphere

\mathbf{v}	velocity vector
\mathbf{v}_0	initial velocity vector
\mathbf{v}_f	final velocity vector
\mathbf{v}_{rec}	velocity vector upon rectification
\mathbf{v}_{rel}	velocity vector of the spacecraft relative to the atmosphere
$\hat{\mathbf{v}}_{rel}$	unit velocity vector of the spacecraft relative to the atmosphere
\mathbf{x}	state vector
$\dot{\mathbf{x}}$	state vector derivative
z_a	apogee altitude
z_p	perigee altitude
β	universal anomaly
β_f	final universal anomaly
δa	difference between semi-major axes
δr	magnitude of difference between perturbed and osculating position vectors
$\delta \mathbf{r}$	difference between perturbed and osculating position vectors
$\delta \dot{\mathbf{r}}$	difference between perturbed and osculating velocity vectors
$\delta \ddot{\mathbf{r}}$	difference between perturbed and osculating acceleration vectors
$\delta \theta$	difference between true anomalies
$\Delta \beta$	universal anomaly step
Δt	time step
λ	longitude
μ	gravitational parameter of the Earth
μ_j	gravitation parameter of a third body j
ω	argument of perigee
ω_0	initial argument of perigee
$\boldsymbol{\omega}$	angular velocity vector of the Earth
Ω	right ascension of the ascending node
Ω_0	initial right ascension of the ascending node
ϕ	geocentric latitude
Φ	solar flux at 1 AU

ρ_j	magnitude of position vector from the Earth to a third body j
$\boldsymbol{\rho}_j$	position vector from the Earth to a third body j
ρ	atmospheric density
θ	true anomaly
θ_0	initial true anomaly
ϖ	mean longitude

ACRONYMS

GCRF	geocentric celestial reference frame
GEO	geostationary orbit
GTO	geostationary transfer orbit
ICRF	international celestial reference frame
ITRF	international terrestrial reference frame
JPL	Jet Propulsion Laboratory
LEO	low Earth orbit
LVLH	local vertical, local horizontal reference frame
MMS	Magnetospheric Multiscale Mission
NLZD4/4	Nystrom-Lear 4 th order integrator
RK4	Runge-Kutta 4 th order integrator
SDP4	Simplified Deep Space Perturbations 4
SGP4	Simplified General Perturbations 4
SRP	solar radiation pressure
STK	Systems Tool Kit
TEME	true equator, mean equinox reference frame
TLE	Two-line element set
USSTRATCOM	United States Strategic Command

CHAPTER 1

INTRODUCTION

On-orbit trajectory predictions, ranging from seconds to days into the future, are necessary for targeting, guidance, and navigation [2]. Predictions are made using state vector propagation algorithms. It is desirable for these algorithms to be both high fidelity and computationally efficient.

Orbit propagation methods fall into three categories: numerical, analytical, and semi-analytical. Numerical propagation methods, which are sometimes referred to as special perturbations [1], numerically integrate the equations of motion pertaining to orbital motion and/or perturbations. Numerical propagation is accurate but time consuming. Analytical propagation methods, or general perturbations, replace the original equations of motion with an analytical approximation that captures the essential character of the motion over some limited time interval [1]. Approximating the motion makes analytical integration possible, which can be performed much faster than numerical integration. The cost of approximation is lower accuracy. Semi-analytical propagation methods blend numerical and analytical approaches. Secular and long period components of the motion are approximated and solved analytically, while short period variations are integrated numerically. Semi-analytical methods achieve higher accuracy than analytical methods while requiring less computation time than numerical methods.

Numerical propagation methods were developed well before computers could exploit their accuracy. In the mid 19th century, Encke presented the idea of integrating only orbital perturbations which attained enough accuracy with limited computing abilities [1]. Cowell chose to integrate the complete equations of motion to predict the return of Halley's comet in 1910 [3]. Signaling the capabilities of modern computers, the Navy generated the first numerically propagated space catalog in 1997 [4].

Analytical propagation methods were developed before numerical and semi-analytical methods because they did not require numerical integration, which was a burdensome task before computers were available [1]. In fact, algebraic solutions to the effects of perturbations were studied even before the two-body equations were complete [5]. The development of analytic theories continued well into the late 20th century. Theories derived by Kozai and Brouwer describe the motion of LEO satellites in closed-form [6–8]. Extending and refining this work resulted in the SGP4 propagator, which currently supports the USSTRATCOM public space catalog [9].

Numerical and analytical methods will be the focus of this survey. Semi-analytical methods will not be considered for the following reasons. First, these methods are typically used for either long-term orbit propagation or analysis involving many satellites [1], which is beyond the scope. Second, non-proprietary versions of code are difficult to obtain. Third, analyzing numerical and analytical methods places bounds on computation time and accuracy, so it can be assumed that a semi-analytical method would fall somewhere within these bounds.

The motivation for this research stems from the fact that published research comparing propagation methods is minimal. It is important to quantitatively understand the performance of common propagators for various orbits.

The objective of this research is to analyze numerical and analytical propagation methods over different orbit regimes for the application of on-board propagation. For numerical propagation, several differential equation formulations (Cowell, Encke-time, Encke-beta, and Equinoctial Elements) will be compared over a range of integration step sizes for a given set of perturbations and numerical integration methods. Perturbations will include a combination of a spherical harmonic gravity model, lunisolar, SRP, and drag, depending on the orbit. Two numerical integration methods will be tested: a Runge-Kutta 4th order and a NLZD4/4. For analytical propagation, SGP4, which relies on mean orbital elements, will be compared for element sets averaged with different amounts of orbit data. Relative position accuracy and computational requirements will be analyzed.

CHAPTER 2

ELEMENTS OF NUMERICAL PROPAGATION

2.1 Overview

A numerical propagator consists of three main components. In the form of an equation,

$$\text{propagator} = \text{differential equations} + \text{environment model} + \text{numerical integrator.} \quad (2.1)$$

The remainder of this chapter covers the components of equation (2.1) that are relevant to this analysis.

2.2 Formulation of Differential Equations

The following sections briefly describe the formulations of differential equations analyzed in this survey. These equations are numerically integrated to predict a satellite's future state. Full derivations are not presented. For more information about the theory behind these formulations, see [1–3, 10]. An algorithm overview for each formulation is also provided.

2.2.1 Cowell's Formulation

Cowell's formulation involves directly integrating the full equations of motion in rectangular coordinates. This method is efficient if the order of the perturbation acceleration is approximately equal to or larger than the central force gravity acceleration [3]. Cowell's formulation is

$$\ddot{\mathbf{r}} = -\frac{\mu}{r^3}\mathbf{r} + \mathbf{a}_p. \quad (2.2)$$

Equation (2.2) can also be written as a first-order system, where

$$\mathbf{x} = \begin{bmatrix} \mathbf{r} \\ \dot{\mathbf{r}} \end{bmatrix} \quad (2.3)$$

and

$$\dot{\mathbf{x}} = \begin{bmatrix} \dot{\mathbf{r}} \\ -\frac{\mu}{r^3}\mathbf{r} + \mathbf{a}_p \end{bmatrix}. \quad (2.4)$$

A Cowell algorithm is summarized as follows:

1. Set $\mathbf{r} = \mathbf{r}_0$, $\mathbf{v} = \mathbf{v}_0$, $t = t_0$.
2. Determine Δt by dividing t_f by n_{steps} .
3. Integrate the state vector from 0 to n_{steps} :
 - a. Integrate $\dot{\mathbf{r}}$ and $\ddot{\mathbf{r}}$ to obtain \mathbf{r} and \mathbf{v} .
 - b. Increment t , $t = t + \Delta t$.
4. Obtain \mathbf{r}_f , \mathbf{v}_f , and t_f .

2.2.2 Encke's Formulation

Instead of expressing acceleration with the full equations of motion, Encke's formulation describes the difference in accelerations between a perturbed orbit and an osculating (2-body) orbit. Integrating these differences and then adding them to the osculating position and velocity – propagated using Kepler's equation – results in the perturbed position and velocity. This process continues until the magnitude of the position difference exceeds a certain tolerance, at which point the osculating orbit is re-initialized using the current perturbed state. Re-initializing the osculating orbit is referred to as rectification.

Encke's formulation is more efficient than Cowell when the perturbation acceleration is much less than the central force gravity acceleration [3]. Under these conditions, it provides higher accuracy than Cowell for the same integration step size, or alternatively, the same

accuracy as Cowell despite using larger step sizes.

Two versions of Encke's formulation are analyzed: Encke-time and Encke-beta. Encke-time is the standard approach where time is the independent variable of the differential equations. Encke-beta is a time-regularized approach where universal anomaly is the independent variable.

Encke-time

Encke-time refers to Encke's formulation where the equations of motion are an implicit function of time. When Encke's formulation is presented, this version is typically assumed. From [3], the difference in acceleration between the perturbed and osculating orbits is

$$\delta\ddot{\mathbf{r}} = \frac{\mu}{r_c^3} \left\{ \left(1 - \frac{r_c^3}{r^3} \right) \mathbf{r} - \delta\mathbf{r} \right\} + \mathbf{a}_p, \quad (2.5)$$

where

$$\mathbf{r} = \mathbf{r}_c + \delta\mathbf{r}. \quad (2.6)$$

To avoid the interior problem [11], Battin's approach is used [3], and equation (2.5) is rewritten as

$$\delta\ddot{\mathbf{r}} = -\frac{\mu}{r_c^3} (f(q)\mathbf{r} + \delta\mathbf{r}) + \mathbf{a}_p, \quad (2.7)$$

where

$$q = \frac{\delta\mathbf{r} \cdot (\delta\mathbf{r} - 2\mathbf{r})}{\mathbf{r} \cdot \mathbf{r}} \quad (2.8)$$

and

$$f(q) = q \frac{3 + 3q + q^2}{1 + (1 + q)^{\frac{3}{2}}}. \quad (2.9)$$

Equation (2.7) can also be written as a first-order system, where

$$\mathbf{x} = \begin{bmatrix} \delta\mathbf{r} \\ \delta\dot{\mathbf{r}} \end{bmatrix} \quad (2.10)$$

and

$$\dot{\mathbf{x}} = \begin{bmatrix} \delta \dot{\mathbf{r}} \\ -\frac{\mu}{r_c^3} (f(q)\mathbf{r} + \delta \mathbf{r}) + \mathbf{a}_p \end{bmatrix}. \quad (2.11)$$

An Encke-time algorithm is summarized as follows:

1. Set $\mathbf{r}_{rec}, \mathbf{r}_c = \mathbf{r}_0, \mathbf{v}_{rec}, \mathbf{v}_c = \mathbf{v}_0, \delta \mathbf{r} = 0, \delta \dot{\mathbf{r}} = 0, t_{rec}, t = t_0$.
2. Determine Δt by dividing t_f by n_{steps} .
3. Integrate the state vector from 0 to n_{steps} :
 - a. Rectify if $\delta r/r > \text{tolerance}$:
 - i. Set $\mathbf{r}_{rec} = \mathbf{r}, \mathbf{v}_{rec} = \mathbf{v}, \delta \mathbf{r} = 0, \delta \dot{\mathbf{r}} = 0, t_{rec} = t$.
 - b. Integrate $\delta \dot{\mathbf{r}}$ and $\delta \ddot{\mathbf{r}}$ to obtain $\delta \mathbf{r}$ and $\delta \dot{\mathbf{r}}$.
 - c. Increment $t, t = t + \Delta t$.
 - d. Use a Kepler routine to determine \mathbf{r}_c and \mathbf{v}_c from $\mathbf{r}_{rec}, \mathbf{v}_{rec}$, and t .
 - e. Update the position, $\mathbf{r} = \mathbf{r}_c + \delta \mathbf{r}$, and velocity, $\mathbf{v} = \mathbf{v}_c + \delta \dot{\mathbf{r}}$.
4. Obtain $\mathbf{r}_f, \mathbf{v}_f$, and t_f .

Encke-beta

Encke-beta refers to Encke's formulation where the equations of motion are an implicit function of universal anomaly (beta) instead of time. Encke-beta is an example of a time-regularized formulation.

With fixed-step integration, time regularization becomes more advantageous as the orbit's eccentricity increases [2]. For elliptical orbits, equal steps in time are distributed abundantly around apogee and sparsely around perigee. This is problematic for time-based formulations because the number of steps required for accurate integration increases with a function's frequency. Since elliptical orbital motion changes much more rapidly around perigee than apogee, there arises a lopsided distribution of integration steps: too few around perigee and too many around apogee. Alternatively, equal steps in universal anomaly are

more evenly distributed, resulting in higher integration accuracy.

Figure 2.1 shows an elliptical orbit with equal steps in both time and universal anomaly. The distribution of steps shows how a fixed-step integrator would naturally perform better using a time-regularized formulation.

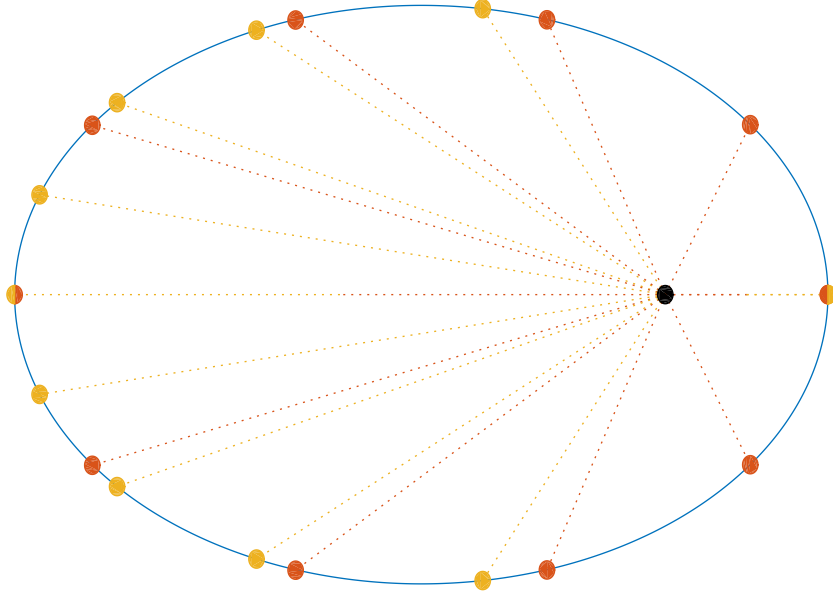


Fig. 2.1: A distribution of equal steps in time (yellow) and universal anomaly (red) around an elliptical orbit. Circles with both yellow and red indicate overlapping time and universal anomaly steps.

Regularization relating time to universal anomaly is achieved through the Sundman transformation,

$$\frac{dt}{d\beta} = t' = \frac{r_c}{\sqrt{\mu}}, \quad (2.12)$$

where the prime (') denotes differentiation with respect to β . From [2], the difference in time-regularized acceleration between the perturbed and osculating orbits is

$$\delta \mathbf{r}'' = \frac{\sigma_c}{r_c} \delta \mathbf{r}' + \frac{r_c^2}{\mu} \left(\frac{\mu}{r_c^3} \mathbf{r}_c - \frac{\mu}{r^3} \mathbf{r} + \mathbf{a}_p \right), \quad (2.13)$$

where

$$\sigma_c = \frac{\mathbf{r}_c \cdot \mathbf{v}_c}{\sqrt{\mu}}. \quad (2.14)$$

Using Battin's approach, equation (2.13) can be written as

$$\delta \mathbf{r}'' = \frac{1}{r_c} (\sigma_c \delta \mathbf{r}' - \delta \mathbf{r} - f \mathbf{r}) + \frac{r_c^2}{\mu} \mathbf{a}_p. \quad (2.15)$$

Writing equation (2.15) as a first-order system results in

$$\mathbf{x} = \begin{bmatrix} \delta \mathbf{r} \\ \delta \mathbf{r}' \end{bmatrix} \quad (2.16)$$

and

$$\dot{\mathbf{x}} = \begin{bmatrix} \delta \mathbf{r}' \\ \frac{1}{r_c} (\sigma_c \delta \mathbf{r}' - \delta \mathbf{r} - f \mathbf{r}) + \frac{r_c^2}{\mu} \mathbf{a}_p \end{bmatrix}. \quad (2.17)$$

An Encke-beta algorithm is summarized as follows:

1. Set $\mathbf{r}_{rec}, \mathbf{r}_c = \mathbf{r}_0, \mathbf{v}_{rec}, \mathbf{v}_c = \mathbf{v}_0, \delta \mathbf{r} = 0, \delta \mathbf{r}' = 0, t_{rec}, t = t_0, \beta = 0$.
2. Propagate a Keplerian orbit from $\mathbf{r}_{rec}, \mathbf{v}_{rec}$, and t_{rec} to t_f .
3. Determine β_f using the equation

$$\beta_f = \alpha_c \sqrt{\mu} (t_f - t_0) + \sigma_f - \sigma_0, \quad (2.18)$$

where

$$\alpha_c = \frac{1}{a_c} = \frac{2}{r_c} - \frac{v_c^2}{\mu} \quad (2.19)$$

and

$$\sigma = \frac{\mathbf{r} \cdot \mathbf{v}}{\sqrt{\mu}}. \quad (2.20)$$

4. Determine $\Delta\beta$ by dividing β_f by n_{steps} .
5. Integrate the state vector from 0 to n_{steps} :

a. Rectify if $\delta r/r > \text{tolerance}$:

i. Set $\mathbf{r}_{rec} = \mathbf{r}$, $\mathbf{v}_{rec} = \mathbf{v}$, $\delta \mathbf{r} = 0$, $\delta \mathbf{r}' = 0$, $t_{rec} = t$, $\beta = 0$.

ii. Determine β_f by propagating a Keplerian orbit from the \mathbf{r}_{rec} , \mathbf{v}_{rec} , and t_{rec} to t_f .

iii. Determine $\Delta\beta$.

b. Integrate $\delta \mathbf{r}'$ and $\delta \mathbf{r}''$ to obtain $\delta \mathbf{r}$ and $\delta \mathbf{r}'$.

c. Increment β , $\beta = \beta + \Delta\beta$.

d. Determine the current osculating state \mathbf{r}_c , \mathbf{v}_c , and t using the equations

$$\mathbf{r}_c = \left[1 - \frac{1}{r_{rec}} U_2(\beta, \alpha_c) \right] \mathbf{r}_{rec} + \frac{1}{\sqrt{\mu}} [r_{rec} U_1(\beta, \alpha_c) + \sigma_{rec} U_2(\beta, \alpha_c)] \mathbf{v}_{rec}, \quad (2.21)$$

$$\mathbf{v}_c = \left[-\frac{\sqrt{\mu}}{r_c r_{rec}} U_1(\beta, \alpha_c) \right] \mathbf{r}_{rec} + \left[1 - \frac{1}{r_c} U_2(\beta, \alpha_c) \right] \mathbf{v}_{rec}, \quad (2.22)$$

and

$$t = t_{rec} + \frac{1}{\sqrt{\mu}} [r_{rec} U_1(\beta, \alpha_c) + \sigma_{rec} U_2(\beta, \alpha_c) + U_3(\beta, \alpha_c)], \quad (2.23)$$

where U_n represents a Stumpff function [2].

e. Update the state using the equations

$$\mathbf{r} = \mathbf{r}_c + \delta \mathbf{r} \quad (2.24)$$

and

$$\mathbf{v} = \mathbf{v}_c + \frac{\sqrt{\mu} \delta \mathbf{r}'}{r_c}. \quad (2.25)$$

f. Decrement n_{steps} , $n_{steps} = n_{steps} - 1$, to find the remaining number of steps.

6. Obtain \mathbf{r}_f , \mathbf{v}_f , and t_f .

2.2.3 Equinoctial Elements

From the 2-body problem there arises six constant integrals of motion. A general second-order system – which encompasses Keplerian motion – is expressed as

$$\ddot{\mathbf{x}} = \mathbf{f}(\mathbf{x}, \dot{\mathbf{x}}, t) \quad (2.26)$$

with the constants

$$\boldsymbol{\alpha} = \boldsymbol{\alpha}(\mathbf{x}, \dot{\mathbf{x}}, t). \quad (2.27)$$

One possible set of constants describing Keplerian motion are the classical orbital elements

$$\boldsymbol{\alpha} = (a, e, i, \Omega, \omega, M). \quad (2.28)$$

In the presence of perturbations, the second-order system becomes

$$\ddot{\mathbf{x}} = \mathbf{f}(\mathbf{x}, \dot{\mathbf{x}}, t) + \mathbf{g}(\mathbf{x}, \dot{\mathbf{x}}, t) \quad (2.29)$$

and $\boldsymbol{\alpha}$ is no longer constant [3, 10]. Variation of parameters formulates the motion of a perturbed orbit by expressing the "constants" as a set of first-order differential equations. Gauss' equations, for example, describe this motion in terms of time-varying classical orbital elements.

Singularities exist in some of Gauss' equations when the inclination or eccentricity is near 0. To remove these singularities a new set of orbital elements, called Equinoctial Elements, is introduced [3]. They rely on the following quantities. The longitude of periapsis is defined as

$$\varpi = \Omega + \omega. \quad (2.30)$$

The mean longitude is defined as

$$l = \varpi + M. \quad (2.31)$$

The true longitude is defined as

$$L = \varpi + f. \quad (2.32)$$

Defining the eccentric longitude as

$$K = \varpi + E, \quad (2.33)$$

the augmented form of Kepler's equation in terms of mean longitude is

$$l = K + e \sin(\varpi) \cos(K) - e \cos(\varpi) \sin(K). \quad (2.34)$$

The non-singular Equinoctial Elements are a , P_1 , P_2 , Q_1 , Q_2 , and l , where

$$P_1 = e \sin(\varpi), \quad (2.35)$$

$$P_2 = e \cos(\varpi), \quad (2.36)$$

$$Q_1 = \tan\left(\frac{i}{2}\right) \sin(\Omega), \quad (2.37)$$

and

$$Q_2 = \tan\left(\frac{i}{2}\right) \cos(\Omega). \quad (2.38)$$

Derived using variation of parameters, the differential equations describing perturbed orbital motion in terms of Equinoctial Elements are

$$\dot{a} = \frac{2a^2}{h} \left[(P_2 \sin(L) - P_1 \cos(L)) a_{pr} + \frac{p}{r} a_{p\theta} \right], \quad (2.39)$$

$$\dot{P}_1 = \frac{r}{h} \left\{ -\frac{p}{r} \cos(L) a_{pr} + \left[P_1 + \left(1 + \frac{p}{r}\right) \sin(L) \right] a_{p\theta} - P_2 (Q_1 \cos(L) - Q_2 \sin(L)) a_{ph} \right\}, \quad (2.40)$$

$$\dot{P}_2 = \frac{r}{h} \left\{ \frac{p}{r} \sin(L) a_{pr} + \left[P_2 + \left(1 + \frac{p}{r}\right) \cos(L) \right] a_{p\theta} + P_1 (Q_1 \cos(L) - Q_2 \sin(L)) a_{ph} \right\}, \quad (2.41)$$

$$\dot{Q}_1 = \frac{r}{2h} (1 + Q_1^2 + Q_2^2) \sin(L) a_{ph}, \quad (2.42)$$

$$\dot{Q}_2 = \frac{r}{2h} (1 + Q_1^2 + Q_2^2) \sin(L) a_{ph}, \quad (2.43)$$

and

$$i = n - \frac{r}{h} \left\{ \left[\frac{a}{a+b} \left(\frac{p}{r} \right) (P_1 \sin(L) + P_2 \cos(L)) + \frac{2b}{a} \right] a_{pr} + \frac{a}{a+b} \left(1 + \frac{p}{r} \right) (P_1 \cos(L) - P_2 \sin(L)) a_{d\theta} + (Q_1 \cos(L) - Q_2 \sin(L)) a_{ph} \right\}, \quad (2.44)$$

where

$$b = a \sqrt{1 - P_1^2 - P_2^2}, \quad (2.45)$$

$$h = nab, \quad (2.46)$$

$$\frac{p}{r} = 1 + P_1 \sin(L) + P_2 \cos(L), \quad (2.47)$$

and

$$\frac{r}{h} = \frac{h}{\mu (1 + P_1 \sin(L) + P_2 \cos(L))}. \quad (2.48)$$

An algorithm incorporating equinoctial elements is summarized as follows:

1. Set $\mathbf{r} = \mathbf{r}_0$, $\mathbf{v} = \mathbf{v}_0$, $t = t_0$ and convert \mathbf{r}, \mathbf{v} to a, P_1, P_2, Q_1, Q_2, l .
2. Determine Δt by dividing t_f by n_{steps} .
3. Integrate the state vector from 0 to n_{steps} :
 - a. Integrate $\dot{a}, \dot{P}_1, \dot{P}_2, \dot{Q}_1, \dot{Q}_2, \dot{l}$ to obtain a, P_1, P_2, Q_1, Q_2, l :
 - i. Convert a, P_1, P_2, Q_1, Q_2, l to \mathbf{r}, \mathbf{v} to calculate \mathbf{a}_p .
 - ii. Convert \mathbf{r}, \mathbf{v} to $a, e, i, \Omega, \omega, \theta$.
 - iii. Rotate \mathbf{a}_p from ECI through the perifocal frame to local osculating polar coordinates $\hat{\mathbf{i}}_r, \hat{\mathbf{i}}_\theta, \hat{\mathbf{i}}_h$ to obtain $a_{pr}, a_{p\theta}, a_{ph}$.
 - b. Increment t , $t = t + \Delta t$.
4. Convert a, P_1, P_2, Q_1, Q_2, l to \mathbf{r}, \mathbf{v} .
5. Obtain $\mathbf{r}_f, \mathbf{v}_f$, and t_f .

2.3 Perturbations

The following sections list the mathematical models describing the perturbations considered in this analysis. These perturbations include Earth's non-spherical gravity field, third bodies, SRP, and drag. An environment model, per equation (2.1), refers to a collection of perturbations.

2.3.1 Earth's Gravity Field

From [12], the potential function describing Earth's nonuniform gravity field is

$$U = \frac{\mu}{r} \sum_{n=0}^{\infty} \sum_{m=0}^n \frac{R_e^n}{r^n} P_{n,m}(\sin \phi) (C_{n,m} \cos(m\lambda) + S_{n,m} \sin(m\lambda)). \quad (2.49)$$

The gravitational coefficients C and S from the GEM-T1 gravity model [13] are used. The perturbed gravity vector is computed in an Earth-fixed reference frame. For more information about the transformation between celestial and terrestrial reference frames, see Section A.2.

2.3.2 Third Bodies

From [10], the acceleration due to a third body is

$$\ddot{\mathbf{r}} = -\mu_j \left(\frac{\mathbf{d}_j}{d_j^3} + \frac{\boldsymbol{\rho}_j}{\rho_j} \right). \quad (2.50)$$

The subscript j indicates that equation (2.50) can be applied to any number of third bodies. To avoid the interior problem [11], Battin's approach is used [3], and (2.50) is rewritten as

$$\ddot{\mathbf{r}} = -\frac{\mu_j}{d_j^3} (\mathbf{r} + f(q_j) \boldsymbol{\rho}_j), \quad (2.51)$$

where

$$f(q_j) = q_j \left(\frac{3 + 3q_j + q_j^2}{1 + (1 + q_j)^{\frac{3}{2}}} \right) \quad (2.52)$$

and

$$q_j = \frac{1}{\rho_j^2} \mathbf{r} \cdot (\mathbf{r} - 2\rho_j). \quad (2.53)$$

Positions of the third bodies are provided by the JPL Developmental Ephemeris 421 [14].

2.3.3 Solar Radiation Pressure

From [15], the acceleration due to solar radiation pressure is

$$\ddot{\mathbf{r}} = C_r \frac{A}{m} \frac{K_s \Phi}{c} \left(\frac{1}{r_{AU}} \right)^2 \hat{\mathbf{r}}_s. \quad (2.54)$$

The unit vector from the sun to the spacecraft, $\hat{\mathbf{r}}_s$, points from the sun's apparent position. The apparent position is the sun's location when it radiated the photons currently striking the spacecraft.

2.3.4 Drag

From [1], the acceleration due to drag is

$$\ddot{\mathbf{r}} = -\frac{1}{2} \frac{A}{m} C_d \rho v_{rel}^2 \hat{\mathbf{v}}_{rel}. \quad (2.55)$$

The velocity in equation (2.55) is the velocity of the spacecraft relative to the atmosphere. As the atmosphere rotates with Earth, the relative velocity is

$$\mathbf{v}_{rel} = \mathbf{v} - \mathbf{T}\boldsymbol{\omega} \times \mathbf{r}, \quad (2.56)$$

where \mathbf{T} is the rotation matrix from the ITRF to the GCRF (see Section A.2). A lookup table is used to determine density. The 1976 U.S. Standard Atmosphere [16] is used to interpolate density corresponding to a given altitude. To determine the altitude, or ellipsoidal height, algorithm 13 from [1] is used.

2.4 Numerical Integration Methods

The following sections briefly describe the numerical integration methods used in this analysis. It is important to note that for on-orbit propagation, the integration method will be fixed-step. This ensures that the amount of time required for each integration step is constant. Therefore only fixed-step integration methods are considered.

2.4.1 Runge-Kutta

The Runge-Kutta class of numerical integrators are designed to integrate equations of the form

$$\dot{\mathbf{x}} = \mathbf{f}(\mathbf{x}, t). \quad (2.57)$$

While acceleration is generally expressed as a second-order differential equation, if a state vector containing position and velocity is introduced, the result is a series of first-order differential equations suitable for a Runge-Kutta integrator. Equations (2.4), (2.11), and (2.17) show this transformation. A 4th order Runge-Kutta integrator is used. While higher order versions offer more accuracy, they also increase computation time as more function evaluations are required [12].

2.4.2 Nyström-Lear

The class of Nyström integrators are designed to integrate equations of the form

$$\ddot{\mathbf{x}} = \mathbf{f}(\dot{\mathbf{x}}, \mathbf{x}, t). \quad (2.58)$$

This form is especially suitable for Cowell's and Encke's formulation of the equation of motion. Since the Equinoctial Elements formulation is a set of first-order differential equations, the following substitution must be made

$$\begin{bmatrix} \mathbf{u} \\ \dot{\mathbf{u}} \\ \ddot{\mathbf{u}} \end{bmatrix} = \begin{bmatrix} \int_{t_0}^t \mathbf{x} dt \\ \mathbf{x} \\ \dot{\mathbf{x}} \end{bmatrix}. \quad (2.59)$$

An NLZD4/4 belonging to the Nyström integrator family is considered [17]. It has the capability of providing higher accuracy than the RK4 while requiring the same number of function evaluations within an integration step.

A comparison between the RK4 and NLZD4/4 involving relatively simple functions is provided in Appendix B. A series of first and second-order linear differential equations are integrated using both approaches to compare their accuracy. The results shown in Appendix B do not necessarily extend to the non-linear differential equations involved in orbit propagation.

CHAPTER 3

SGP4

3.1 Background

SGP4 is based on the analytic theories of Kozai and Brouwer, who independently developed solutions for the motion of a LEO satellite under the influence of the zonal harmonics J_2 , J_3 , J_4 , and J_5 [6, 8, 18]. These solutions were derived using a variation of parameters approach. Averaging techniques, series expansions, and other approximations were used to arrive at closed-form solutions. In addition to gravitational perturbations, SGP4 includes a density model based on the work of Lane and Cranford [19].

Initially, the perturbations modeled by SGP4 consisted of only zonal gravitational terms (up to J_4) and drag. As Molniya and geosynchronous orbits became more common, deep space modeling was integrated into SGP4 [18]. This included the lunisolar effects and resonance effects of Earth tesseral harmonics developed by Bowman and Hujsak [20, 21]. Older documents may refer to this additional modeling as SDP4 [9]. However, more recent revisions in text and computer code maintain the name SGP4 (or the combined SGP4/SDP4) for both near-Earth and deep space propagation. The addition of deep space modeling completed the SGP4 propagator in use today [18].

3.2 Perturbation Effects

In contrast to equation (2.1), analytical propagators have unique formulations that encompass a fixed set of approximated perturbations. Rather than modeling a perturbing acceleration, SGP4 models the effect of perturbations on orbital elements to describe orbital motion. The changes in orbital elements due to perturbations can be categorized as secular, long-period, or short-period. As summarized in Table 3.1, SGP4 models different sets of perturbation effects depending on the orbit.

Table 3.1: SGP4 perturbation effects for different orbit conditions.

Orbit Conditions	Perturbation Effects
nominal ($P < 225$ min)	secular: J_2, J_2^2, J_4 , drag long-period: J_2, J_3 short-period: J_2
$P \geq 225$ min	secular: J_2, J_2^2, J_4 , drag, lunisolar long-period: J_2, J_3 , lunisolar short-period: J_2
$680 \text{ min} < P < 760 \text{ min}$ AND $e > 0.5$	secular: $J_2, J_2^2, J_{2,2}, J_{3,2}, J_4, J_{4,4}, J_{5,2}, J_{5,4}$, drag, lunisolar long-period: J_2, J_3 , lunisolar short-period: J_2
$1200 \text{ min} < P < 1800 \text{ min}$	secular: $J_2, J_2^2, J_{2,2}, J_{3,1}, J_{3,3}, J_4$, drag (if B^* drag coefficient $\neq 0$), lunisolar long-period: J_2, J_3 , lunisolar short-period: J_2

3.3 Overview

The input to SGP4 is a TLE set containing mean orbital elements, and a time interval specified in minutes. The algorithm performs a check on orbital period and eccentricity to determine which perturbations to include. The output of SGP4 is a state vector at the desired time coordinatized in an inertial TEME frame. The conversion between the TEME and J2000 frames is discussed in Section A.2.

For brevity, the SGP4 equations are not included in this document. A comprehensive set of equations are provided in [9, 18]. Computer code and verification test cases are provided in [22].

CHAPTER 4
PROCEDURE

4.1 Overview

Numerical propagation methods and SGP4 were compared to a truth ephemeris for predictions made up to 7 days. Accuracy and timing metrics were compiled for each type of orbit. The orbits were LEO, GEO, GTO, Molniya, and the 2nd phase of NASA’s MMS mission [23]. LEO and GEO were near circular; GTO, Molniya, and MMS were highly elliptical. The epoch for every numerically propagated orbit was 1/1/17 00:00:00 UTC. The epoch for every orbit propagated with SGP4 was 1/8/17 00:00:00 UTC (see Section 4.5). Table 4.1 shows the initial classical orbital elements and initial perigee and apogee altitudes for each orbit type. Every orbit had $\Omega_0 = 0^\circ$ and $\theta_0 = 0^\circ$.

Table 4.1: Initial classical orbital elements (0 if not specified) and initial perigee and apogee altitudes for each orbit.

Orbit	Initial Classical Orbital Elements				Initial Altitudes	
	a_0 (km)	e_0	i_0 (deg)	ω_0 (deg)	z_p (km)	z_a (km)
LEO	6878.137	0.001	28.5	0	493.122	506.878
GEO	42164.000	0.0001	1.0	0	35781.647	35790.079
Molniya	26561.762	0.7034	63.4	270	1500.000	38867.251
GTO	24396.069	0.7283	28.5	0	250.000	35785.863
MMS	84103.137	0.8938	28.0	0	2550.000	152900.000

4.2 Truth Ephemeris Generation

A set of high fidelity truth ephemerides was necessary for reliable analysis. Each truth ephemeris was propagated numerically with a step size that yielded negligible integrator

error. To determine the proper step size, first a numerically propagated 2-body orbit was compared to a Kepler routine with the same initial conditions. Cowell's formulation with a RK4 was used for numerical propagation (Encke and Equinoctial Elements rely on a perturbing acceleration). The position error after 7 days was then plotted as a function of number of integration steps (step size). Figure 4.1 below shows this process applied to GEO.

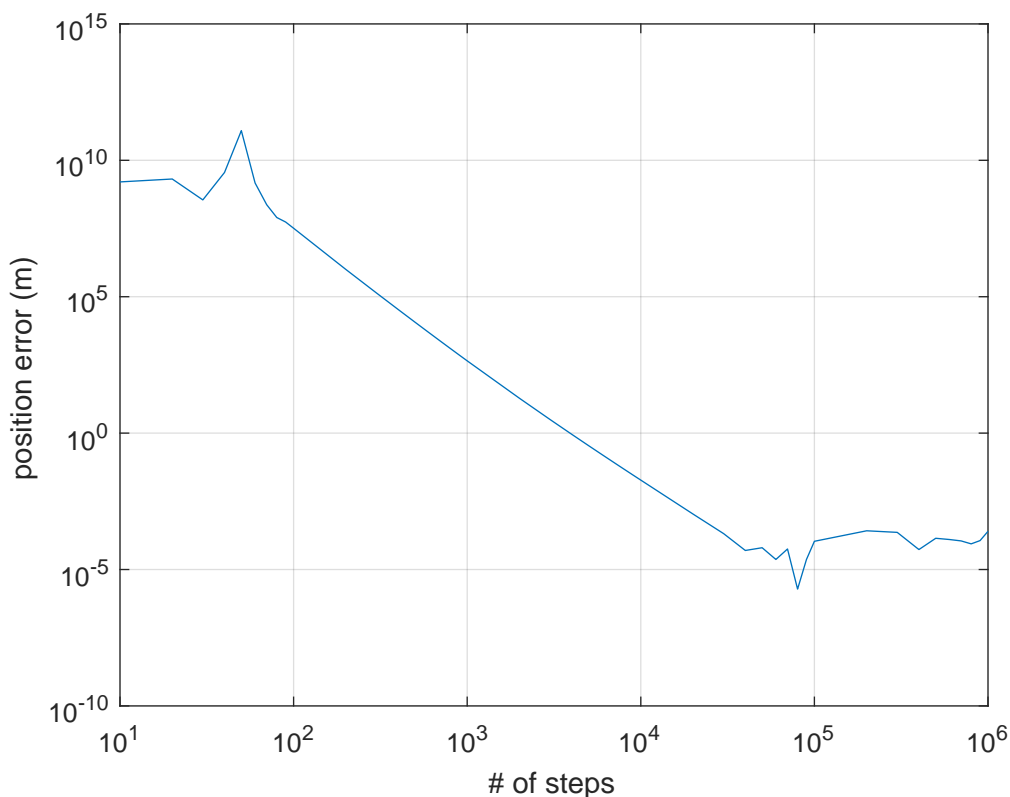


Fig. 4.1: Position error after 7 days as a function of number of integration steps for GEO.

The error trend in Figure 4.1 is characteristic of a Runge-Kutta integrator. Large step sizes (too few integration steps) lead to approximation error, where the numerical integration scheme fails to produce an accurate approximation of the function. Excessively small step sizes (too many integration steps) result in errors caused by the effects of finite

machine precision. By plotting error versus number of steps on a log-log scale, appropriate step sizes are identified by a straight line with a slope approximately equal to the order of the integrator [2]. The step size that reliably yields the lowest integrator error occurs where the error plateaus immediately after the straight line. This method was repeated for each orbit type. The results are summarized in Table 4.2.

Table 4.2: Number of integration steps and corresponding time step (assuming a final time of 7 days) used for the truth ephemeris generation of each orbit.

Orbit	# of Steps	Time Step (s)
LEO	5×10^5	1.2096
GEO	4×10^4	15.120
Molniya	4×10^5	1.512
GTO	4×10^5	1.512
MMS	3×10^5	2.016

Each truth ephemeris also included a relevant environment model. The environment models chosen for each orbit are listed in Table 4.3.

Table 4.3: Environment models used for each orbit.

Orbit	Environment Model
LEO	18×18 gravity, lunisolar, SRP, drag
GEO	4×4 gravity, lunisolar, SRP
Molniya	8×8 gravity, lunisolar, SRP
GTO	8×8 gravity, lunisolar, SRP, drag ($h_{ellp} < 1000$ km)
MMS	8×8 gravity, lunisolar, SRP

The basis for these models was Figure 3.1 from [12] which plots the approximate relative acceleration of various perturbations as a function of distance from the center of the Earth.

However, adhering to the results from this plot was less important than model accuracy. For example, given the LEO initial conditions in Table 4.1, [12] suggests that dynamic solid tides have a greater perturbing effect than SRP. Dynamic solid tides were ultimately neglected for this analysis due to a lack of confidence in accurate modeling and implementation. In other words, there is high confidence in the accuracy of each environment model component and its implementation.

4.3 Performance Metrics

The following metrics were used to compare the performance of each propagator. They provide a concise and consistent analysis of accuracy and computation requirements for each propagator.

4.3.1 Magnitude of Position Difference

The magnitude of the position difference, also referred to as the position error, is

$$e_r(t) = \|\mathbf{r}(t) - \mathbf{r}_t(t)\|. \quad (4.1)$$

It was stored as a function of time. Two key plots could be shown with this metric: the position error as a function of time, and a position error at a specific time as a function of number of integration steps.

4.3.2 Number of Integration Steps

For numerical propagation, a timing metric independent of processing power is number of integration steps. For consistency across all differential equation formulations, the number of integration steps is used in place of time steps because Encke-beta has no defined time step.

4.3.3 Normalized Computation Time

Another timing metric independent of processing power is normalized computation

time. This metric is used to compare the time required for each numerical propagator to completed one integration step with the runtime of SGP4. Results are normalized to SGP4 runtime.

4.4 Numerical Propagation Specifics

The following steps summarize the numerical propagation procedure.

1. A propagator was specified by selecting a differential equation formulation and an integrator. The environment model corresponded to the orbit type.
2. An initial state vector corresponding to the orbit type was propagated forward 7 days over a range of step sizes listed in Table 4.4.
3. Position error between the propagated and truth ephemerides was calculated using equation (4.1).

Table 4.4: Range of number of integration steps and corresponding range of time steps (assuming a final time of 7 days) for each orbit.

Orbit	# of Steps Range	Time Step Range (s)
LEO	$1 \times 10^3 - 1 \times 10^5$	604.8 – 6.048
GEO	$1 \times 10^2 - 1 \times 10^4$	6048 – 60.48
Molniya	$1 \times 10^3 - 1 \times 10^5$	604.8 – 6.048
GTO	$1 \times 10^3 - 1 \times 10^5$	604.8 – 6.048
MMS	$1 \times 10^3 - 1 \times 10^5$	604.8 – 6.048

4.5 SGP4 Propagation Specifics

The following steps summarize the SGP4 propagation procedure.

1. The truth ephemeris for each orbit was propagated an additional 7 days, in total spanning 1/1/17 00:00:00 UTC to 1/15/17 00:00:00 UTC.

2. Using STK's TLE generator, TLE sets were created using sample points from truth ephemeris data spanning 1/1/17 00:00:00 UTC to 1/8/17 00:00:00 UTC. The fit lengths varied, but the final sample point was always set to 1/8/17 00:00:00 UTC. For example, a 3-day fit spanned 1/5 to 1/8, and a 1-day fit spanned 1/7 to 1/8.
3. The TLE sets were input into SGP4 and propagated forward 7 days. Although propagation with these methods can be accomplished in only one step, a time interval matching the truth ephemeris was used to analyze position error over time.
4. Position error between the propagated and truth ephemerides was calculated using equation (4.1).

CHAPTER 5
LEO RESULTS

5.1 Numerical Propagation

Figures 5.1 and 5.2 show comparisons between differential equation formulations, numerical integration schemes, and number of integration steps (step size). For this LEO model, the initial state is listed in Table 4.1, and the environment model is listed in Table 4.3. The step size used for propagating the truth ephemeris is listed in Table 4.2.

Figure 5.1 shows position error as a function of time for each differential equation formulation. Position error is calculated using equation (4.1). Differential equation formulations are indicated by color. For Encke-time and Encke-beta, solid lines indicate rectification at every step, dashed lines indicate a 0.01% rectification tolerance, and dotted lines indicate a 0.1% rectification tolerance. The plots in the left column show results using the RK4. The plots in the right column show results using the NLZD4/4. The plots in the upper row show results using 10^4 integration steps over the 7 day propagation period, which corresponds to a time step of 60.48 s. The plots in the lower row show results using 10^3 integration steps, which corresponds to a time step of 604.8 s.

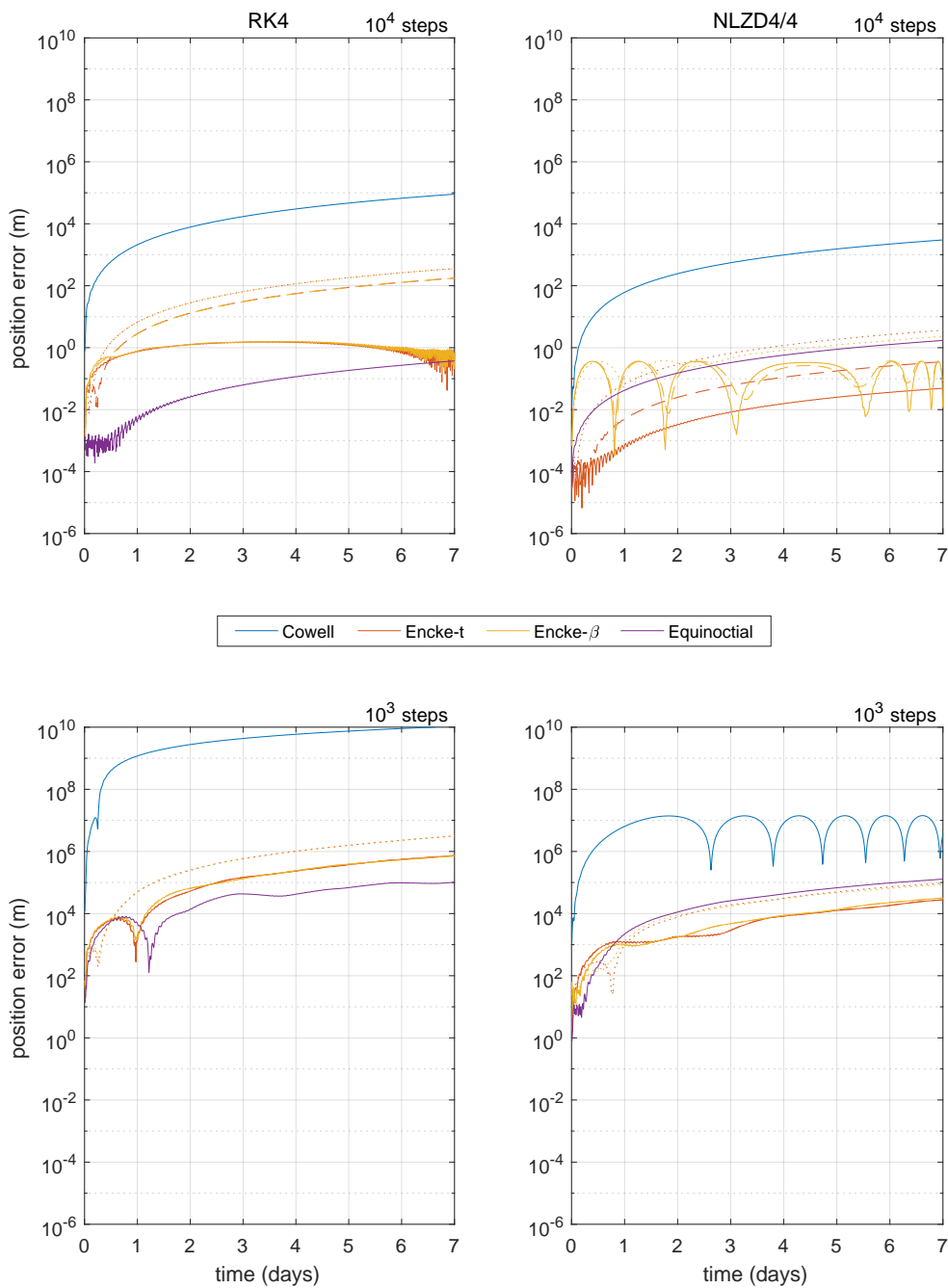


Fig. 5.1: LEO position error as a function of time for each differential equation formulation. Line textures for Encke formulations indicate the following rectification tolerances: solid = 0% (every step), dashed = 0.01%, dotted = 0.1%. The left column shows RK4 results and the right column shows NLZD4/4 results. The upper row shows results using 10^4 integration steps and the lower row shows results using 10^3 integration steps.

Figure 5.1 shows that for this LEO model, the formulation and integrator consistently providing the highest position accuracy for 10^4 integration steps over 7 days ($\Delta t = 60.48$ s) is Encke-time rectified every step with the NLZD4/4. The formulations and integrator consistently providing the highest position accuracy for 10^3 integration steps over 7 days ($\Delta t = 604.8$ s) are Encke-time and Encke-beta rectified every step with the NLZD4/4. For these step sizes, Encke and Equinoctial Elements provide significantly higher position accuracy than Cowell regardless of integrator, and the NLZD4/4 provides higher position accuracy than the RK4 for all formulations excluding Equinoctial Elements.

Position error generally grows with time. Oscillations in the position error are also common. Some Encke and Equinoctial Elements results have oscillations with a period equal to the orbital period (≈ 15 per day). This is likely due to low-order terms within the gravity field model contributing to periodic perturbations, as approximation errors of a periodic function are typically periodic. Oscillations with higher frequencies may be due to higher-order terms within the gravity field model, however their exact cause is not fully understood. There is also no current explanation for unusual swoops shown by some formulations with the NLZD4/4.

Figure 5.2 shows position error after 7 days as a function of number of integration steps. The number of integration steps spans two decades with samples taken at each minor tick mark. A corresponding time step is also listed. It is rounded simply to keep a cleaner appearance. The color schemes and line textures used in Figure 5.2 are the same as Figure 5.1. The upper plot shows results using the RK4. The lower plot shows results using the NLZD4/4.

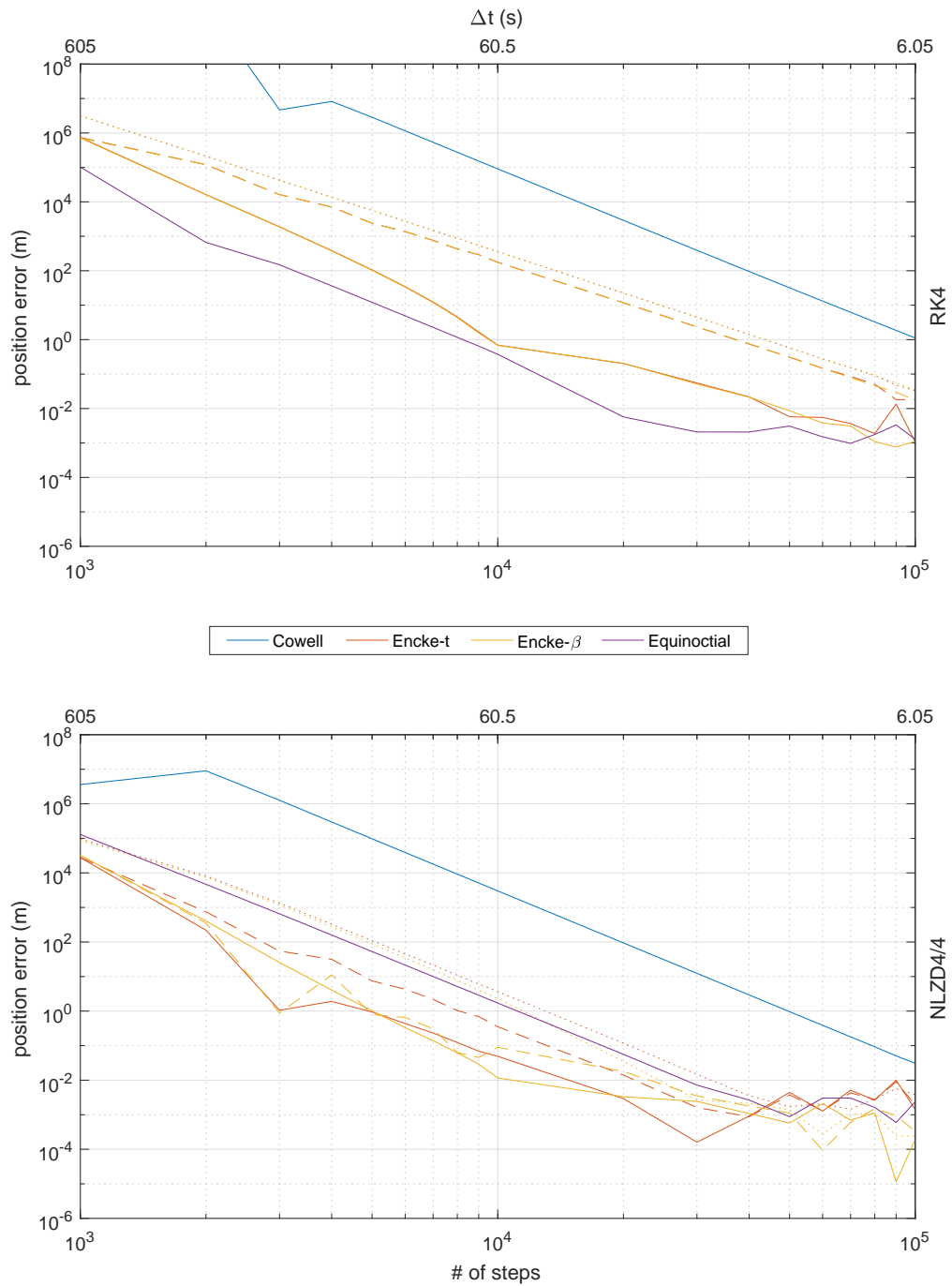


Fig. 5.2: 7 day LEO position error as a function of number of integration steps for each differential equation formulation. Line textures for Encke formulations indicate the following rectification tolerances: solid = 0% (every step), dashed = 0.01%, dotted = 0.1%. The upper plot shows RK4 results and the lower plot shows NLZD4/4 results.

Figure 5.2 confirms that for this LEO model, the formulations and integrator consistently providing the highest position accuracy is Encke-time and Encke-beta rectified every step with the NLZD4/4. It also confirms that Encke and Equinoctial Elements provide significantly higher position accuracy than Cowell regardless of integrator, and the NLZD4/4 provides higher position accuracy than the RK4 for all formulations excluding Equinoctial Elements.

Plateaus in position error indicate a region where further reductions in step size yield no reliable accuracy increase. For Encke and Equinoctial Elements with the NLZD4/4, this plateau generally occurs around 5×10^4 integration steps, which corresponds to a time step of about 12s. While the location of this plateau is dependent on final propagation time, Figure 5.2 shows how a minimum step size can be determined for any numerical propagator.

It is interesting that the NLZD4/4 does not provide higher position accuracy than the RK4 for Equinoctial Elements. The NLZD4/4 reduces to a first-order integrator for these equations. The structure of the RK4 and the reduced NLZD4/4 is identical for first-order differential equation integration (a weighted mean of four function evaluations). They differ by the intervals between function evaluations and the weights placed on them. Results from Figure 5.2 show that that intervals and weights used by the RK4 are better suited for approximating the Equinoctial Elements functions in this LEO model. More research is needed to determine if this is an anomaly, or if there are classes of first-order functions that perform worse with the NLZD4/4.

The NLZD4/4 seems to affect the agreement between Encke-time and Encke-beta position error. The upper plot of Figure 5.2 shows results from the two formulations almost overlapping. This is expected for low eccentricity orbits where equal time steps are mapped to nearly equal steps in universal anomaly. The lower plot shows less agreement between the two formulations. There is no current explanation for this discrepancy.

5.2 SGP4

Figure 5.3 shows position error as a function of time using SGP4. The start and end times of a set of sample points used to generate TLEs, referred to as fit lengths, are indicated by color. A "0 day" fit refers to a TLE generated from a single state vector.

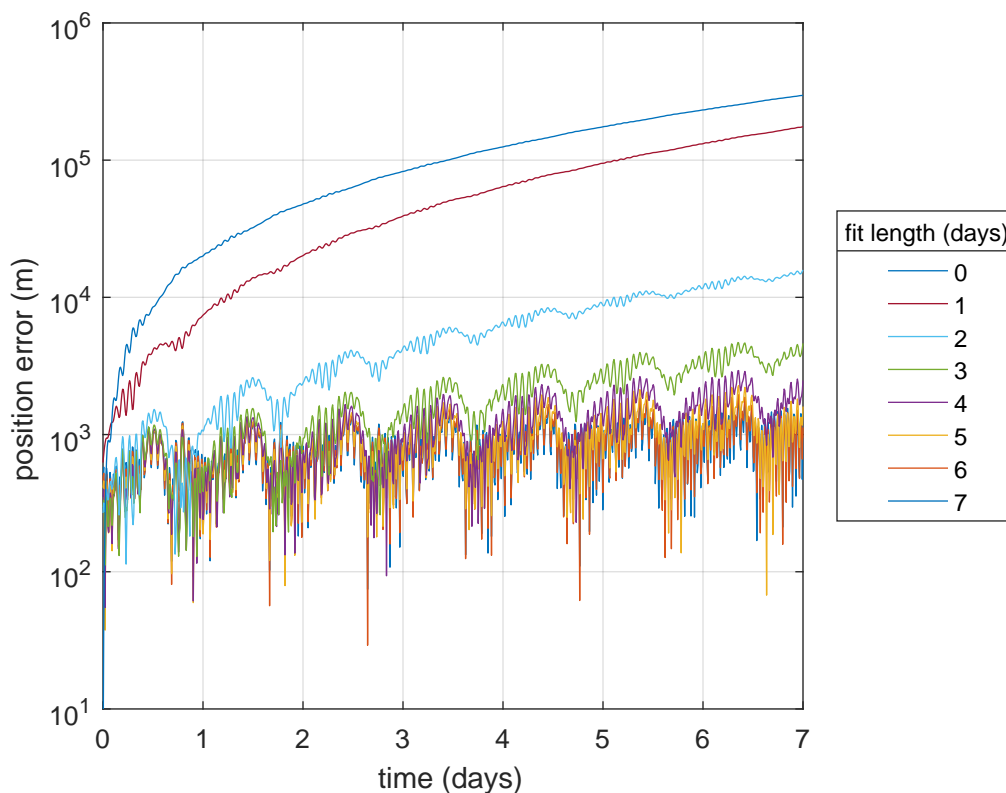


Fig. 5.3: LEO position error as a function of time for different TLE fit lengths. A "0 day" fit refers to a TLE generated from a single state vector.

Figure 5.3 shows that SGP4 can provide relatively accurate position predictions given an adequate number of sample points for TLE generation. Fit length and accuracy are proportional, although accuracy only improves marginally once a sufficient fit length is reached. This plot suggests that a minimum 2 day fit – equivalent to sample points over approximately 30 orbits – is required for position error on the order of 1 km.

Position error shown in Figure 5.3 is relative to the truth ephemeris generated for this

particular LEO model. While the environment model captures dominant perturbations, it is not comprehensive. Position errors with respect to a higher order truth model may not match the results shown in Figure 5.3.

5.3 Accuracy Comparison

Figure 5.4 shows position error after 7 days as a function of number of integration steps. The format and styling of this plot is identical to Figure 5.2, except for an additional line indicating the lowest SGP4 position error from the fit lengths analyzed and displayed in Figure 5.3. This comparison shows how many integration steps are needed to match SGP4 position accuracy for this LEO model. Tables 5.1 and 5.2 list the number of integration steps where the position errors of each differential equation formulation and SGP4 intersect.

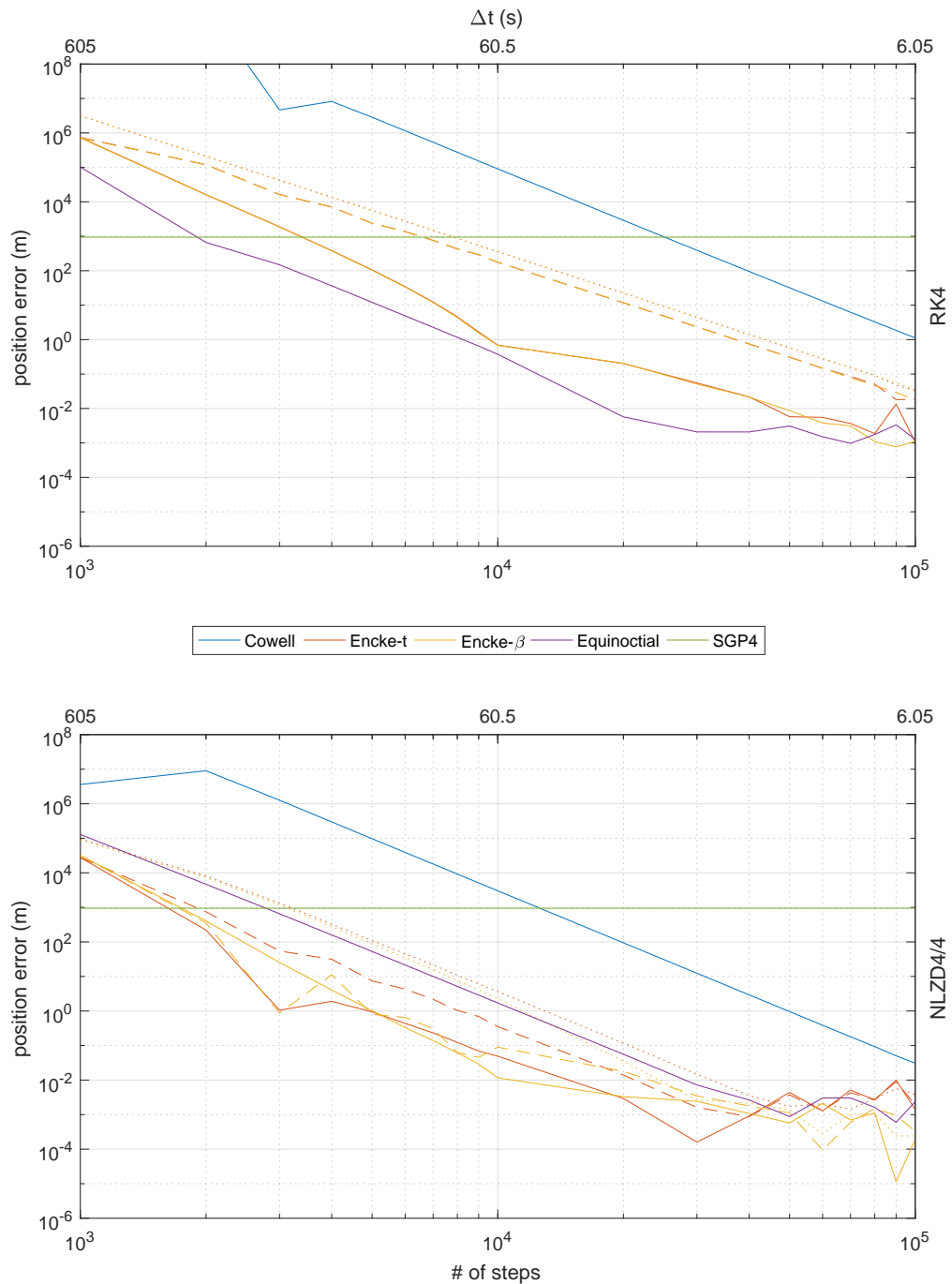


Fig. 5.4: Comparison of 7 day LEO position error between numerical propagators and SGP4. Line textures for Encke formulations indicate the following rectification tolerances: solid = 0% (every step), dashed = 0.01%, dotted = 0.1%. The upper plot shows RK4 results and the lower plot shows NLZD4/4 results.

Table 5.1: Number of integration steps and corresponding time step (if available) required by each differential equation formulation with the RK4 to match the 7 day LEO position accuracy of SGP4.

Formulation	# of Steps	Time Step (s)
Cowell	2.5×10^4	24.2
Encke-time (0%)	3.4×10^3	177.9
Encke-time (0.01%)	6.5×10^3	93.0
Encke-time (0.1%)	8×10^3	75.6
Encke-beta (0%)	3.4×10^3	N/A
Encke-beta (0.01%)	6.5×10^3	N/A
Encke-beta (0.1%)	8×10^3	N/A
Equinoctial Elements	1.9×10^3	318.3

Table 5.2: Number of integration steps and corresponding time step (if available) required by each differential equation formulation with the NLZD4/4 to match the 7 day LEO position accuracy of SGP4.

Formulation	# of Steps	Time Step (s)
Cowell	1.3×10^4	46.5
Encke-time (0%)	1.6×10^3	378.0
Encke-time (0.01%)	1.9×10^3	318.3
Encke-time (0.1%)	3.3×10^3	183.3
Encke-beta (0%)	1.6×10^3	N/A
Encke-beta (0.01%)	1.7×10^3	N/A
Encke-beta (0.1%)	3.3×10^3	N/A
Equinoctial Elements	2.9×10^3	208.6

5.4 Timing Comparison

Table 5.3 lists the time required for each numerical propagator to complete one integration step normalized to the runtime of SGP4 for this LEO model. The time per integration step is dominated by the perturbing acceleration calculation, which is dictated by the environment model. Changing the perturbations or formulations within the environment model could significantly alter these timing results.

Table 5.3: Time required for one integration step normalized to SGP4 runtime for LEO.

Propagator	Time
SGP4	1
Cowell, RK4	0.3000
Cowell, NLZD4/4	0.3000
Encke-time, RK4	0.3114
Encke-time, NLZD4/4	0.3114
Encke-beta, RK4	0.3086
Encke-beta, NLZD4/4	0.3086
Equinoctial Elements, RK4	0.3114
Equinoctial Elements, NLZD4/4	0.3114

Forming the differential equations using Cowell requires the fewest calculations, so naturally it takes the least amount of time. The RK4 and NLZD4/4 timing is consistent across all formulations.

Table 5.3 shows that for any numerical propagation method, only 3 full integration steps can be taken before exceeding the runtime of SGP4. There are two contributing factors: the extensive LEO environment model used in numerical propagation, and the limited number of LEO perturbing effects modeled by SGP4 (see table 3.1).

CHAPTER 6
GEO RESULTS

6.1 Numerical Propagation

Figures 6.1 and 6.2 show comparisons between differential equation formulations, numerical integration schemes, and number of integration steps (step size). For this GEO model, the initial state is listed in Table 4.1, and the environment model is listed in Table 4.3. The step size used for propagating the truth ephemeris is listed in Table 4.2.

Figure 6.1 shows position error as a function of time for each differential equation formulation. Position error is calculated using equation (4.1). Differential equation formulations are indicated by color. For Encke-time and Encke-beta, solid lines indicate rectification at every step, dashed lines indicate a 0.01% rectification tolerance, and dotted lines indicate a 0.1% rectification tolerance. The plots in the left column show results using the RK4. The plots in the right column show results using the NLZD4/4. The plots in the upper row show results using 10^3 integration steps over the 7 day propagation period, which corresponds to a time step of 604.8 s. The plots in the lower row show results using 10^2 integration steps, which corresponds to a time step of 6048 s.

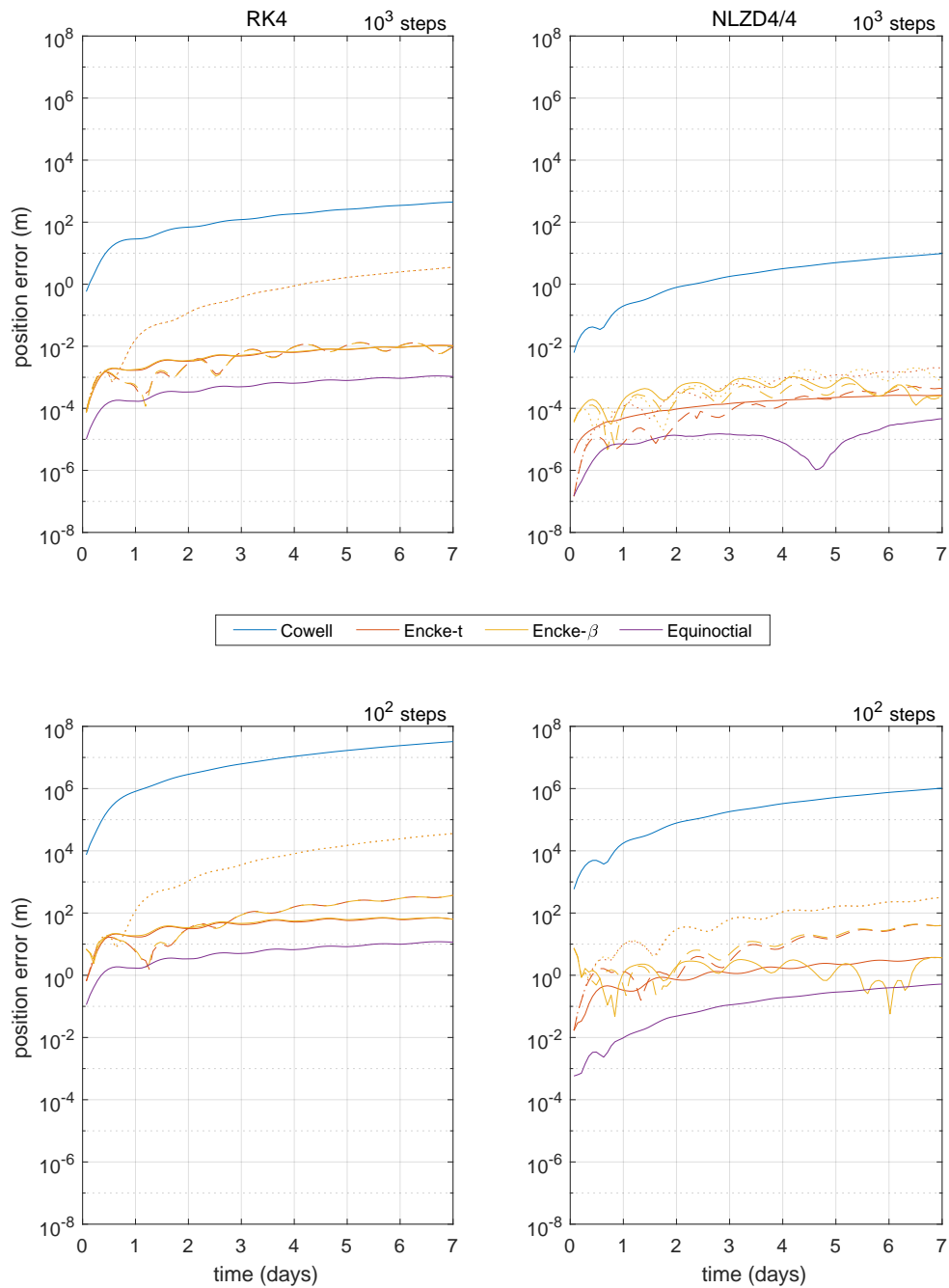


Fig. 6.1: GEO position error as a function of time for each differential equation formulation. Line textures for Encke formulations indicate the following rectification tolerances: solid = 0% (every step), dashed = 0.01%, dotted = 0.1%. The left column shows RK4 results and the right column shows NLZD4/4 results. The upper row shows results using 10^3 integration steps and the lower row shows results using 10^2 integration steps.

Figure 6.1 shows that for this GEO model, the formulation and integrator consistently providing the highest position accuracy for 10^3 and 10^2 integration steps over 7 days ($\Delta t = 604.8$ s and $\Delta t = 6048$ s) is Equinoctial Elements with the NLZD4/4. For these step sizes, Encke and Equinoctial Elements provide significantly higher position accuracy than Cowell regardless of integrator, and the NLZD4/4 provides higher position accuracy than the RK4 for all formulations.

Position error generally grows with time. Oscillations in the position error are also common. Nearly all formulations have some oscillations with a period equal to the orbital period. This is due to periodic orbital motion, in the case of Cowell, and periodic motion produced by the gravity field model, in the cases of Encke and Equinoctial Elements, as approximation errors of periodic functions are typically periodic. Shorter periods shown by some Encke formulations may be due to higher-order terms within the gravity field model, however their exact cause is not fully understood.

Figure 6.2 shows position error after 7 days as a function of number of integration steps. The number of integration steps spans two decades with samples taken at each minor tick mark. A corresponding time step is also listed. It is rounded simply to keep a cleaner appearance. The color schemes and line textures used in Figure 6.2 are the same as Figure 6.1. The upper plot shows results using the RK4. The lower plot shows results using the NLZD4/4.

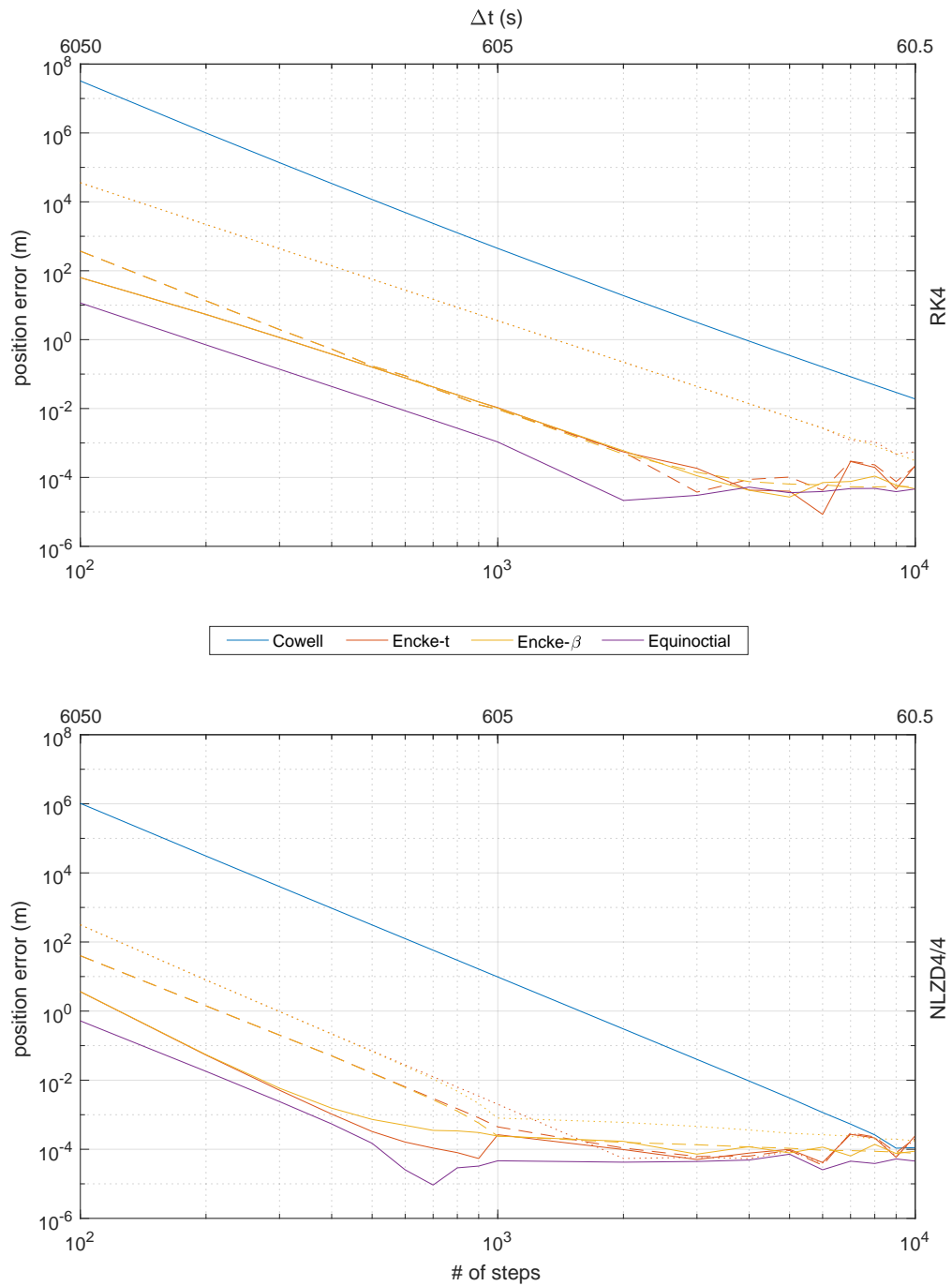


Fig. 6.2: 7 day GEO position error as a function of number of integration steps for each differential equation formulation. Line textures for Encke formulations indicate the following rectification tolerances: solid = 0% (every step), dashed = 0.01%, dotted = 0.1%. The upper plot shows RK4 results and the lower plot shows NLZD4/4 results.

Figure 6.2 confirms that for this GEO model, the formulation and integrator providing the highest position accuracy is Equinoctial Elements with the NLZD4/4. It also confirms that Encke and Equinoctial Elements provide significantly higher position accuracy than Cowell regardless of integrator, and the NLZD4/4 provides higher position accuracy than the RK4 for all formulations.

Plateaus in position error indicate a region where further reductions in step size yield no reliable accuracy increase. For Encke and Equinoctial Elements with the NLZD4/4, this plateau generally occurs around 10^3 integration steps, which corresponds to a time step of about 10 min. While the location of this plateau is dependent on final propagation time, Figure 6.2 shows how a minimum step size can be determined for any numerical propagator.

For second-order differential equation formulations, the NLZD4/4 not only lowers the "intercept" of position error lines, it also slightly increases the slope, indicating the NLZD4/4 achieves an accuracy of higher order than the RK4. This is consistent with the example tested in Section B.2 with the function form $\ddot{x} = f(x, t)$.

Encke-time and Encke-beta yield almost identical results. This is expected for low eccentricity orbits, as equal time steps are mapped to nearly equal steps in universal anomaly. Their overlap is consistent for both integrators.

Rectification tolerance for both Encke formulations has a noticeable impact on position error. The results of each rectification tolerance relative to each other also vary significantly with integrator. More research is needed to determine the cause of these discrepancies.

LEO and GEO results exhibit the same general trends. These trends include Encke and Equinoctial Elements providing accuracy increases by orders of magnitude over Cowell, and Encke-time and Encke-beta yielding similar results. For both orbit models, the NLZD4/4 generally performs better than the RK4.

6.2 SGP4

Figure 6.3 shows position error as a function of time using SGP4. The start and end times of a set of sample points used to generate TLEs, referred to as fit lengths, are indicated by color. A "0 day" fit refers to a TLE generated from a single state vector.

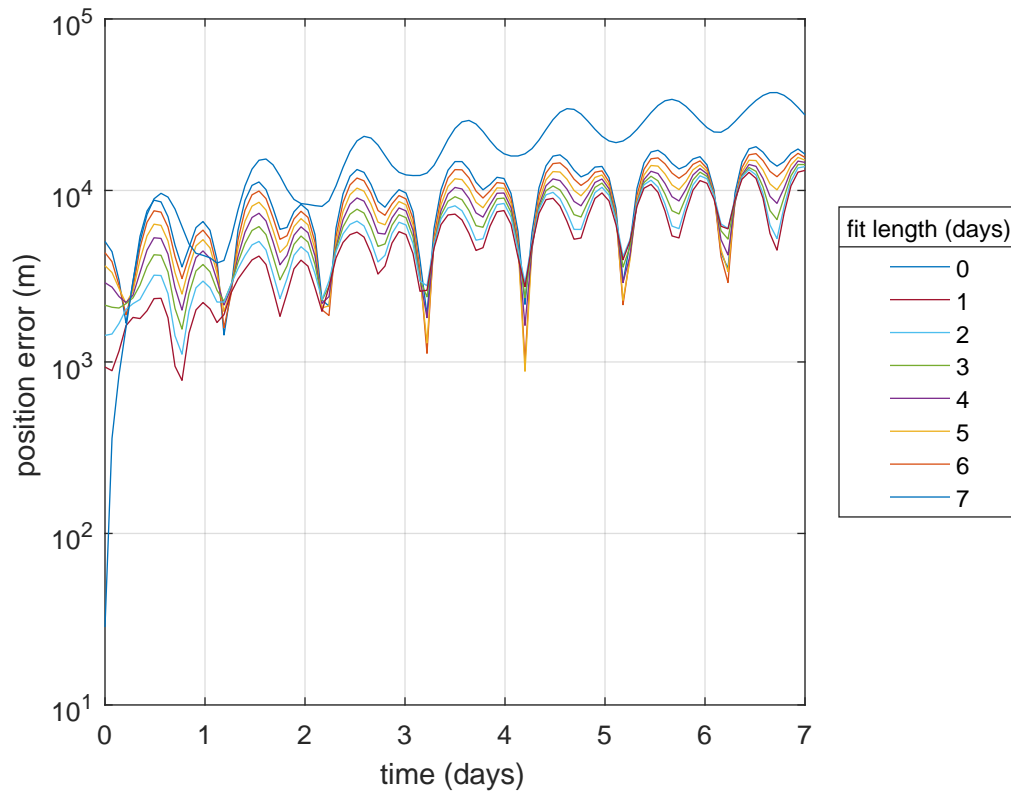


Fig. 6.3: GEO position error as a function of time for different TLE fit lengths. A "0 day" fit refers to a TLE generated from a single state vector.

Figure 6.3 shows that low order modeling of GEO perturbations by SGP4 inherently leads to position error regardless of fit length. The TLE generated from a single state vector yields the highest position error. Excluding the single point fit, the fit length and accuracy are inversely proportional. This indicates that using more ephemeris data to generate a TLE does not ensure higher accuracy for future propagation. In this case, a fit over multiple days accounts for old data that does not accurately describe the current orbit. Since future orbits

will more likely resemble the current orbit as opposed to previous orbits, old data introduces bias to the fit. Of course, there is a balance between selecting only the most recent data and having enough data for a proper fit. Figure 6.3 shows that for GEO propagation, fitting over 1 day (1 orbit) is adequate.

Position error shown in Figure 6.3 is relative to the truth ephemeris generated for this particular GEO model. While the environment model captures dominant perturbations, it is not comprehensive. Position errors with respect to a higher order truth model may not match the results shown in Figure 6.3.

6.3 Accuracy Comparison

Figure 6.4 shows position error after 7 days as a function of number of integration steps. The format and styling of this plot is similar to Figure 6.2, except for an additional line indicating the lowest SGP4 position error from the fit lengths analyzed and displayed in Figure 6.3. Also, another decade of integration steps is added to more clearly see the intersection of numerical propagator and SGP4 results. This comparison shows how many integration steps are needed to match SGP4 position accuracy for this GEO model. Tables 6.1 and 6.2 list the number of integration steps where the position errors of each differential equation formulation and SGP4 intersect.

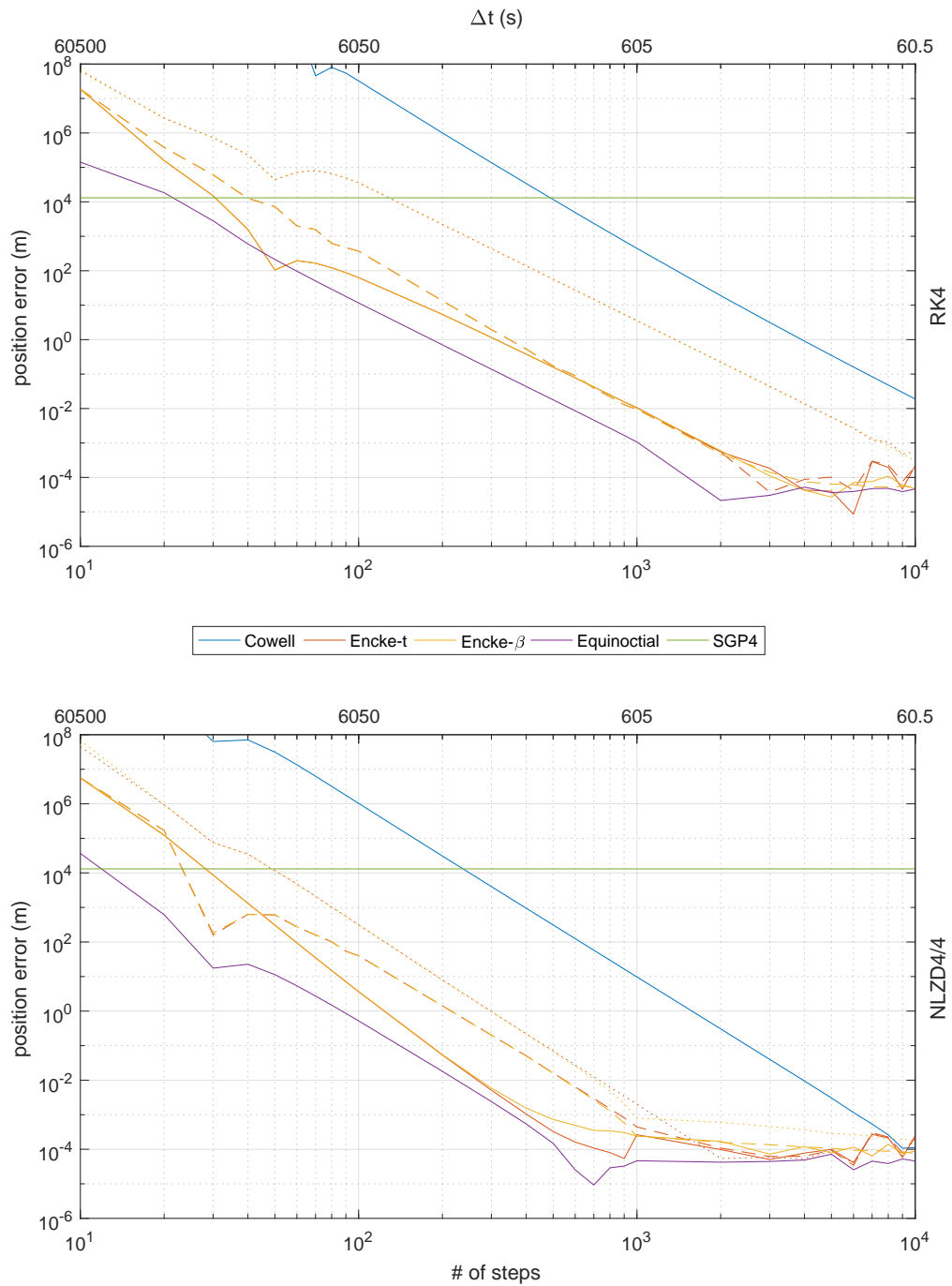


Fig. 6.4: Comparison of 7 day GEO position error between numerical propagators and SGP4. Line textures for Encke formulations indicate the following rectification tolerances: solid = 0% (every step), dashed = 0.01%, dotted = 0.1%. The upper plot shows RK4 results and the lower plot shows NLZD4/4 results.

Table 6.1: Number of integration steps and corresponding time step (if available) required by each differential equation formulation with the RK4 to match the 7 day GEO position accuracy of SGP4.

Formulation	# of Steps	Time Step (min)
Cowell	4×10^2	25.2
Encke-time (0%)	3×10^1	336.0
Encke-time (0.01%)	4×10^1	252.0
Encke-time (0.1%)	1.3×10^2	77.5.
Encke-beta (0%)	3×10^1	N/A
Encke-beta (0.01%)	4×10^1	N/A
Encke-beta (0.1%)	1.3×10^2	N/A
Equinoctial Elements	2.1×10^1	480.0

Table 6.2: Number of integration steps and corresponding time step (if available) required by each differential equation formulation with the NLZD4/4 to match the 7 day GEO position accuracy of SGP4.

Formulation	# of Steps	Time Step (min)
Cowell	2.4×10^2	2520
Encke-time (0%)	2.9×10^1	347.6
Encke-time (0.01%)	2.4×10^1	420.0
Encke-time (0.1%)	5×10^1	201.6
Encke-beta (0%)	2.9×10^1	N/A
Encke-beta (0.01%)	2.4×10^1	N/A
Encke-beta (0.1%)	5×10^1	N/A
Equinoctial Elements	1.3×10^1	775.4

6.4 Timing Comparison

Table 6.3 lists the time required for each numerical propagator to complete one integration step normalized to the runtime of SGP4 for this GEO model. The time per integration step is dominated by the perturbing acceleration calculation, which is dictated by the environment model. Changing the perturbations or formulations within the environment model could significantly alter these timing results.

Table 6.3: Time required for one integration step normalized to SGP4 runtime for GEO.

Propagator	Time
SGP4	1
Cowell, RK4	0.0779
Cowell, NLZD4/4	0.0779
Encke-time, RK4	0.0811
Encke-time, NLZD4/4	0.0811
Encke-beta, RK4	0.0800
Encke-beta, NLZD4/4	0.0800
Equinoctial Elements, RK4	0.0811
Equinoctial Elements, NLZD4/4	0.0811

Forming the differential equations using Cowell requires the fewest calculations, so naturally it takes the least amount of time. The RK4 and NLZD4/4 timing is consistent across all formulations.

Table 6.3 shows that for any numerical propagation method, about 12 full integration steps can be taken before exceeding the runtime of SGP4. Comparing with Table 5.3 demonstrates the dependency of computation time on the environment model. The normalized time per step is also lowered due to additional GEO perturbation effects modeled by SGP4 (see table 3.1). Analyzing Tables 6.2 and 6.3 indicates that Equinoctial Elements can achieve nearly the same accuracy as SGP4 for the same runtime.

CHAPTER 7
MOLNIYA RESULTS

7.1 Numerical Propagation

Figures 7.1 and 7.2 show comparisons between differential equation formulations, numerical integration schemes, and number of integration steps (step size). For this Molniya orbit model, the initial state is listed in Table 4.1, and the environment model is listed in Table 4.3. The step size used for propagating the truth ephemeris is listed in Table 4.2.

Figure 7.1 shows position error as a function of time for each differential equation formulation. Position error is calculated using equation (4.1). Differential equation formulations are indicated by color. For Encke-time and Encke-beta, solid lines indicate rectification at every step, dashed lines indicate a 0.01% rectification tolerance, and dotted lines indicate a 0.1% rectification tolerance. The plots in the left column show results using the RK4. The plots in the right column show results using the NLZD4/4. The plots in the upper row show results using 10^4 integration steps over the 7 day propagation period, which corresponds to a time step of 60.48 s. The plots in the lower row show results using 10^3 integration steps, which corresponds to a time step of 604.8 s.

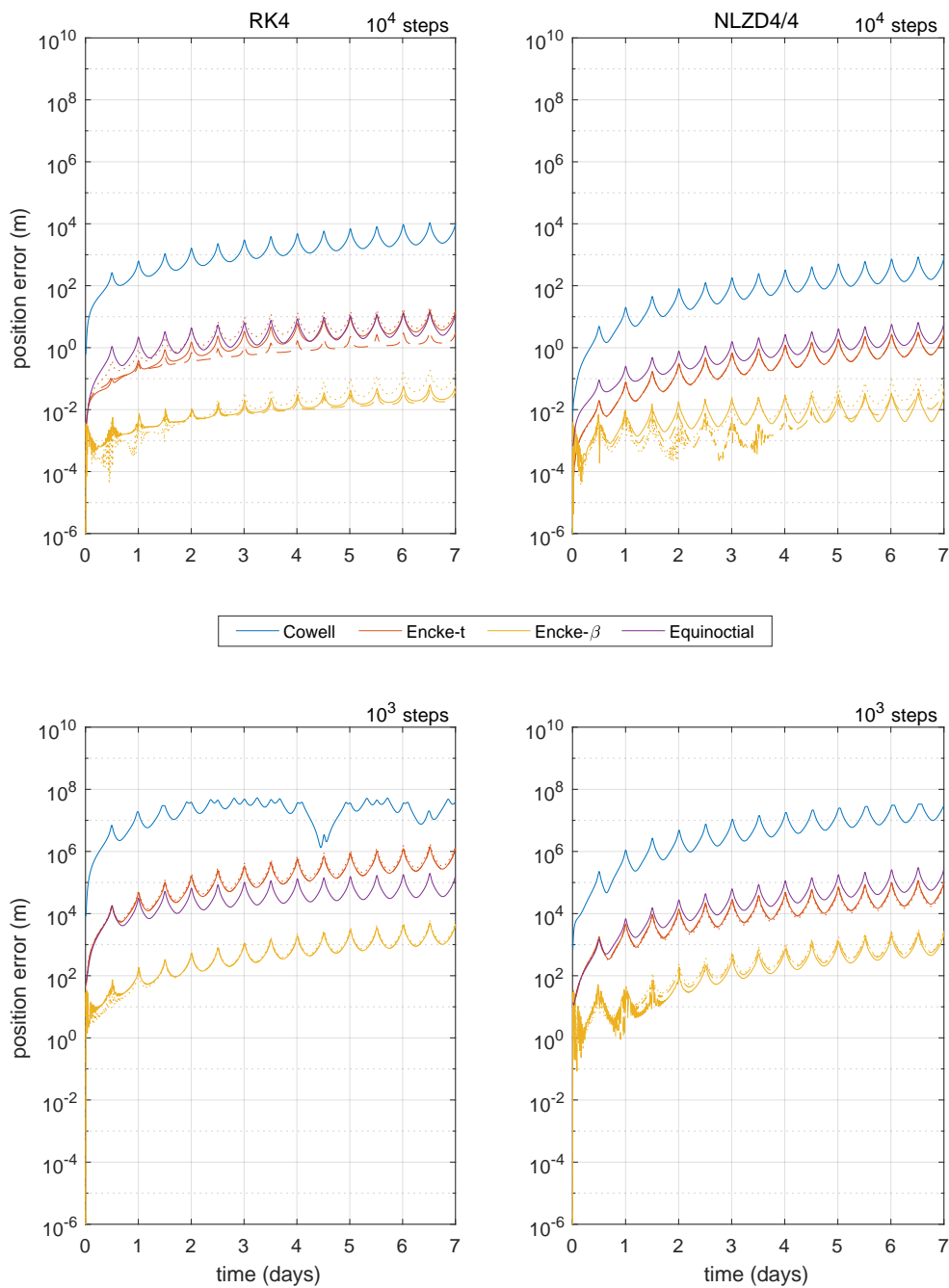


Fig. 7.1: Molniya position error as a function of time for each differential equation formulation. Line textures for Encke formulations indicate the following rectification tolerances: solid = 0% (every step), dashed = 0.01%, dotted = 0.1%. The left column shows RK4 results and the right column shows NLZD4/4 results. The upper row shows results using 10^4 integration steps and the lower row shows results using 10^3 integration steps.

Figure 7.1 shows that for this Molniya orbit model, the formulation and integrator consistently providing the highest position accuracy for 10^4 and 10^3 integration steps over 7 days ($\Delta t = 60.48$ s and $\Delta t = 604.8$ s) is Encke-beta rectified every step with the NLZD4/4. Encke-beta provides significantly higher accuracy than all other formulations because the time-regularized distribution of integration steps replaces unnecessary steps around apogee with additional steps around perigee (see Section 2.2.2). The NLZD4/4 consistently provides more position accuracy than the RK4 for all formulations excluding Equinoctial Elements.

Position error generally grows with time. Swoops in the position error occur at a period equal to the orbital period (2 per day). These swoops are the result of integration step distribution, integration error direction, and elliptical orbital motion. For a more detailed explanation, see Appendix C.

Figure 7.2 shows position error after 7 days as a function of number of integration steps. The number of integration steps spans two decades with samples taken at each minor tick mark. A corresponding time step is also listed. It is rounded simply to keep a cleaner appearance. The color schemes and line textures used in Figure 7.2 are the same as Figure 7.1. The upper plot shows results using the RK4. The lower plot shows results using the NLZD4/4.

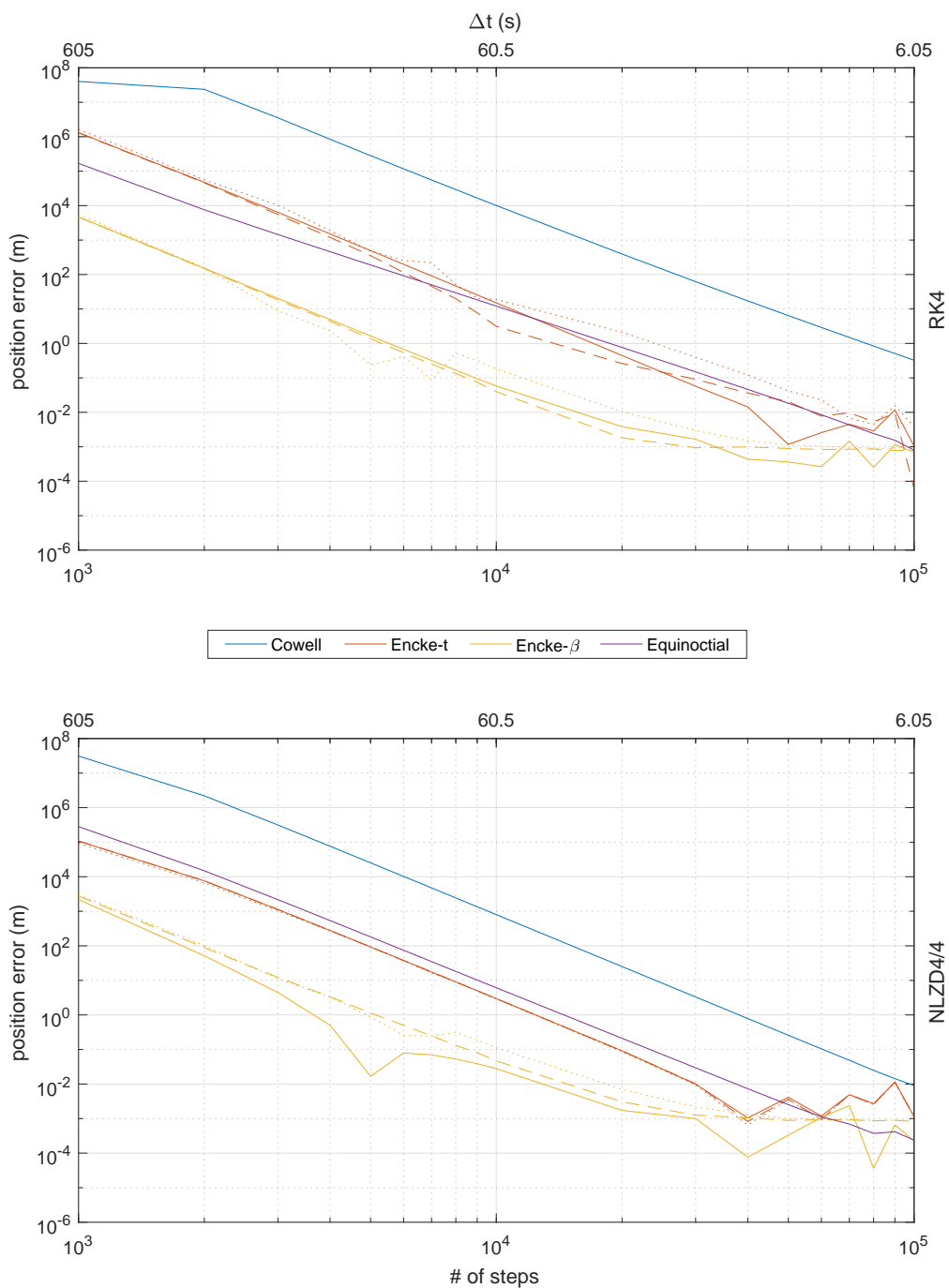


Fig. 7.2: 7 day Molniya position error as a function of number of integration steps for each differential equation formulation. Line textures for Encke formulations indicate the following rectification tolerances: solid = 0% (every step), dashed = 0.01%, dotted = 0.1%. The upper plot shows RK4 results and the lower plot shows NLZD4/4 results.

Figure 7.2 confirms that for this Molniya orbit model, the formulation and integrator providing the highest position accuracy is Encke-beta rectified every step with the NLZD4/4. It also confirms that Encke-beta for every rectification tolerance provides significantly higher position accuracy than all other formulations regardless of integrator, and the NLZD4/4 consistently provides higher position accuracy than the RK4 for all formulations excluding Equinoctial Elements.

Plateaus in position error indicate a region where further reductions in step size yield no reliable accuracy increase. For Encke-beta, this plateau occurs around 2×10^4 integration steps, which corresponds to a time step of about 30 s. While the location of this plateau is dependent on final propagation time, Figure 7.2 shows how a minimum step size can be determined for any numerical propagator.

For second-order differential equation formulations, the NLZD4/4 only lowers the "intercept" of these lines, despite having the form $\ddot{x} = f(x, t)$. In the GEO scenario (see Figure 6.2), this form lead to the NLZD4/4 achieving a slightly higher order of accuracy – indicated by a slope increase – in addition to lower "intercepts". This suggests that the extent of the accuracy increase offered by the NLZD4/4 is dependent on a function's dynamics, as well as its form.

The NLZD4/4 has the opposite effect on Equinoctial Elements integration. Compared to the RK4, the NLZD4/4 "intercept" is initially higher, suggesting lower accuracy. However, the NLZD4/4 slope is higher than the RK4. For instance, the intersection at 10^4 steps shows the NLZD4/4 achieving higher position accuracy than the RK4.

7.2 SGP4

Figure 7.3 shows position error as a function of time using SGP4. The start and end times of a set of sample points used to generate TLEs, referred to as fit lengths, are indicated by color. A "0 day" fit refers to a TLE generated from a single state vector.

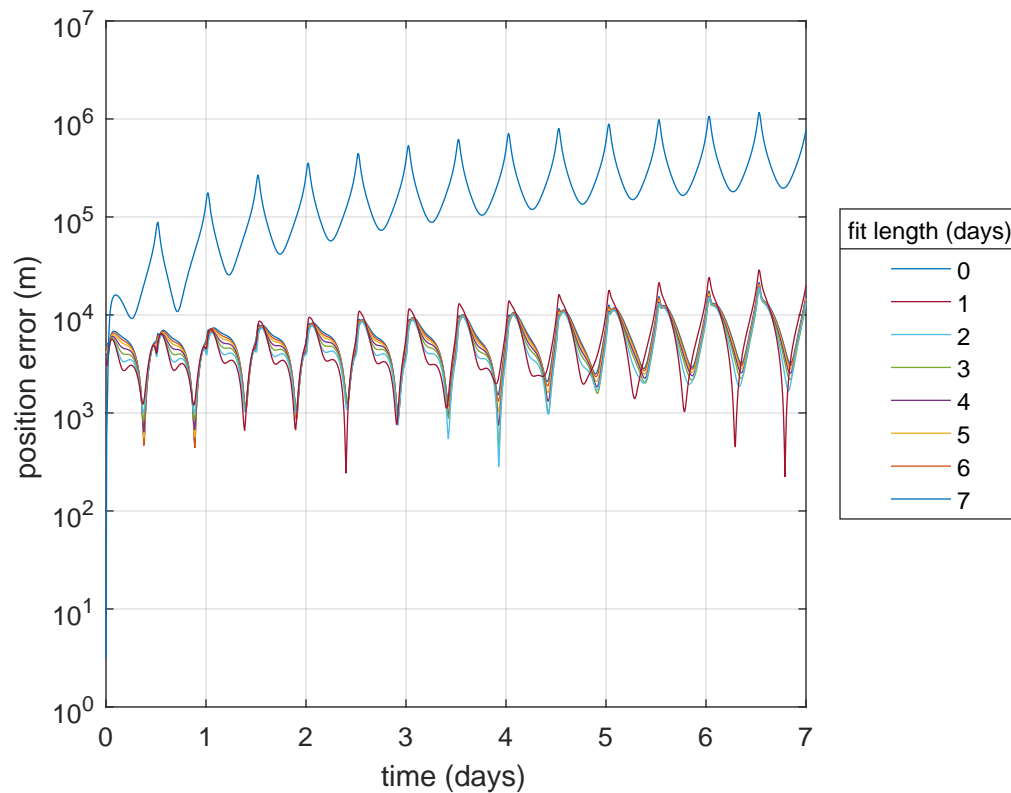


Fig. 7.3: Molniya position error as a function of time for different TLE fit lengths. A "0 day" fit refers to a TLE generated from a single state vector.

Figure 7.3 shows that low order modeling of Molniya orbit perturbations by SGP4 inherently leads to position error regardless of fit length. The TLE generated from a single state vector yields the highest position error. Excluding the single point fit, the fit length has a marginal impact on position accuracy. This indicates that using more ephemeris data to generate a TLE does not ensure higher accuracy for future propagation. Of course, a minimum amount of ephemeris data is required for reasonable position accuracy. Figure

7.3 shows that for Molniya orbit propagation, fitting over 1 day (2 orbits) is adequate.

Position error shown in Figure 7.3 is relative to the truth ephemeris generated for this particular Molniya orbit model. While the environment model captures dominant perturbations, it is not comprehensive. Position errors with respect to a higher order truth model may not match the results shown in Figure 7.3.

7.3 Accuracy Comparison

Figure 7.4 shows position error after 7 days as a function of number of integration steps. The format and styling of this plot is identical to Figure 7.2, except for an additional line indicating the lowest SGP4 position error from the fit lengths analyzed and displayed in Figure 7.3. This comparison shows how many integration steps are needed to match SGP4 position accuracy for this Molniya orbit model. Tables 7.1 and 7.2 list the number of integration steps where the position errors of each differential equation formulation and SGP4 intersect.

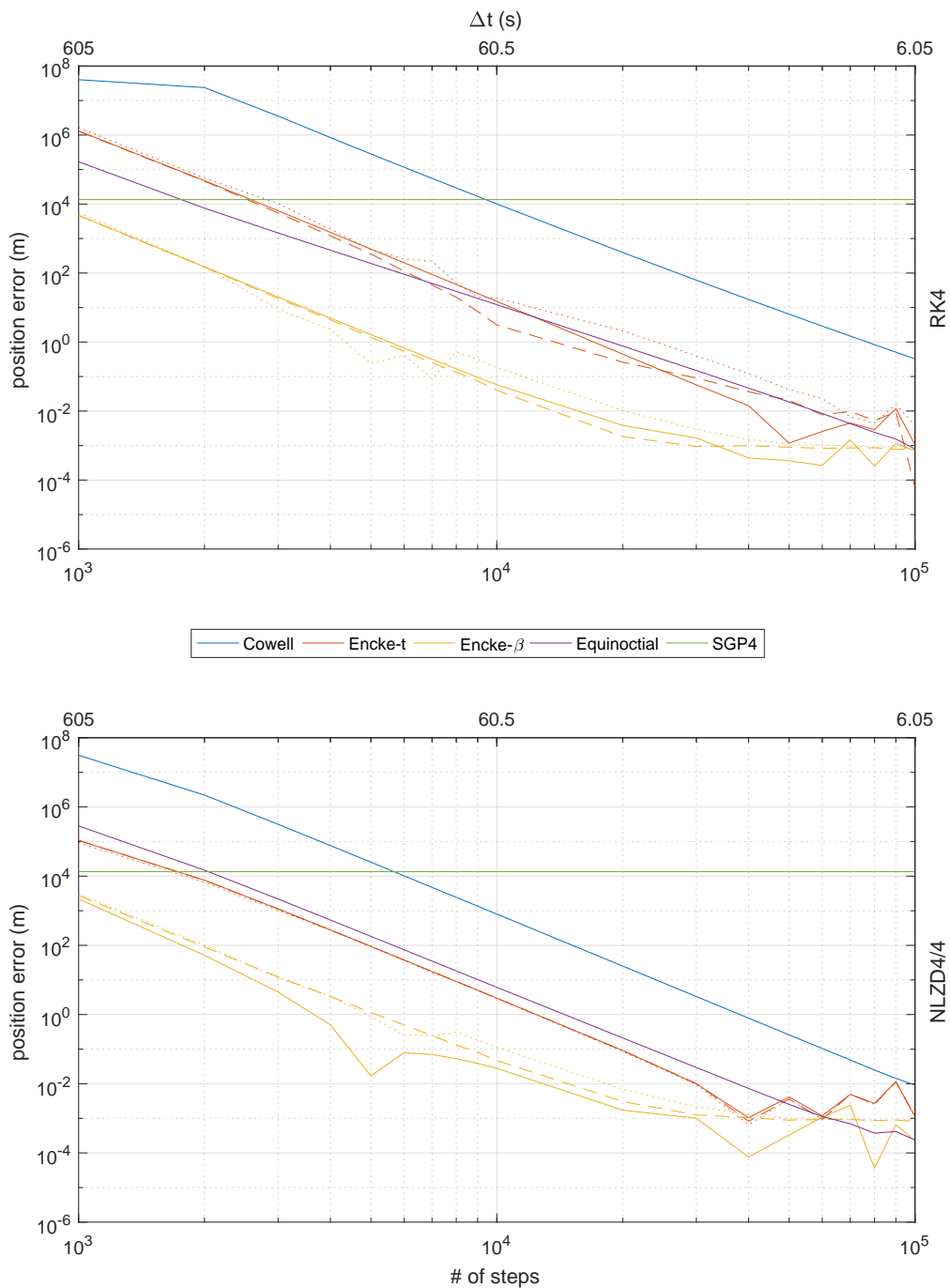


Fig. 7.4: Comparison of 7 day Molniya position error between numerical propagators and SGP4. Line textures for Encke formulations indicate the following rectification tolerances: solid = 0% (every step), dashed = 0.01%, dotted = 0.1%. The upper plot shows RK4 results and the lower plot shows NLZD4/4 results.

Table 7.1: Number of integration steps and corresponding time step (if available) required by each differential equation formulation with the RK4 to match the 7 day Molniya position accuracy of SGP4.

Formulation	# of Steps	Time Step (s)
Cowell	9.5×10^3	63.7
Encke-time (0%)	2.6×10^3	232.6
Encke-time (0.01%)	2.6×10^3	232.6
Encke-time (0.1%)	2.8×10^3	216.0
Encke-beta (0%)	$< 1 \times 10^3$	N/A
Encke-beta (0.01%)	$< 1 \times 10^3$	N/A
Encke-beta (0.1%)	$< 1 \times 10^3$	N/A
Equinoctial Elements	1.8×10^3	336.0

Table 7.2: Number of integration steps and corresponding time step (if available) required by each differential equation formulation with the NLZD4/4 to match the 7 day Molniya position accuracy of SGP4.

Formulation	# of Steps	Time Step (s)
Cowell	5.8×10^3	104.3
Encke-time (0%)	1.8×10^3	336.0
Encke-time (0.01%)	1.8×10^3	336.0
Encke-time (0.1%)	1.8×10^3	336.0
Encke-beta (0%)	$< 1 \times 10^3$	N/A
Encke-beta (0.01%)	$< 1 \times 10^3$	N/A
Encke-beta (0.1%)	$< 1 \times 10^3$	N/A
Equinoctial Elements	2×10^3	302.4

7.4 Timing Comparison

Table 7.3 lists the time required for each numerical propagator to complete one integration step normalized to the runtime of SGP4 for this Molniya orbit model. The time per integration step is dominated by the perturbing acceleration calculation, which is dictated by the environment model. Changing the perturbations or formulations within the environment model could significantly alter these timing results.

Table 7.3: Time required for one integration step normalized to SGP4 runtime for Molniya.

Propagator	Time
SGP4	1
Cowell, RK4	0.0800
Cowell, NLZD4/4	0.0800
Encke-time, RK4	0.0832
Encke-time, NLZD4/4	0.0832
Encke-beta, RK4	0.0821
Encke-beta, NLZD4/4	0.0821
Equinoctial Elements, RK4	0.0832
Equinoctial Elements, NLZD4/4	0.0832

Forming the differential equations using Cowell requires the fewest calculations, so naturally it takes the least amount of time. The RK4 and NLZD4/4 timing is consistent across all formulations.

Table 7.3 shows that for any numerical propagation method, about 12 full integration steps can be taken before exceeding the runtime of SGP4. Comparing with Table 5.3 demonstrates the dependency of computation time on the environment model. Comparing with Table 6.3 shows the timing difference between a 4×4 and 8×8 gravity model, as the SGP4 runtime is comparable for GEO and Molniya orbits, and the only difference between GEO and Molniya environment models is the gravity model.

CHAPTER 8
GTO RESULTS

8.1 Numerical Propagation

Figures 8.1 and 8.2 show comparisons between differential equation formulations, numerical integration schemes, and number of integration steps (step size). For this GTO model, the initial state is listed in Table 4.1, and the environment model is listed in Table 4.3. The step size used for propagating the truth ephemeris is listed in Table 4.2.

Figure 8.1 shows position error as a function of time for each differential equation formulation. Position error is calculated using equation (4.1). Differential equation formulations are indicated by color. For Encke-time and Encke-beta, solid lines indicate rectification at every step, dashed lines indicate a 0.01% rectification tolerance, and dotted lines indicate a 0.1% rectification tolerance. The plots in the left column show results using the RK4. The plots in the right column show results using the NLZD4/4. The plots in the upper row show results using 10^4 integration steps over the 7 day propagation period, which corresponds to a time step of 60.48 s. The plots in the lower row show results using 10^3 integration steps, which corresponds to a time step of 604.8 s.

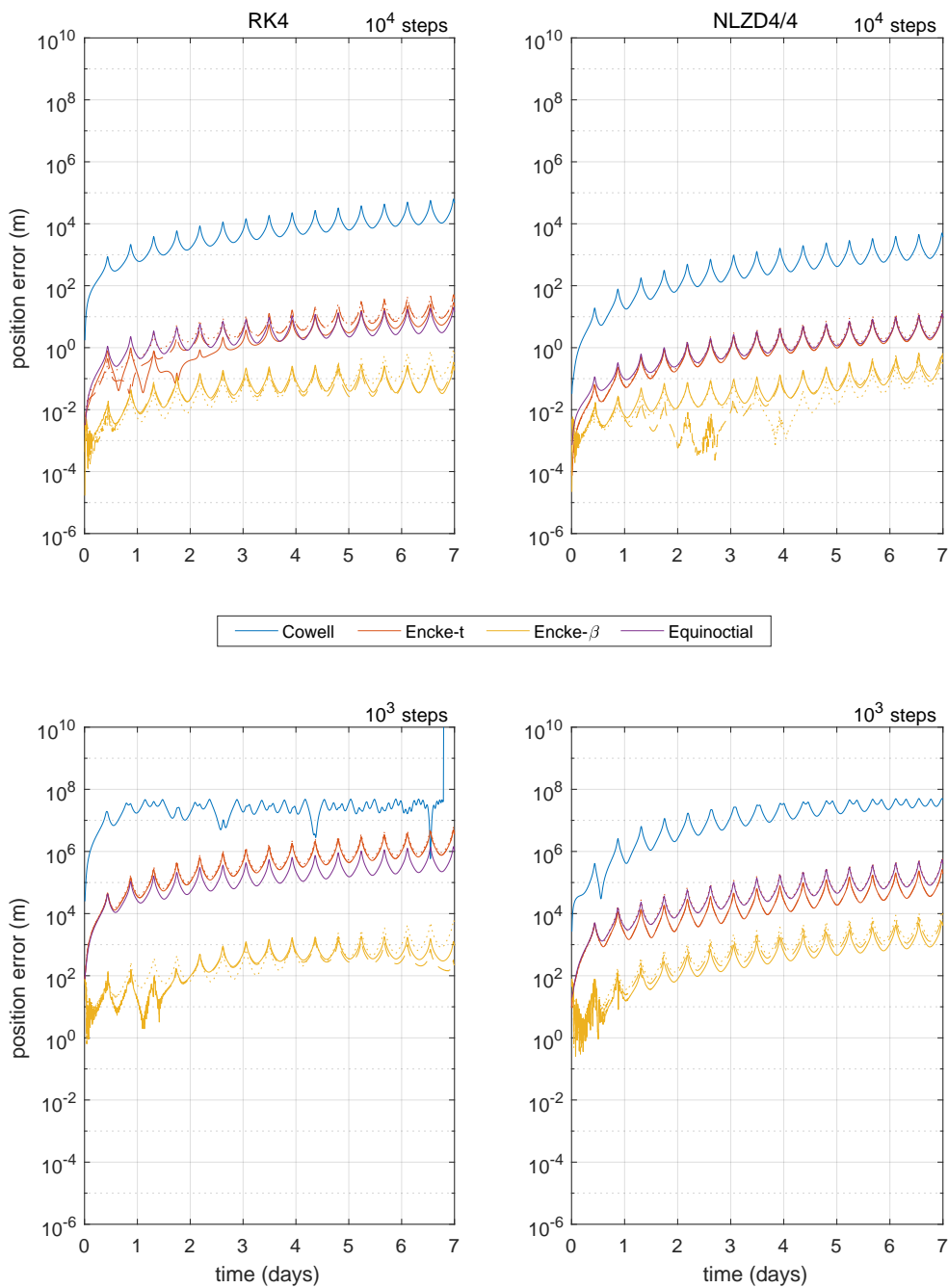


Fig. 8.1: GTO position error as a function of time for each differential equation formulation. Line textures for Encke formulations indicate the following rectification tolerances: solid = 0% (every step), dashed = 0.01%, dotted = 0.1%. The left column shows RK4 results and the right column shows NLZD4/4 results. The upper row shows results using 10^4 integration step the lower row shows results using 10^3 integration step.

Figure 8.1 shows that for this GTO model, the formulation consistently providing the highest position accuracy for 10^4 and 10^3 integration steps over 7 days ($\Delta t = 60.48$ s and $\Delta t = 604.8$ s) is Encke-beta rectified every step. Encke-beta provides significantly more accuracy than all other formulations because the time-regularized distribution of integration steps replaces unnecessary steps around apogee with additional steps around perigee (see Section 2.2.2). In contrast to the orbits previously discussed, the NLZD4/4 does not consistently provide higher accuracy than the RK4 for Encke-beta. Cowell and Encke-time do show an accuracy increase with the NLZD4/4. Equinoctial Elements shows a marginal accuracy increase, but it also varies with the number of integration steps and at which time the position error is analyzed.

Position error generally grows with time. Swoops in the position error occur at a period equal to the orbital period (≈ 2 per day). These swoops are the result of integration step distribution, integration error direction, and elliptical orbital motion. For a more detailed explanation, see Appendix C (although the examples pertain to Molniya orbits, the effects in GTO are similar).

Figure 8.2 shows position error after 7 days as a function of number of integration steps. The number of integration steps spans two decades with samples taken at each minor tick mark. A corresponding time step is also listed. It is rounded simply to keep a cleaner appearance. The color schemes and line textures used in Figure 8.2 are the same as Figure 8.1. The upper plot shows results using the RK4. The lower plot shows results using the NLZD4/4.

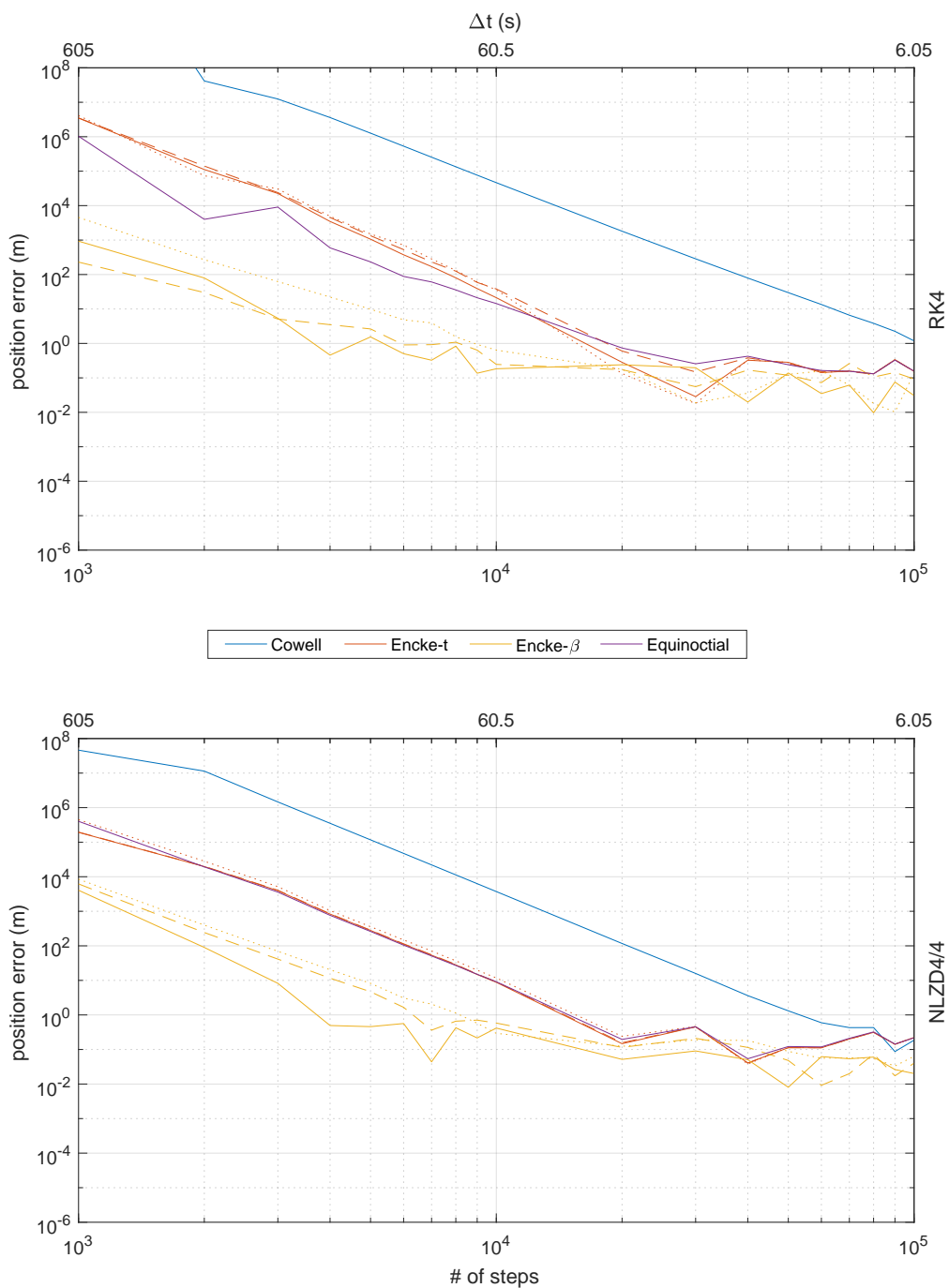


Fig. 8.2: 7 day GTO position error as a function of number of integration steps for each differential equation formulation. Line textures for Encke formulations indicate the following rectification tolerances: solid = 0% (every step), dashed = 0.01%, dotted = 0.1%. The upper plot shows RK4 results and the lower plot shows NLZD4/4 results.

Figure 8.2 confirms that for this GTO model, the formulation consistently providing the highest position accuracy is Encke-beta rectified every step. It also confirms that Encke-beta for every rectification tolerance provides significantly more position accuracy than all other formulations regardless of integrator. The NLZD4/4 provides higher position accuracy than the RK4 for Encke-time and Cowell. Overall Equinoctial Elements shows a marginal accuracy increase with the NLZD4/4, but this does not apply to all step sizes. Neither integrator shows a clear advantage for Encke-beta.

Plateaus in position error indicate a region where further reductions in step size yield no reliable accuracy increase. For Encke-beta, this plateau occurs around 10^4 integration steps, which corresponds to a time step of about 1 min. While the location of this plateau is dependent on final propagation time, Figure 8.2 shows how a minimum step size can be determined for any numerical propagator.

The position error lines in Figure 8.2 are more unsteady than other orbits. They also plateau at least an order of magnitude higher. This is likely caused by the GTO period and perturbing function. Figure 8.1 shows that the final position vector is near perigee, corresponding to a position error peak. However, the Molniya orbit also has a period where the final position vector is near perigee. The difference between Molniya and GTO scenarios is the strength of the perturbing acceleration. The minimum GTO altitude is ≈ 250 km, whereas the minimum Molniya altitude is ≈ 1500 km. Stronger gravitational perturbations and the addition of drag contribute to higher variation in the final position. Altogether, this results in unsteady position error lines that plateau earlier than other orbits.

Molniya and GTO results exhibit the same general trends. The most important trend is Encke-beta, regardless of rectification tolerance or integrator, provides an accuracy increase by orders of magnitude over other formulations. The NLZD4/4 provides a consistent accuracy increase over the RK4 for Cowell and Encke-time. For Equinoctial Elements and Encke-beta, however, the NLZD4/4 fails to provide a consistent improvement. This is especially interesting considering that these formulations are completely different. More research is needed to better understand the limitations of the NLZD4/4.

8.2 SGP4

Figure 8.3 shows position error as a function of time using the SGP4. The start and end times of a set of sample points used to generate TLEs, referred to as fit lengths, are indicated by color. A "0 day" fit refers to a TLE generated from a single state vector.

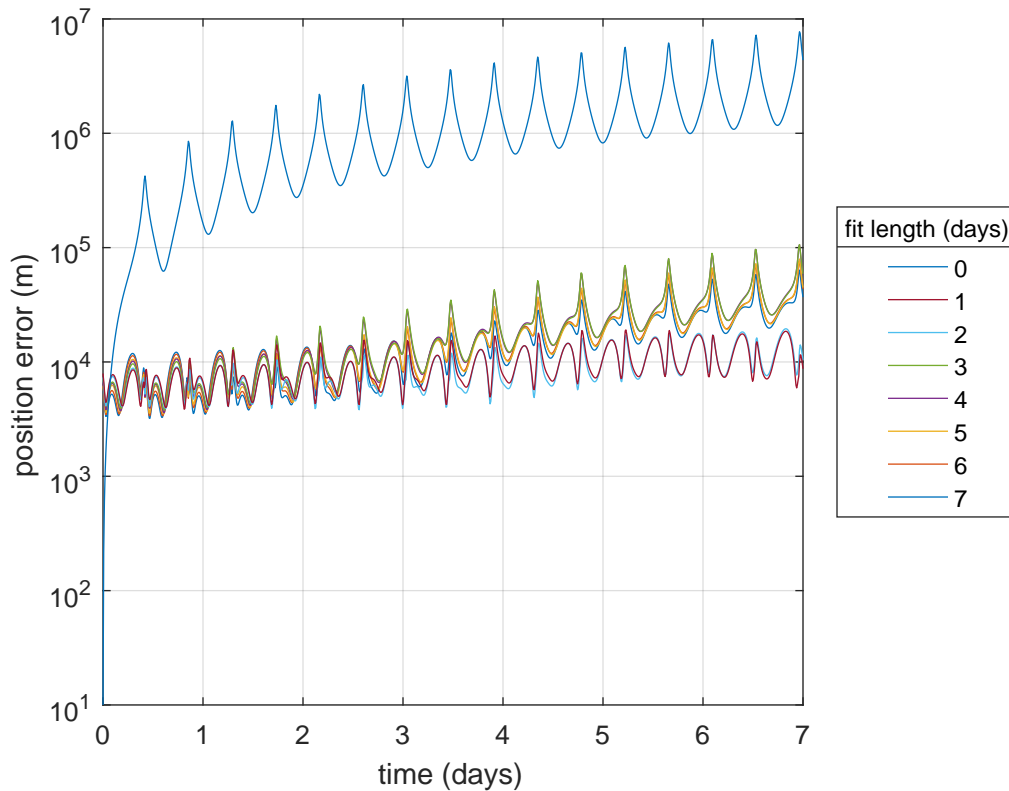


Fig. 8.3: GTO position error as a function of time for different TLE fit lengths. A "0 day" fit refers to a TLE generated from a single state vector.

Figure 8.3 shows that low order modeling of GTO perturbations by SGP4 inherently leads to position error regardless of fit length. The TLE generated from a single state vector yields the highest position error. Fits over 1 and 2 days yield the highest position accuracy, almost an order of magnitude higher than fits with additional data. This indicates that using more ephemeris data to generate a TLE does not ensure higher accuracy for future propagation. In this case, a fit over multiple days accounts for old data that does not

accurately describe the current orbit. Since future orbits will more likely resemble the current orbit as opposed to previous orbits, old data introduces bias to the fit. Of course, there is a balance between selecting only the most recent data and having enough data for a proper fit. Figure 8.3 shows that for GTO propagation, fitting over 1 day (≈ 2 orbits) is adequate.

Position error shown in Figure 8.3 is relative to the truth ephemeris generated for this particular GTO model. While the environment model captures dominant perturbations, it is not comprehensive. Position errors with respect to a higher order truth model may not match the results shown in Figure 8.3.

8.3 Accuracy Comparison

Figure 8.4 shows position error after 7 days as a function of number of integration steps. The format and styling of this plot is identical to Figure 8.2, except for an additional line indicating the lowest SGP4 position error from the fit lengths analyzed and displayed in Figure 8.3. This comparison shows how many integration steps are needed to match the SGP4 position accuracy for this GTO model. Tables 8.1 and 8.2 list the number of integration steps where the position errors of each differential equation formulation and SGP4 intersect.

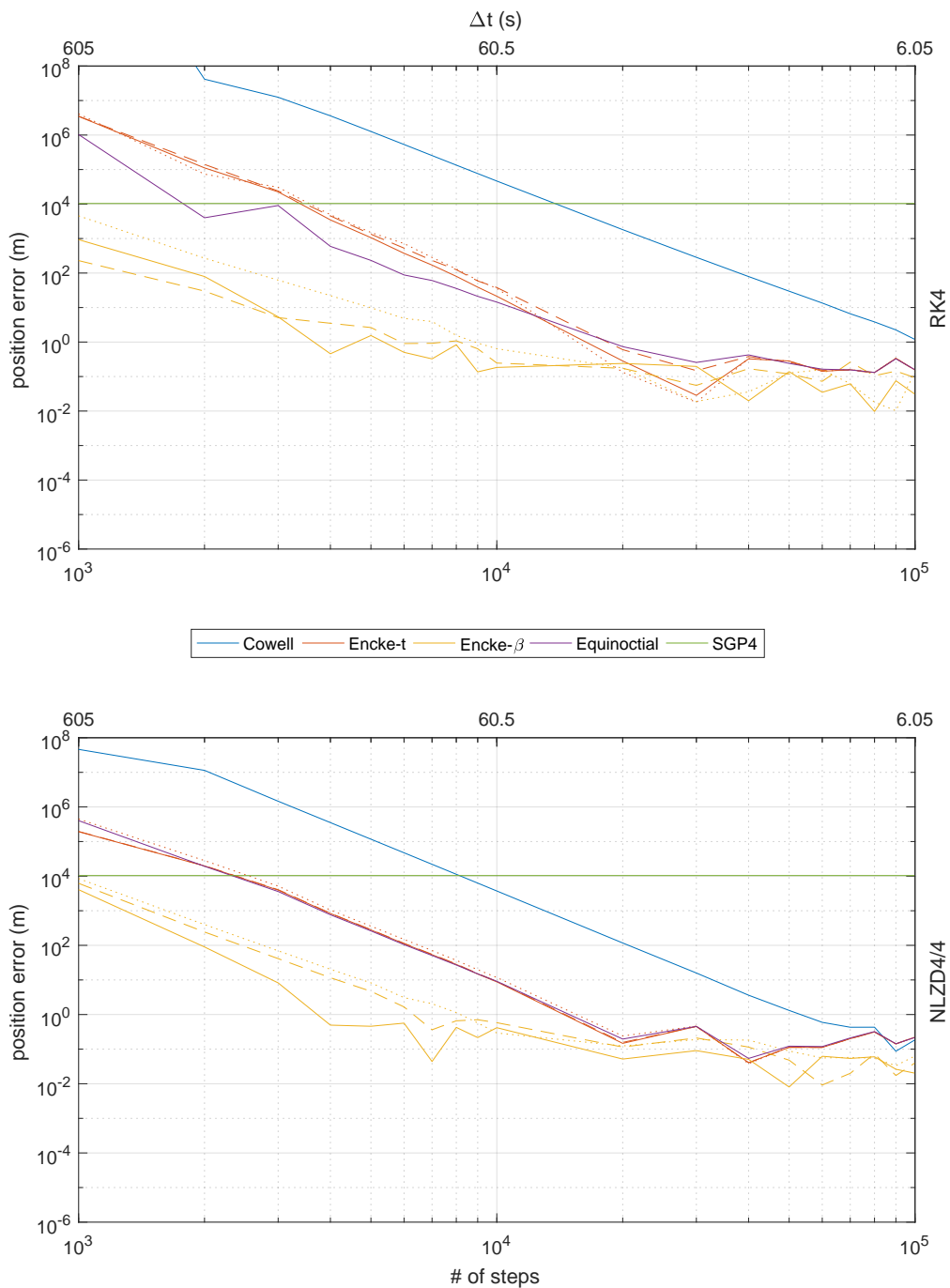


Fig. 8.4: Comparison of 7 day GTO position error between numerical propagators and SGP4. Line textures for Encke formulations indicate the following rectification tolerances: solid = 0% (every step), dashed = 0.01%, dotted = 0.1%. The upper plot shows RK4 results and the lower plot shows NLZD4/4 results.

Table 8.1: Number of integration steps and corresponding time step (if available) required by each differential equation formulation with the RK4 to match the 7 day GTO position accuracy of SGP4.

Formulation	# of Steps	Time Step (s)
Cowell	1.5×10^4	40.3
Encke-time (0%)	3.5×10^3	172.8
Encke-time (0.01%)	3.5×10^3	172.8
Encke-time (0.1%)	3.5×10^3	172.8
Encke-beta (0%)	$< 1 \times 10^3$	N/A
Encke-beta (0.01%)	$< 1 \times 10^3$	N/A
Encke-beta (0.1%)	$< 1 \times 10^3$	N/A
Equinoctial Elements	1.8×10^3	336.0

Table 8.2: Number of integration steps and corresponding time step (if available) required by each differential equation formulation with the NLZD4/4 to match the 7 day GTO position accuracy of SGP4.

Formulation	# of Steps	Time Step (s)
Cowell	8×10^3	75.6
Encke-time (0%)	2.4×10^3	252.0
Encke-time (0.01%)	2.4×10^3	252.0
Encke-time (0.1%)	2.5×10^3	241.9
Encke-beta (0%)	$< 1 \times 10^3$	N/A
Encke-beta (0.01%)	$< 1 \times 10^3$	N/A
Encke-beta (0.1%)	$< 1 \times 10^3$	N/A
Equinoctial Elements	2.4×10^3	252.0

8.4 Timing Comparison

Table 8.3 lists the time required for each numerical propagator to complete one integration step normalized to the runtime of SGP4 for this GTO model. The time per integration step is dominated by the perturbing acceleration calculation, which is dictated by the environment model. Changing the perturbations or formulations within the environment model could significantly alter these timing results.

Table 8.3: Time required for one integration step normalized to SGP4 runtime for GTO.

Propagator	Time
SGP4	1
Cowell, RK4	0.0894
Cowell, NLZD4/4	0.0894
Encke-time, RK4	0.0941
Encke-time, NLZD4/4	0.0941
Encke-beta, RK4	0.0941
Encke-beta, NLZD4/4	0.0941
Equinoctial Elements, RK4	0.0941
Equinoctial Elements, NLZD4/4	0.0941

Forming the differential equations using Cowell requires the fewest calculations, so naturally it takes the least amount of time. The RK4 and NLZD4/4 timing is consistent across all formulations.

Table 8.3 shows that for any numerical propagation method, about 11 full integration steps can be taken before exceeding the runtime of SGP4. Comparing with Table 5.3 demonstrates the dependency of computation time on the environment model. Comparing with Table 7.3 shows the additional time required for drag calculations, as the SGP4 runtime is comparable for Molniya and GTO, and the only difference between Molniya and GTO environment models is drag.

CHAPTER 9
MMS RESULTS

9.1 Numerical Propagation

Figures 9.1 and 9.2 show comparisons between differential equation formulations, numerical integration schemes, and number of integration steps (step size). For this MMS orbit model, the initial state is listed in Table 4.1, and the environment model is listed in Table 4.3. The step size used for propagating the truth ephemeris is listed in Table 4.2.

Figure 9.1 shows position error as a function of time for each differential equation formulation. Position error is calculated using equation (4.1). Differential equation formulations are indicated by color. For Encke-time and Encke-beta, solid lines indicate rectification at every step, dashed lines indicate a 0.01% rectification tolerance, and dotted lines indicate a 0.1% rectification tolerance. The plots in the left column show results using the RK4. The plots in the right column show results using the NLZD4/4. The plots in the upper row show results using 10^4 integration steps over the 7 day propagation period, which corresponds to a time step of 60.48 s. The plots in the lower row show results using 10^3 integration steps, which corresponds to a time step of 604.8 s.

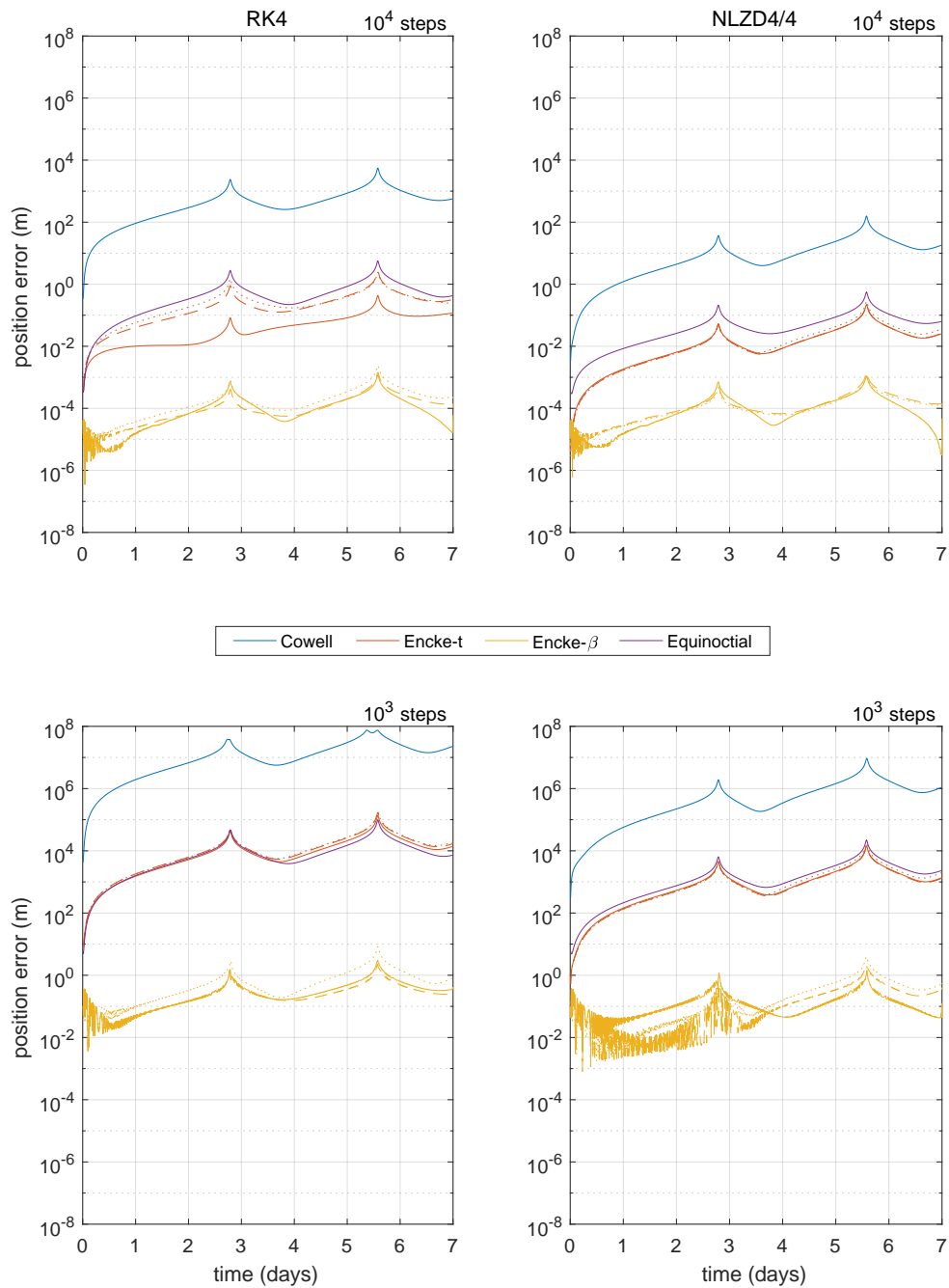


Fig. 9.1: MMS position error as a function of time for each differential equation formulation. Line textures for Encke formulations indicate the following rectification tolerances: solid = 0% (every step), dashed = 0.01%, dotted = 0.1%. The left column shows RK4 results and the right column shows NLZD4/4 results. The upper row shows results using 10^4 integration steps and the lower row shows results using 10^3 integration steps.

Figure 9.1 shows that for this MMS orbit model, the formulation consistently providing the highest position accuracy for 10^4 and 10^3 integration steps over 7 days ($\Delta t = 60.48$ s and $\Delta t = 604.8$ s) is Encke-beta rectified every step. Encke-beta provides significantly more accuracy than all other formulations because the time-regularized distribution of integration steps replaces unnecessary steps around apogee with additional steps around perigee (see Section 2.2.2). The NLZD4/4 consistently provides higher position accuracy than the RK4 for all formulations excluding Encke-beta.

Position error generally grows with time. The two peaks indicate perigee passage, as the orbital period is just under 3 days. These peaks are the result of integration step distribution, integration error direction, and elliptical orbital motion. For a more detailed explanation, see Appendix C (although the examples pertain to Molniya orbits, the effects on this MMS orbit are similar).

Figure 9.2 shows position error after 7 days as a function of number of integration steps. The number of integration steps spans two decades with samples taken at each minor tick mark. A corresponding time step is also listed. It is rounded simply to keep a cleaner appearance. The color schemes and line textures used in Figure 9.2 are the same as Figure 9.1. The upper plot shows results using the RK4. The lower plot shows results using the NLZD4/4.

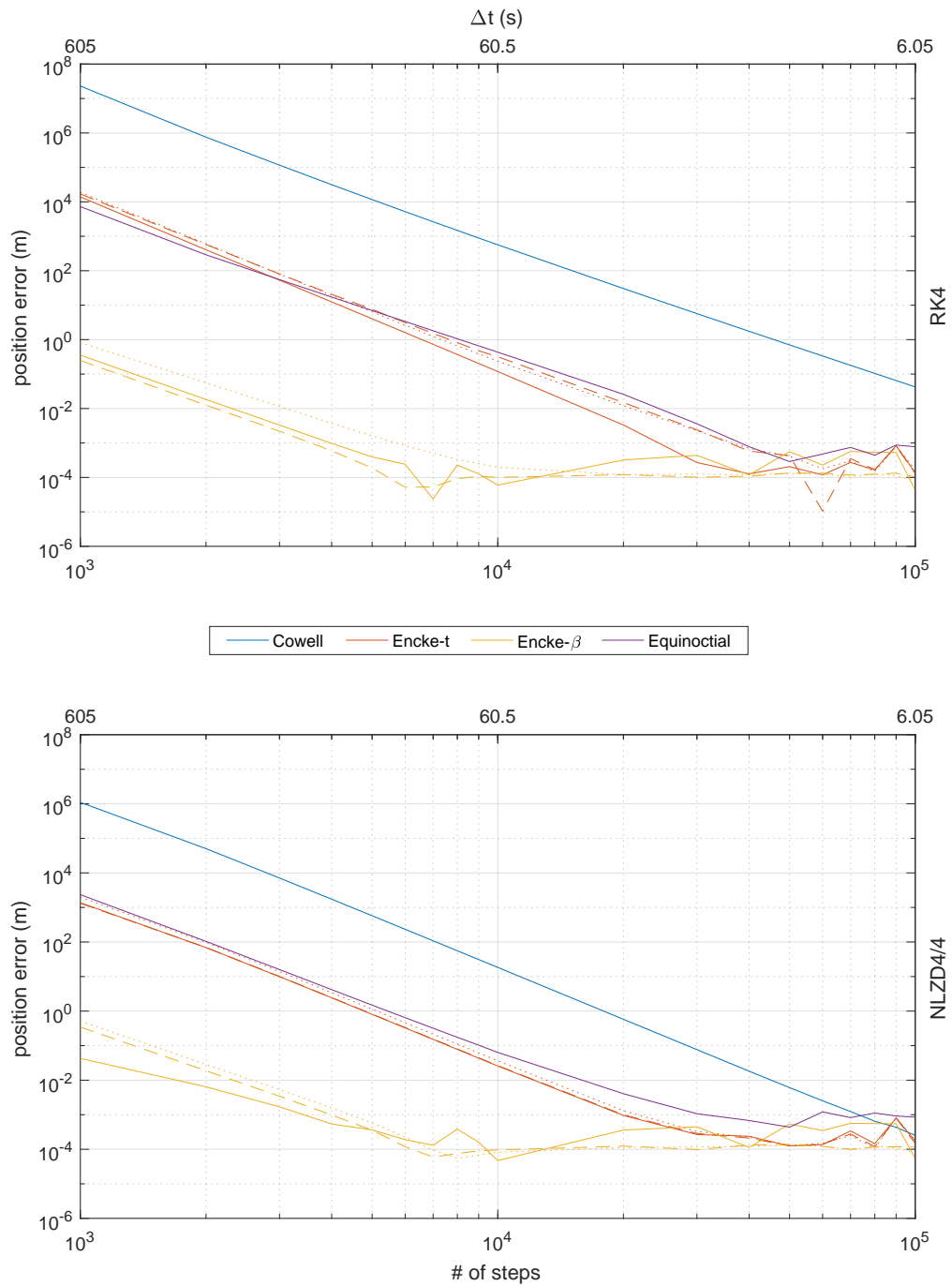


Fig. 9.2: 7 day MMS position error as a function of number of integration steps for each differential equation formulation. Line textures for Encke formulations indicate the following rectification tolerances: solid = 0% (every step), dashed = 0.01%, dotted = 0.1%. The upper plot shows RK4 results and the lower plot shows NLZD4/4 results.

Figure 9.2 confirms that for this MMS orbit model, the formulation consistently providing the highest position accuracy is Encke-beta rectified every step. It also confirms that Encke-beta for every rectification tolerance provides significantly more position accuracy than all other formulations regardless of integrator. The NLZD4/4 provides higher position accuracy than the RK4 for Encke-time, Equinoctial Elements, and Cowell. Overall Encke-beta shows a marginal accuracy increase with the NLZD4/4, but this does not apply to all step sizes.

Plateaus in position error indicate a region where further reductions in step size yield no reliable accuracy increase. For Encke-beta, this plateau occurs around 6×10^3 integration steps, which corresponds to a time step of about 100 sec. While the location of this plateau is dependent on final propagation time, Figure 9.2 shows how a minimum step size can be determined for any numerical propagator.

9.2 SGP4

Figure 9.3 shows MMS position error as a function of time using SGP4. The start and end times of a set of sample points used to generate TLEs, referred to as fit lengths, are indicated by color. A "0 day" fit refers to a TLE generated from a single state vector.

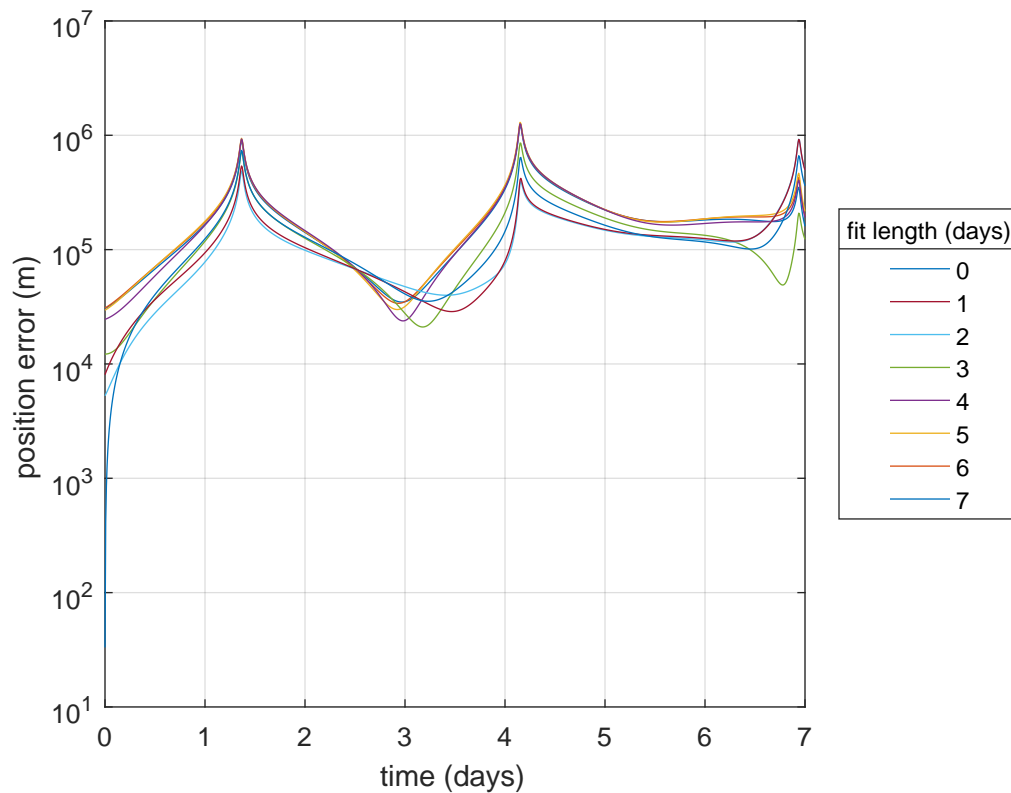


Fig. 9.3: MMS position error as a function of time for different TLE fit lengths. A "0 day" fit refers to a TLE generated from a single state vector.

Figure 9.3 shows that low order modeling of MMS orbit perturbations by SGP4 inherently leads to position error regardless of fit length. Of course, SGP4 was never designed for an orbit like MMS. The fit length has a marginal impact on position accuracy. Unlike every other orbit, the single point fit performs about as well as every other fit.

9.3 Accuracy Comparison

Figure 9.4 shows position error after 7 days as a function of number of integration steps. The format and styling of this plot is identical to Figure 9.2, except for an additional line indicating the lowest SGP4 position error from the fit lengths analyzed and displayed in Figure 9.3. Also, another decade of integration steps is added to more clearly see the intersection of numerical propagator and SGP4 results. This comparison shows how many integration steps are needed to match SGP4 position accuracy for this MMS orbit model. Tables 9.1 and 9.2 list the number of integration steps where the position errors of each differential equation formulation and SGP4 intersect.

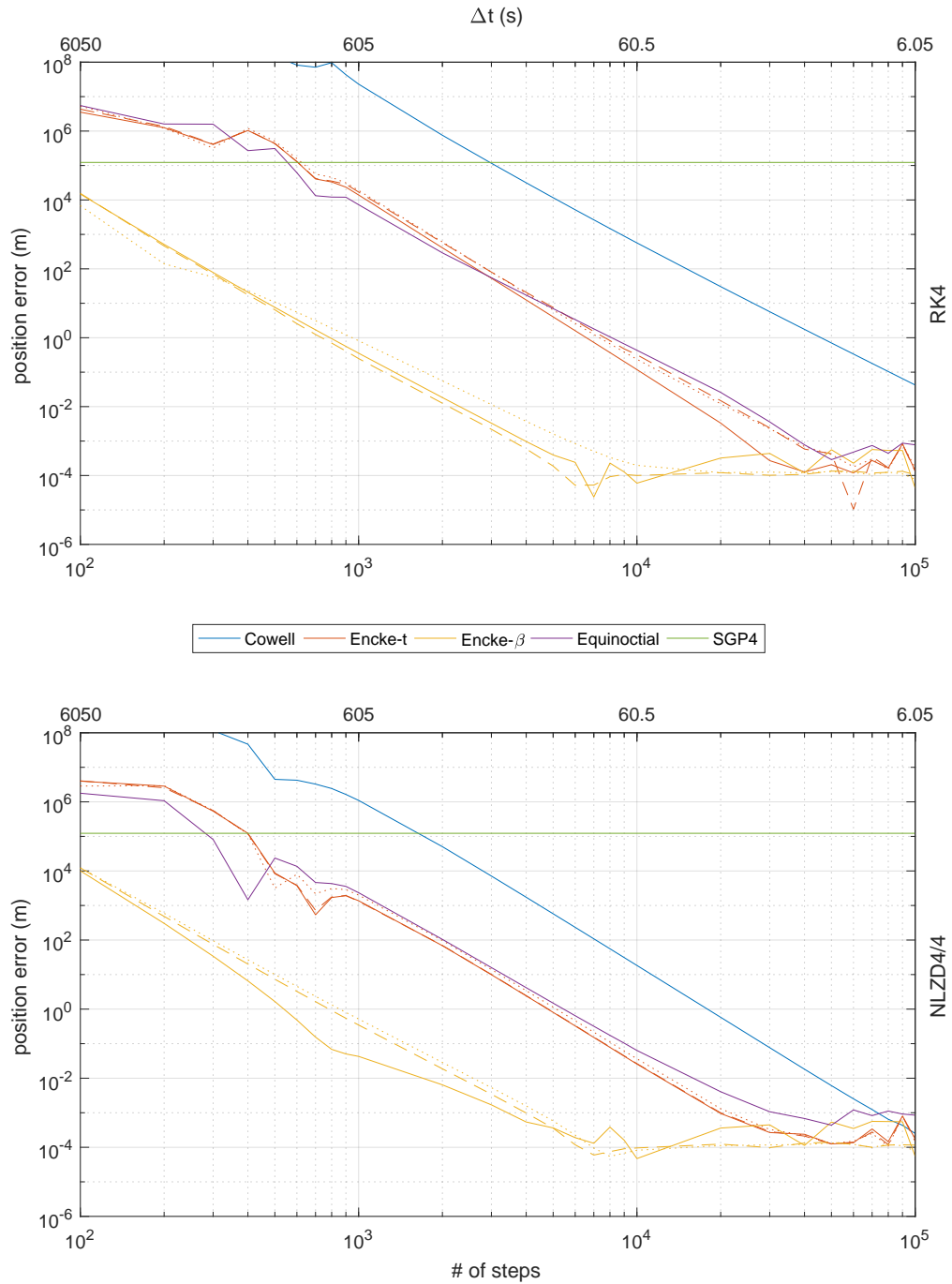


Fig. 9.4: Comparison of 7 day MMS position error between numerical propagators and SGP4. Line textures for Encke formulations indicate the following rectification tolerances: solid = 0% (every step), dashed = 0.01%, dotted = 0.1%. The upper plot shows RK4 results and the lower plot shows NLZD4/4 results.

Table 9.1: Number of integration steps and corresponding time step (if available) required by each differential equation formulation with the RK4 to match the 7 day MMS position accuracy of SGP4.

Formulation	# of Steps	Time Step (s)
Cowell	3×10^3	201.6
Encke-time (0%)	6.2×10^2	975.5
Encke-time (0.01%)	6.2×10^2	975.5
Encke-time (0.1%)	6.2×10^2	975.5
Encke-beta (0%)	$< 1 \times 10^2$	N/A
Encke-beta (0.01%)	$< 1 \times 10^2$	N/A
Encke-beta (0.1%)	$< 1 \times 10^2$	N/A
Equinoctial Elements	5.6×10^2	1080.0

Table 9.2: Number of integration steps and corresponding time step (if available) required by each differential equation formulation with the NLZD4/4 to match the 7 day MMS position accuracy of SGP4.

Formulation	# of Steps	Time Step (s)
Cowell	1.7×10^3	355.8
Encke-time (0%)	4×10^2	1512.0
Encke-time (0.01%)	4×10^2	1512.0
Encke-time (0.1%)	4×10^2	1512.0
Encke-beta (0%)	$< 1 \times 10^2$	N/A
Encke-beta (0.01%)	$< 1 \times 10^2$	N/A
Encke-beta (0.1%)	$< 1 \times 10^2$	N/A
Equinoctial Elements	2.9×10^2	2085.5

9.4 Timing Comparison

Table 9.3 lists the time required for each numerical propagator to complete one integration step normalized to the runtime of SGP4 for this MMS orbit model. The time per integration step is dominated by the perturbing acceleration calculation, which is dictated by the environment model. Changing the perturbations or formulations within the environment model could significantly alter these timing results.

Table 9.3: Time required for one integration step normalized to SGP4 runtime for MMS.

Propagator	Time
SGP4	1
Cowell, RK4	0.0894
Cowell, NLZD4/4	0.0894
Encke-time, RK4	0.0929
Encke-time, NLZD4/4	0.0929
Encke-beta, RK4	0.0918
Encke-beta, NLZD4/4	0.0918
Equinoctial Elements, RK4	0.0929
Equinoctial Elements, NLZD4/4	0.0929

Forming the differential equations using Cowell requires the fewest calculations, so naturally it takes the least amount of time. The RK4 and NLZD4/4 timing is consistent across all formulations.

Table 9.3 shows that for any numerical propagation method, about 11 full integration steps can be taken before exceeding the runtime of SGP4. Comparing with Table 5.3 demonstrates the dependency of computation time on the environment model. While MMS and Molynia have the same environment models, the time per step compared to Table 7.3 is slightly higher as fewer perturbing effects are modeled by SGP4 (see Table 3.1).

CHAPTER 10
PROPAGATOR COMPARISON

Figure 10.1 shows the computation time relative to SGP4 required by each numerical propagator as a function of position accuracy after 7 days. LEO, GEO, Molniya, and GTO results are shown. Differential equation formulations are indicated by color. Solid lines indicate RK4 integration, and dashed lines indicate NLZD4/4 integration. While Encke-time results are not plotted, its accuracy in LEO and GEO are nearly identical to Encke-beta. Encke-beta results are generated with a 0.01% rectification tolerance. The green star located on each x-axis indicates the highest position accuracy attained by one SGP4 run (of course, additional runs will yield no further accuracy increase). A green line is extended vertically to more easily see the intersection of this position accuracy with numerical propagation results. An intersection indicates how long it takes each numerical propagator, in terms of SGP4 runs, to match the best possible position accuracy of SGP4 after 7 days.

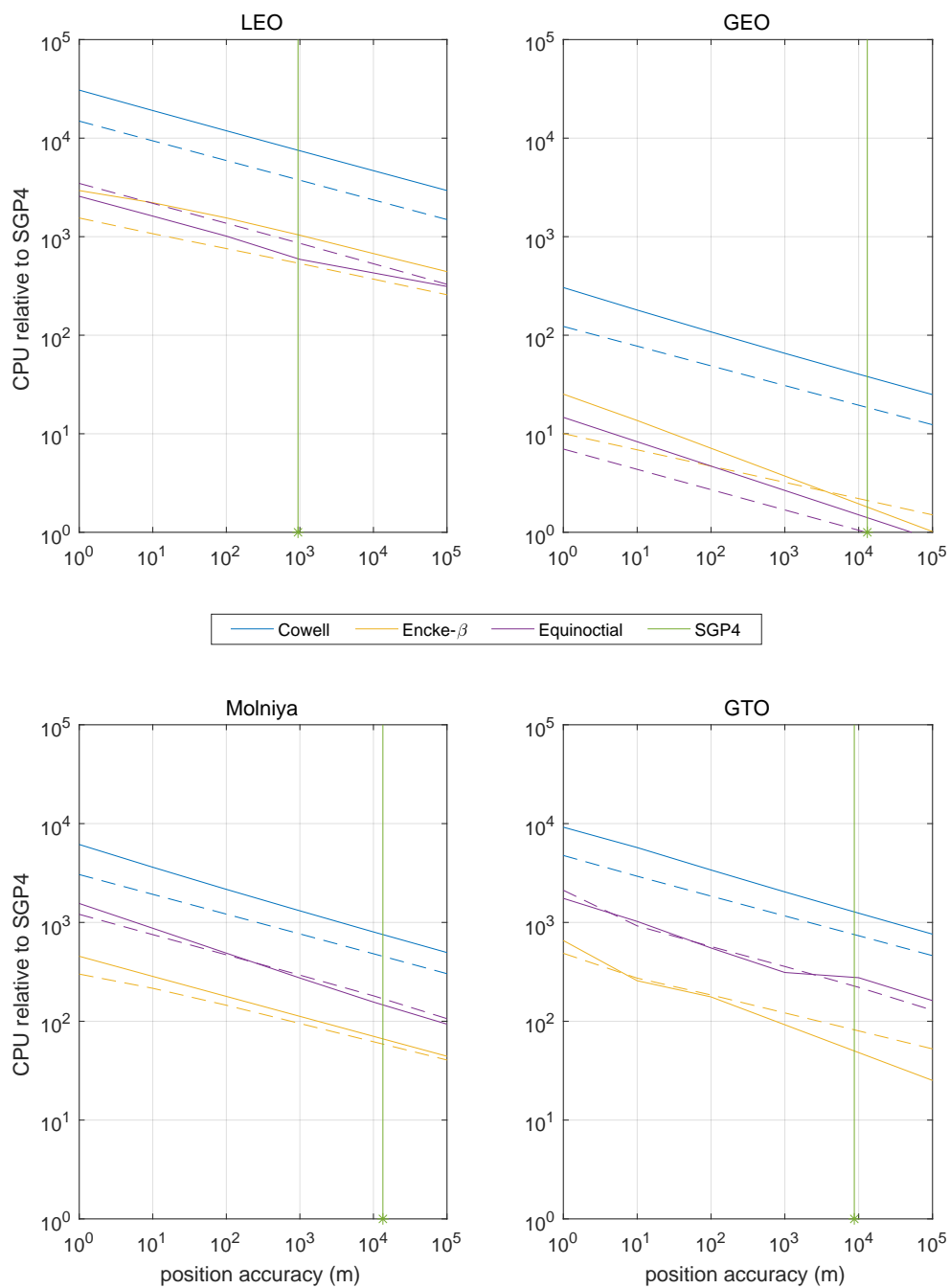


Fig. 10.1: Computation time relative to SGP4 required by each numerical propagator as a function of 7 day position accuracy. Solid lines indicate RK4 integration and dashed lines indicate NLZD4/4 integration. The green star located on each x-axis indicates the highest position accuracy attained by one SGP4 run.

Before discussing the results of Figure 10.1, it is important to address some assumptions. First, the SGP4 accuracy assumes a best case scenario in terms of TLE generation, where a sufficient amount of ephemeris data is available. Second, these results show 7 day propagation. Lowering the final propagation time will generally lower the position errors for all propagation methods. The extent of each accuracy increase, however, depends on orbit type and propagator. Figures 5.1, 6.1, 7.1, and 8.1 show how numerically propagated position error changes over time for select step sizes. Figures 5.3 , 6.3, 7.3, and 8.3 show how SGP4 position error changes over time. Third, the code for the environment model, which accounts for the majority of numerical propagation runtime, could be further optimized, which would lower the numerical propagation lines on each plot.

Figure 10.1 confirms the speed of SGP4. For instance, in LEO, it takes every numerical propagator over 500 times longer to achieve the same position accuracy. The best numerical propagators for Molniya and GTO take over 50 times longer. In GEO, however, propagating with Equinoctial Elements and the NLZD4/4 requires the time equivalent of one SGP4 run to match the best possible SGP4 accuracy. This indicates that GEO propagation should be performed numerically with Equinoctial Elements and the NLZD4/4. Any additional time allocated for numerical propagation increases position accuracy. For example, the time equivalent of 10 SGP4 runs with Equinoctial Elements and the NLZD4/4 yields position errors lower than 1 m.

CHAPTER 11

CONCLUSIONS AND FUTURE WORK

This survey and performance analysis compared the accuracy and computation requirements of orbit propagators for various orbits. Numerical propagators were analyzed by comparing differential equation formulations over a range of integration steps for a fixed environment model and integrator. SGP4 was analyzed by varying the amount of data used to generate TLE inputs. Ultimately, this research provided a quantitative understanding of the performance of common propagators over different orbit regimes.

For all orbits, Encke and Equinoctial Elements provided significantly higher position accuracy than Cowell regardless of integrator. In LEO, Equinoctial Elements was superior with the RK4, but Encke was superior with the NLZD4/4. In GEO, Equinoctial Elements was consistently superior. For elliptical orbits, Encke-beta provided an accuracy increase over Encke-time and Equinoctial Elements by orders of magnitude. These results indicate that the best all-purpose formulation for on-board propagation (i.e. fixed-step integration) is Encke-beta.

The NLZD4/4 generally provided higher position accuracy than the RK4, although the extent of this accuracy increase varied with orbit type and differential equation formulation. One notable exception was Equinoctial Elements in LEO where the NLZD4/4 performed consistently worse. For Encke-beta in GTO and Equinoctial Elements in Molniya and GTO, neither integrator provided a clear advantage. These results show that some functions can be better approximated with the RK4.

SGP4 provided the highest accuracy in LEO, where a TLE fit with an adequate number of sample points resulted in position error on the order of 1 km. The best TLE fits for GEO, Molniya, and GTO resulted in SGP4 position error on the order of 10 km. SGP4 is an attractive propagator option due to its speed. However, this analysis showed that its accuracy is dependent on the amount of previous ephemeris data used for TLE generation.

For an on-board application, a sufficient amount of data for accurate TLE fits might not be readily available.

In GEO, the speed of SGP4 is compromised by poor modeling of perturbation effects. Numerical propagation with Equinoctial Elements and the NLZD4/4 matches the best possible SGP4 position accuracy for the same computation time as SGP4. This means that the superior propagator for GEO consists of a numerical formulation with Equinoctial Elements and the NLZD4/4. Any additional computation time will allow for more integration steps and subsequently higher accuracy.

While the orbits, environment models, or time spans analyzed in this survey may not exactly align with a future mission, the approach used to generate results is directly applicable. These results can also serve as a starting point in narrowing down a propagator best suited for future applications.

This analysis limited the scope of numerical propagators by including only two numerical integrators. Future work might include higher order integrators such as a Runge-Kutta 8th order. It would be interesting to see where the current position errors and position errors from higher order integrators intersect.

Other future work could investigate the environment model more closely to determine, given a fixed computation time, what environment model formulation yields the highest absolute position accuracy. For example, approximations can be made in the transformation between inertial and Earth-fixed frames. Approximating this calculation could free up computation time for additional perturbations. However, the subsequent accuracy decrease from approximation may offset the accuracy gained from including higher order perturbations.

Future work that extends beyond orbit propagation might include a thorough analysis of the NLZD4/4. This research provided examples where the RK4 performs better. It would be useful to characterize, if possible, which functions are better suited for the traditional RK4.

REFERENCES

- [1] Vallado, D. A., *Fundamentals of Astrodynamics and Applications*, Microcosm Press, Hawthorne, CA., 2007.
- [2] Robinson, S., Scarritt, S., and Goodman, J. L., “Encke-beta Predictor for Orion Burn Targeting and Guidance,” *AAS Guidance and Control Conference*, Breckenridge, CO, February 5-10 2016. AAS 16-112.
- [3] Battin, R., *An Introduction to the Mathematics and Methods of Astrodynamics*, AIAA Education Series, Reston, Virginia, 1999.
- [4] Vallado, D. A., “An Analysis of State Vector Propagation Using Differing Flight Dynamics Programs,” *AAS/AIAA Astrodynamics Specialist Conference*, Copper Mountain, CO, January 23-27, 2005. AAS 05-199.
- [5] Pannekoek, A., *A History of Astronomy*, Dover Publications, New York, 1989.
- [6] Kozai, Y., “The Motion of a Close Earth Satellite,” *Astronomical Journal*, Vol. 64, 1959, pp. 367–377.
- [7] Kozai, Y., “Second-Order Solution of Artificial Satellite Theory Without Drag,” *Astronomical Journal*, Vol. 67, 1962, pp. 446.
- [8] Brouwer, D., “Solutions of the Problem of Artificial Satellite Theory Without Drag,” *Astronomical Journal*, Vol. 64, 1959, pp. 378–397.
- [9] Hoots, F. R. and Roehrich, R., “Models for Propagation of NORAD Element Sets. Spacetrack Report no. 3.” U.S. Air Force: Aerospace Defense Command. 1980.
- [10] Bond, V. R. and Allman, M. C., *Modern Astrodynamics, Fundamentals and Perturbations Methods*, University Press, Princeton, New Jersey, 1996.
- [11] Stiefel, E. L. and Scheifele, G., *Linear and Regular Celestial Mechanics- Perturbed Two-Body Motion, Numerical Methods, Canonical Theory*, Springer, New York, 1971.
- [12] Montenbruck, O. and Gill, E., *Satellite Orbits: Models, Methods, and Applications*, Springer, 2011.
- [13] Marsh, J. G., Lerch, F. J., Putney, B. H., Christodoulidis, D. C., Smith, D. E., Felsentreger, T. L., Sanchez, B. V., Klosko, S. M., Pavlis, E. C., Martin, T. V., Robbins, J. R., Williamson, R. G., Colombo, O. L., Rowlands, D. D., Eddy, W. F., Chandler, N. L., Rachlin, K. E., Patel, G. B., Bhati, S., and Chinn, D. S., “A New Gravitational Model for the Earth From Satellite Tracking Data: GEM-T1,” *Journal of Geophysical Research*, Vol. 93, No. B6, 1988, pp. 6169–6215.
- [14] Folkner, W. M., Williams, J. G., and Boggs, D. H., *The Planetary and Lunar Ephemeris DE421*, Jet Propulsion Laboratory Memorandum, IOM 343R-08-003.

- [15] *Systems Took Kit 11 Technical Notes*, Analytical Graphics Inc., 2016.
- [16] *U.S. Standard Atmosphere*, U.S. Government Printing Office, Washington, D.C., 1976.
- [17] Lear, W. M., *Nystrom Integrator*, Tech. Rep. JSC-24229, NASA - Lyndon B. Johnson Space Center, March 1990.
- [18] Hoots, F., Jr., P. W. S., and Glover, R. A., “A History of Analytical Orbit Modeling in the U. S. Space Surveillance System,” *Journal of Guidance, Control, and Dynamics*, Vol. 27, 2004, pp. 174–185.
- [19] Lane, M. H. and Cranford, K. H., “An Improved Analytical Drag Theory for the Artificial Satellite Problem,” *AIAA/AAS Astrodynamics Conference*, Princeton, NJ, August 20-22, 1969, AIAA 69-925.
- [20] Bowman, B., “A First Order Semi-Analytic Perturbation Theory for Highly Eccentric 12 Hour Resonating Satellite Orbits,” NORAD document, Nov. 1971.
- [21] Hujsak, R. S., “A Restricted Four Body Solution For Resonating Satellites Without Drag,” Project SPACETRACK Report no. 1, USAF Aerospace Defense Command, Nov. 1979.
- [22] Vallado, D. A., Crawford, P., Hujsak, R., and Kelso, T. S., “Revisiting Spacetrack Report no. 3,” *AAS/AIAA Astrodynamics Specialist Conference*, Keystone, CO, August 21-24, 2006. AIAA 2006-6753.
- [23] *Magnetospheric Multiscale: Using Earth’s magnetosphere as a laboratory to study the microphysics of magnetic reconnection*, NASA, March 12, 2015.
- [24] *An Overview of Reference Frames and Coordinate Systems in the SPICE Context*, Navigation and Ancillary Information Facility, 2017.
- [25] Seidelmann, P. K. and Urban, S. E., *Explanatory Supplement to the Astronomical Almanac*, U. S. Naval Observatory, University Science Books, Mill Valley, CA.
- [26] McCarthy, D. and Petit, G., *IERS Technical Note no. 3 - IERS Conventions*, U.S. Naval Observatory, 2003.
- [27] Vallado, D. A., Seago, J. H., and Seidelmann, P. K., “Implementation Issues Surrounding the New IAU Reference Systems for Astrodynamics,” *AAS/AIAA Space Flight Mechanics Conference*, Tampa, FL, January 22-26, 2006, AAS 06-134.

APPENDICES

Appendix A

Coordinate Frames and Transformations

A.1 Coordinate Frame Descriptions

ITRF

The International Terrestrial Reference Frame (ITRF) is a geocentric coordinate system fixed to the rotating Earth [1], with the z -axis through the north pole, the x -axis through the prime meridian, and the y -axis completing the right-handed triad.

ICRF/GCRF

The International Celestial Reference Frame (ICRF) is defined by the adopted locations of hundreds of extragalactic radio sources [24]. It is the best realization of an inertial frame constructed to date [15]. The Geocentric Reference Frame (GCRF) is its geocentric counterpart.

J2000

The inertial J2000 frame is defined by the mean equator and mean equinox of the J2000 epoch (1/1/00 12:00:00.000 TDB) [15]. It is also tied to the FK5 star catalog [25].

TEME

The inertial True Equator, Mean Equinox (TEME) frame is used by SGP4. Whereas the J2000 frame is defined by the mean equator, mean equinox of the J2000 epoch, the TEME frame is defined by the true equator, mean equinox of an arbitrary epoch [1].

GCRF/J2000 Comparison

The GCRF is essentially the same as the J2000 frame except that it is tied to extragalactic radio sources instead of a star catalog. These radio sources are very distant in comparison to the stars, and are not subject to stellar proper motion [25]. While [15] notes that the J2000 frame rotates very slowly over time with respect to the GCRF, their difference is less than 0.1 arcsecond [24]. In fact, these two frames are considered the same in the SPICE data system [24].

A.2 Coordinate Transformations

Figure A.1 shows a roadmap of the possible transformations between Earth-fixed and inertial coordinate frames. The left and middle columns are more recently developed theories, and transform a vector from the ITRF to the GCRF. The right column transforms a vector from the ITRF to the J2000 frame.

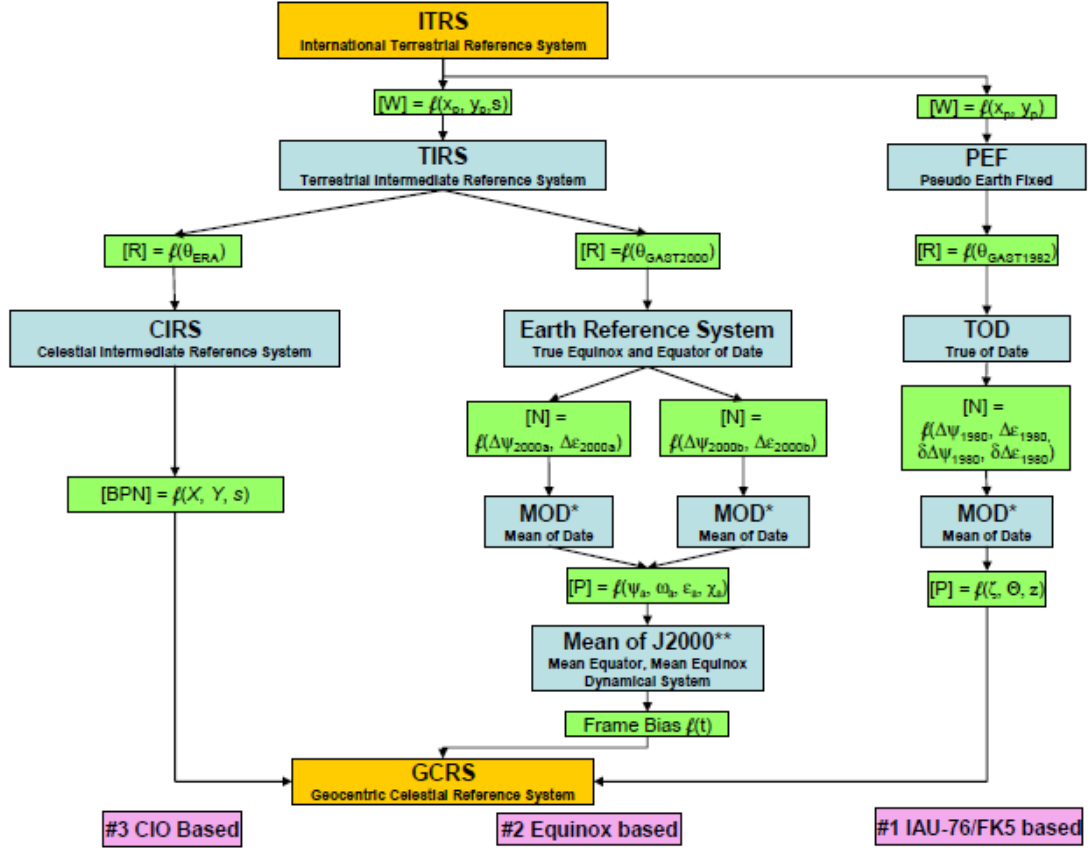


Fig. A.1: Three general approaches for transformations between terrestrial (Earth-fixed) and celestial (inertial) systems [1].

GCRF to ITRF

The GCRF is related to the ITRF though a series of rotation matrices,

$$\mathbf{r}^{GCRF} = \mathbf{PN}(t)\mathbf{R}(t)\mathbf{W}(t)\mathbf{r}^{ITRF}, \quad (\text{A.1})$$

where the superscript denotes the coordinate frame, \mathbf{PN} is the precession-nutation matrix of date t , \mathbf{R} is the sidereal-rotation matrix of date t , and \mathbf{W} is the polar-motion matrix of date t . There are different approaches for calculating these rotation matrices. For this analysis, CIO based approach (left column of Figure A.1) was used [1, 26, 27].

TEME to J2000

The J2000 frame is related to the TEME frame through a series of rotation matrices,

$$\mathbf{r}^{J2000} = \mathbf{P}(t)\mathbf{N}(t)\mathbf{R}_3(-Eq_{Equinox1982})\mathbf{r}^{TEME}, \quad (\text{A.2})$$

where the superscript denotes the coordinate frame, \mathbf{P} is the precession matrix of date t , \mathbf{N} is the nutation matrix of date t , and \mathbf{R}_3 is a rotation about the z-axis by the angle $Eq_{Equinox1982}$. The precession and nutation matrices are calculated using the 1976 IAU Theory of Precession and 1980 Theory of Nutation. The angle $Eq_{Equinox1982}$ is calculated using the equation of the equinoxes [1, 26, 27].

Appendix B

RK4 and NLZD4/4 Test Cases

The following sections present a series of differential equations to compare the RK4 and NLZD4/4 integrators. The equations tested are all linear, so an analytic solution is available. The equations are numerically integrated and compared to the analytic "truth" solution to analyze their accuracy.

B.1 First-Order Differential Equations

Consider the following equation,

$$\dot{x} = -\frac{x}{25}, \tag{B.1}$$

which is a function of position only. Equation (B.1) has the solution

$$x(t) = x_0 e^{-t/25}. \tag{B.2}$$

Figure B.1 shows the position error as a function of number of integration steps when integrating from $t = 0$ to $t = 25$ with the initial condition $x_0 = 1$.

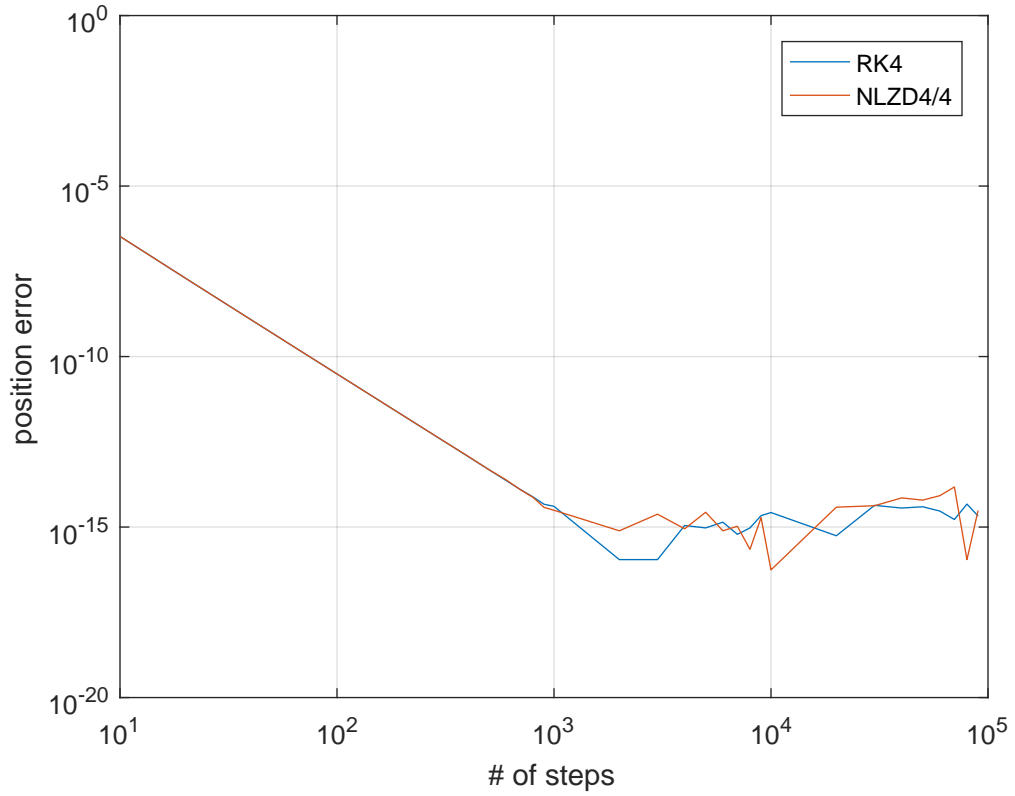


Fig. B.1: Position error for $\dot{x} = f(x)$.

Consider the following equation,

$$\dot{x} = -\frac{x}{25} + \frac{t}{10}, \quad (\text{B.3})$$

which is a function of position and time. Equation (B.3) has the solution

$$x = \left(x_0 + \frac{125}{2}\right) e^{-t/25} + \frac{5}{2}t - \frac{125}{2}. \quad (\text{B.4})$$

Figure B.2 shows the position error as a function of number of integration steps when integrating from $t = 0$ to $t = 25$ with the initial condition $x_0 = 0$.

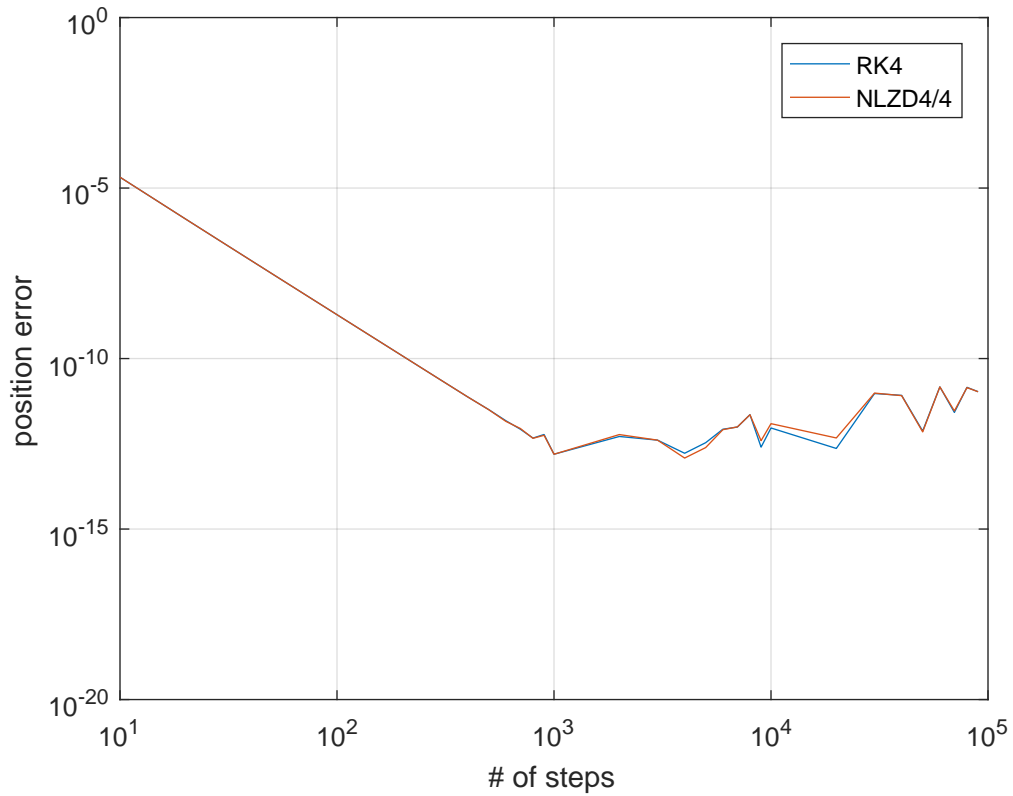


Fig. B.2: Position error for $\dot{x} = f(x, t)$.

Consider the following equation,

$$\dot{x} = -\frac{x}{25} + \cos(t), \quad (\text{B.5})$$

which is a function of position and time. Equation (B.5) has the solution

$$x(t) = \left(x_0 - \frac{25}{626}\right) e^{-t/25} + \frac{625}{626} \sin(t) + \frac{25}{626} \cos(t). \quad (\text{B.6})$$

Figure B.3 shows the position error as a function of number of integration steps when integrating from $t = 0$ to $t = 25$ with the initial condition $x_0 = 0$.

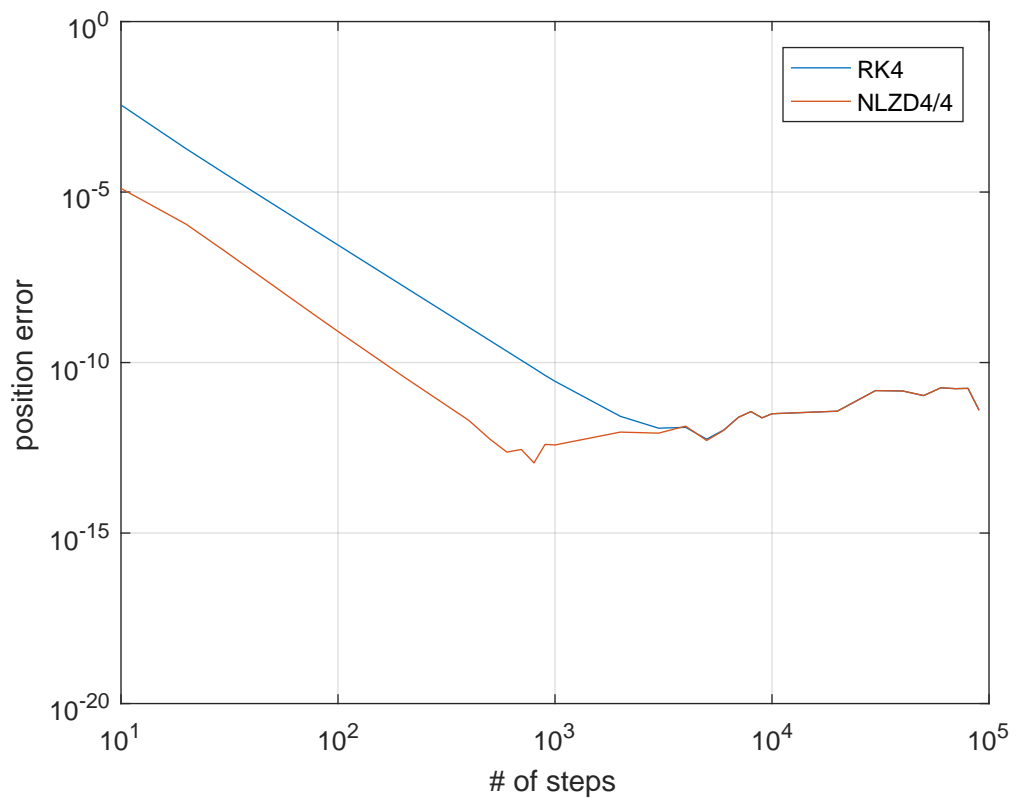


Fig. B.3: Position error for $\dot{x} = f(x, t)$.

B.2 Second-Order Differential Equations

Consider the following equation,

$$\ddot{x} = \frac{\dot{x}}{4} - x + \cos(4t), \quad (\text{B.7})$$

which is a function of velocity, position, and time. Equation (B.7) has the solution

$$x(t) = \left\{ \frac{8}{3\sqrt{7}} \left(\dot{x}_0 + \frac{2}{113} - \frac{1}{8} \left(x_0 + \frac{15}{226} \right) \right) \sin \left(\frac{3\sqrt{7}}{8} t \right) + \left(x_0 + \frac{15}{226} \right) \sin \left(\frac{3\sqrt{7}}{8} t \right) \right\} e^{t/8} - \frac{1}{226} \sin(4t) - \frac{15}{226} \cos(4t) \quad (\text{B.8})$$

Figure B.1 shows the position error as a function of number of integration steps when integrating from $t = 0$ to $t = 25$ with the initial conditions $\dot{x}_0 = x_0 = 0$.

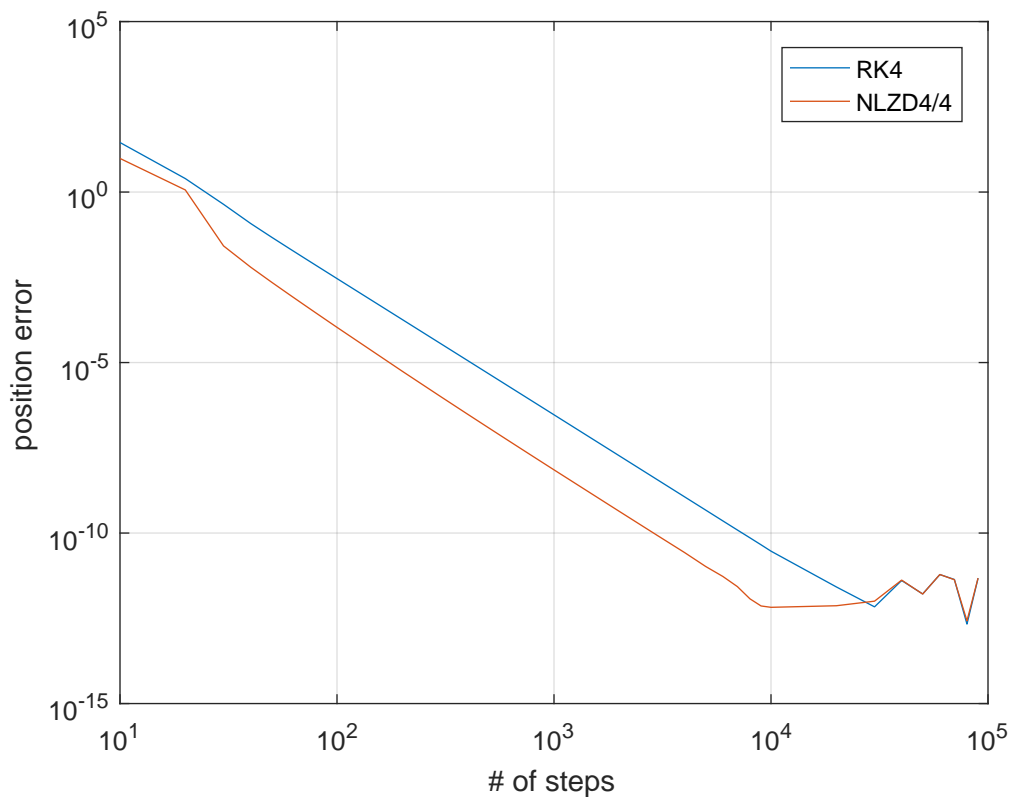


Fig. B.4: Position error for $\ddot{x} = f(\dot{x}, x, t)$.

Consider the following equation,

$$\ddot{x} = -x + \cos(4t), \quad (\text{B.9})$$

which is a function of position and time. Equation (B.9) has the solution

$$x(t) = \dot{x}_0 \sin(t) + \left(x_0 + \frac{1}{15}\right) \cos(t) - \frac{1}{15} \cos(4t) \quad (\text{B.10})$$

Figure B.5 shows the position error as a function of number of integration steps when integrating from $t = 0$ to $t = 25$ with the initial conditions $\dot{x}_0 = x_0 = 0$.

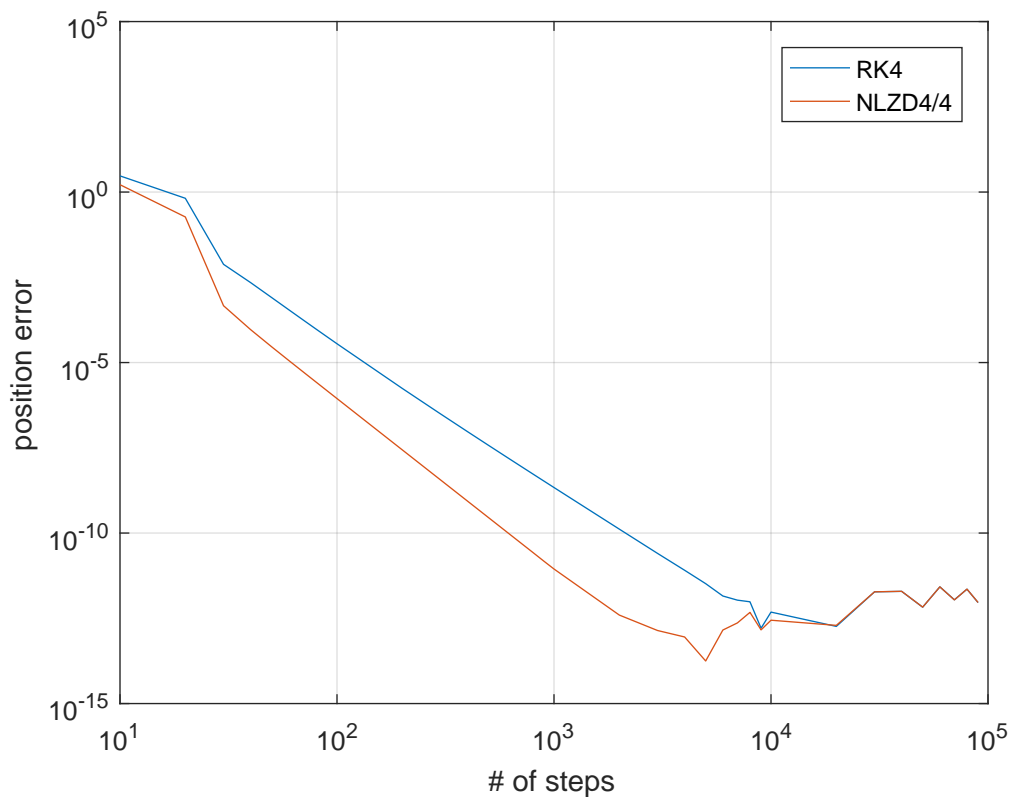


Fig. B.5: Position error for $\ddot{x} = f(x, t)$.

Consider the equation,

$$x(t) = \cos(4t), \quad (\text{B.11})$$

which is a function of time only. Equation (B.11) has the solution

$$x(t) = x_0 + \frac{1}{16} + \dot{x}_0 t - \frac{1}{16} \cos(4t). \quad (\text{B.12})$$

Figure B.6 shows the position error as a function of number of integration steps when integrating from $t = 0$ to $t = 25$ with the initial conditions $\dot{x}_0 = x_0 = 0$.

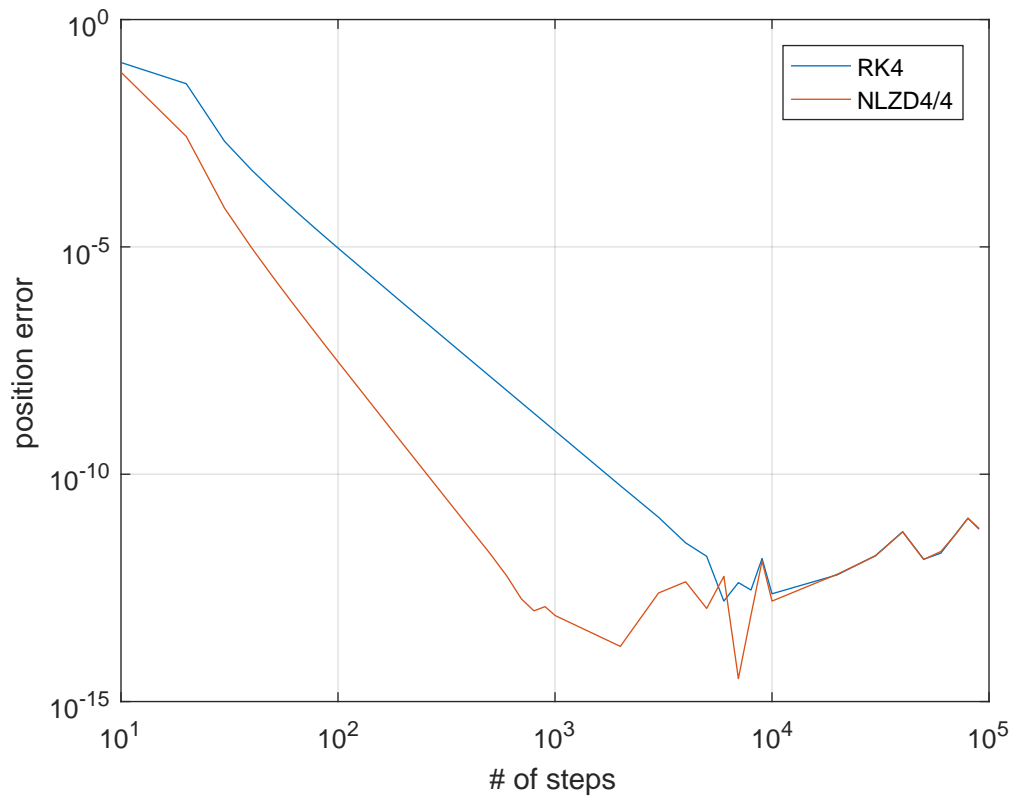


Fig. B.6: Position error for $\ddot{x} = f(t)$.

Appendix C

Elliptical Orbit Propagation Errors

Figures C.1 through C.4 show how numerically propagating an elliptical orbit results in distinct swoops in the position error as a function of time (see Figures 7.1 and 8.1). In short, this behavior is caused by a combination of integration step distribution, integration error direction, and elliptical orbital motion.

Figure C.1 shows, for a 2-body Molniya orbit, position error between numerical and analytical propagation, and true anomaly as a function of time. The step size for numerical propagation was intentionally selected to induce integration error. Figure C.1 highlights the relationship between position error and true anomaly. As discussed in Section 2.2.2 and shown in Figure 2.1, equal time steps around an elliptical orbit are sparsely distributed around perigee, a region where they're most needed to mitigate integration error. Despite different initial true anomalies (indicated by different colors), local peaks in position error and perigee passage occur simultaneously.

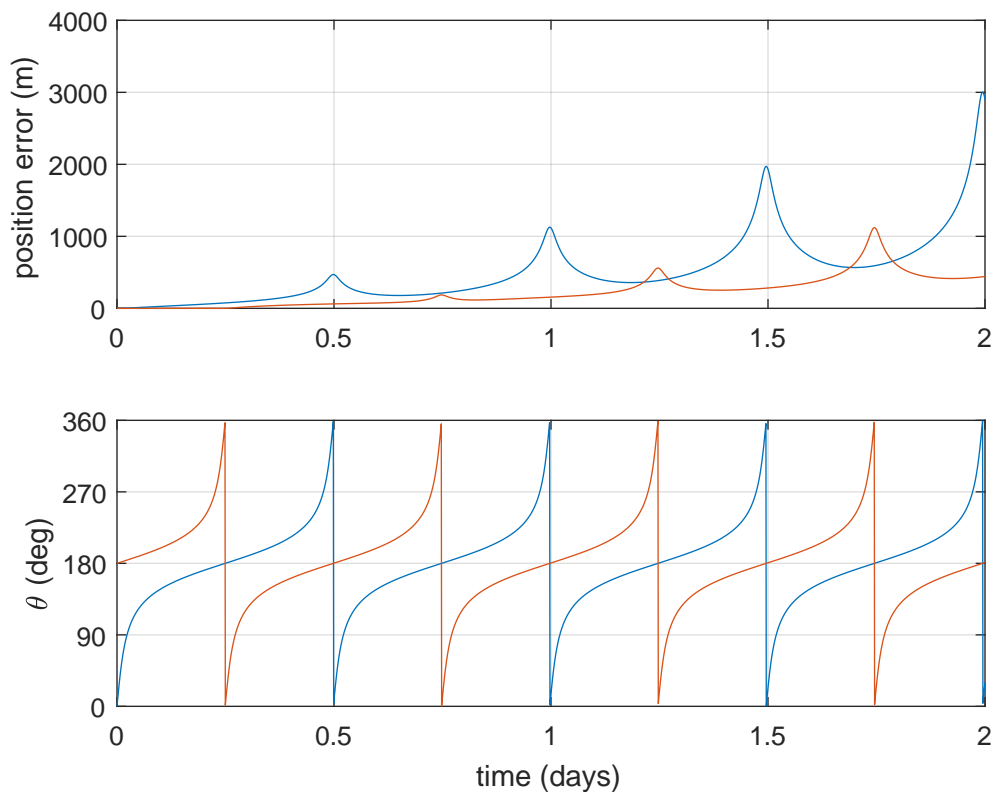


Fig. C.1: Position error and true anomaly as a function of time for numerically propagated 2-body Molniya orbits. Initial true anomalies are indicated by color: $\theta_0 = 0^\circ$ (blue) and $\theta_0 = 180^\circ$ (red).

Figure C.1 shows how position error arises using Cowell's formulation. Encke and Equinoctial Elements are only valid when a perturbing acceleration is present, which might suggest that neglecting the full orbital motion would eliminate these position error trends.

Figure C.2, however, shows how local position error peaks around perigee remain despite using different formulations. The magnitude of the perturbing acceleration is highest around perigee. This results in a similar problem experienced by Cowell. Too few integration steps are allocated around an area where the amplitude and frequency of the perturbing function is highest. Therefore integration error still grows around perigee despite neglecting the full equations of motion. These errors are much smaller than Cowell, but the general behavior is the same.

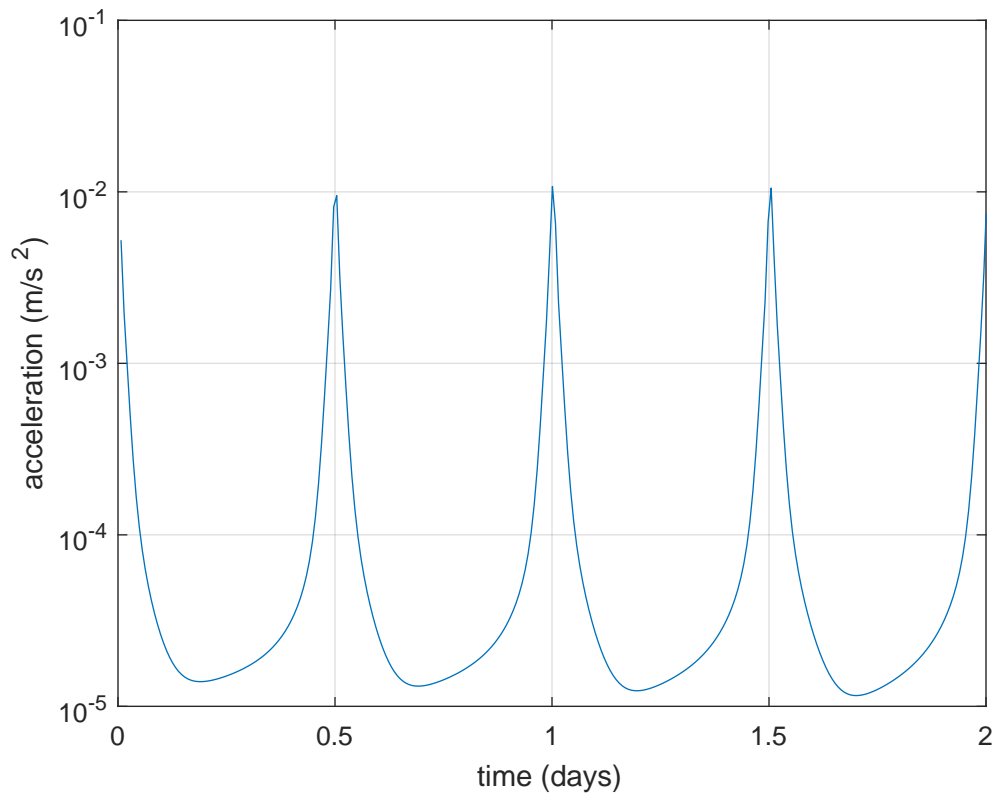


Fig. C.2: Magnitude of the perturbing acceleration for the Molniya orbit truth ephemeris (initial state given in Table 4.1 and environment model given in Table 4.3).

Time regularization improves the distribution of integration steps, but it does not completely invert the amount of steps allocated around apogee and perigee. Encke-beta significantly increases position accuracy as a result of distributing equal steps in universal anomaly, but it remains susceptible to the same effects experienced by time-based formulations. Figures 7.1 and 8.1 show that Encke-beta position error still shows local peaks around perigee.

While distribution of integration steps explains the increase in position error around perigee, it does not explain the decrease in position error around apogee. For time-based formulations, integration steps are abundantly distributed around apogee so approximation error is mitigated. However, it seems that any position error accumulated around perigee

would remain throughout the orbit, resulting in a stepwise trend rather than swoops. It turns out, position error mainly lies in the orbital plane, and elliptical orbital motion causes it to expand and contract.

Figure C.3 shows position error in terms of radial, intrack, and crosstrack components for a Molniya orbit (initial state given in Table 4.1 and environment model given in Table 4.3), propagated using Encke and Equinoctial Elements with the RK4 and 10^4 integration steps over 7 days ($\Delta t = 60.48$). The LVLH frame is defined by the truth ephemeris.

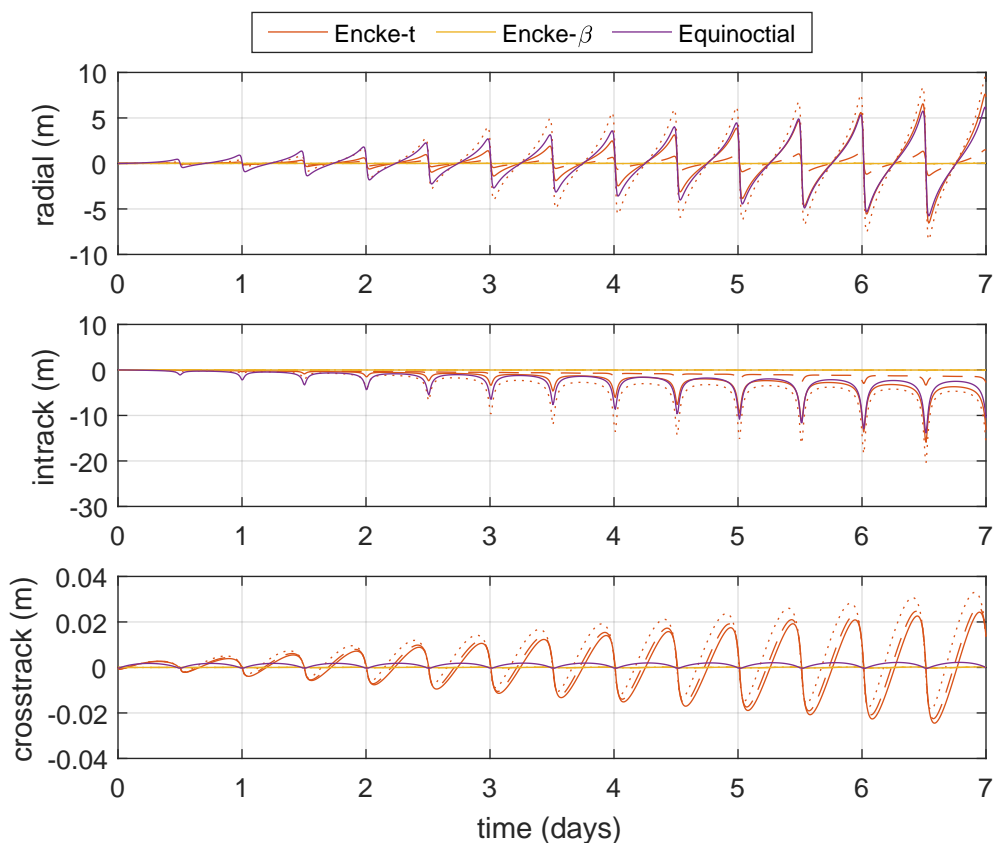


Fig. C.3: Radial, intrack, and crosstrack position error as a function of time for a Molniya orbit, propagated using Encke and Equinoctial with the RK4 and 10^4 integration steps over 7 days ($\Delta t = 60.48$). Encke formulations indicate the following rectification tolerances: solid = 0% (every step), dashed = 0.01%, dotted = 0.1%.

The key takeaway from these plots is that the majority of position error lies in the orbital plane. While Figure C.3 only shows Encke and Equinoctial formulations, Cowell

behaves the same way, but on a larger scale. Changing the number of integration steps changes the magnitude of position error, but the majority remains in-plane. Although it is not plotted, velocity errors are present as well. They exhibit a similar distribution shown in Figure C.3 in terms of in-plane and out-of-plane components.

Figure C.4 shows the position difference between two 2-body Molniya orbits with an initial in-plane state separation. In terms of orbital elements, their initial state difference is $\delta\theta = 0.05^\circ$ and $\delta a = 10$ m. The orbits begin at or near perigee.

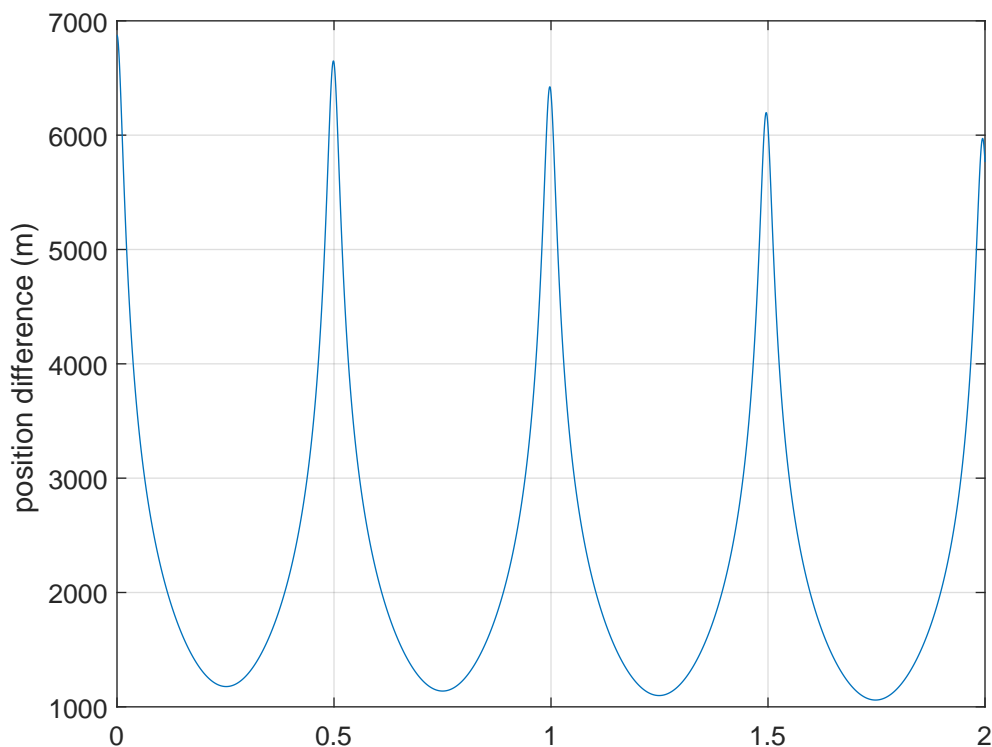


Fig. C.4: Position difference between 2-body Molniya orbits with an initial state difference (in terms of orbital elements) of $\delta\theta = 0.05^\circ$ and $\delta a = 10$ m.

This plot shows how elliptical orbital motion causes an in-plane state difference near perigee to naturally contract around apogee, and then expand again around perigee. The same distinct swoops are present.

To summarize, swoops in position error are caused by integration step distribution, integration error direction, and elliptical orbital motion. Integration step distribution yields approximation error around perigee, where too few integration steps inadequately approximate perturbed orbital motion (Cowell) or perturbed motion alone (Encke and Equinoctial Elements). The majority of this error, both in position and velocity, is directed in the orbital plane. This in-plane error naturally contracts around apogee, where a sufficient amount of integration steps keeps the approximation error negligible. Upon returning to perigee, the in-plane error naturally expands and additional approximation error accumulates. This process continues, resulting in position error swoops with secular growth.